DEPARTMENT OF PHYSICS
UNIVERSITY OF JYVÄSKYLÄ
RESEARCH REPORT No. 7/2014

INTRINSIC TRANSVERSE MOMENTUM DISTRIBUTION OF JET CONSTITUENTS IN P-PB COLLISIONS AT ALICE

BY
JIŘÍ KRÁL

Academic Dissertation
for the Degree of
Doctor of Philosophy

To be presented, by permission of the Faculty of Mathematics and Science
of the University of Jyväskylä, for public examination in Auditorium FYS 1
of the University of Jyväskylä on August 8th, 2014, at 12 o'clock noon

Jyväskylä, Finland
August 2014

This thesis is dedicated to my parents,
who know the great value of education and supported me from my earliest days,
providing me with the foundation to pursue it further.

Abstract

Král, Jiří
Intrinsic transverse momentum distribution of jet constituents in p–Pb collisions at ALICE
Jyväskylä, University of Jyväskylä, 2014, 153 p.
Department of Physics Research Report No. 7/2014
ISBN: 978-951-39-5740-7
ISBN PDF: 978-951-39-5741-4
ISSN: 0075-465X

Keywords: jet fragmentation, transverse momentum, nuclear collisions, havy ions, electromagnetic calorimeter, trigger, ALICE

Author	Jiří Král University of Jyväskylä Finland
Supervisor	Prof. Jan Rak University of Jyväskylä Finland
Reviewers	Dr. Alexander Kupčo Institute of Physics ASCR, v.v.i. Czech Republic
	Dr. Sebastian White Rockefeller Univesity USA
Opponent	Dr. Michael J. Tannenbaum Brookhaven National Laboratory USA

Acknowledgements

I would like to express my great gratitude to my supervisor Prof. Jan Rak, who supervised me in my research. I would like to thank him for providing me this golden opportunity to work in the field. The presented results would not have been achieved without his involvement.

Special thanks belong to Dr. Sami Räsänen, Dr. Filip Křížek and Dr. Astrid Morreale for their help and useful guidance that they provided over the time. I would also like to thank the remaining past and present members of ALICE Jyväskylä Group for providing the working environment.

A very special thanks to Dr. Terry Awes, Dr. Hans Muller and Dr. David Sivermyr for their continuous support in the ALICE EMCal project. Thanks goes to all people participating on ALICE coordination and runs for being such a great group of people to work with. I would also like to acknowledge the support from the Jet Physics Working Group, especially Dr. Jana Bielčíková, Dr. Marta Verweij, Dr. Christine Nattrass, Dr. Rosi Jan Reed and Dr. Marco Van Leeuwen.

I would like also express my thanks to Dr. Redamy Perez-Ramos who provided the theoretical calculations to the data presented in the thesis.

The last, but not least thanks belong to my friends Myroslav Myška and Michal Nyklíček for their friendly support.

Contents

Chapter 1

Introduction

The currently largest and most recent accelerator, The Large Hadron Collider (LHC) [1], was constructed at the European Organization for Nuclear Research (CERN) during the past decades. The physics aims of the LHC project are: to discover crucial missing elements of the Standard Model, namely the Higgs boson; to search for possible new fundamental interactions, too week to have been observed so far; to search for new possible generations of quarks or leptons; to discover evidence for particles responsible for the Dark Matter in the Universe and to explore the Quantum ChromoDynamics (QCD) phases of matter in the Ultra-Relativistic Heavy Ion Collision (URHIC).

The accelerator was commissioned in 2009 and reached new energy frontiers with the highest center of mass energy $\sqrt{s} = 8$ TeV in the pp and $\sqrt{s_{\mathrm{NN}}} = 2.76$ TeV in Pb–Pb collision. It is still expected to reach the top designed energy of $\sqrt{s} = 14$ TeV in the near future. The LHC run I (2010-2013) delivered many exciting results. Among those the most celebrated one is the discovery of the Higgs like boson by ATLAS [2] and CMS [3] experiments.

Beside the research in the electroweak sector, LHC experiments are also designed to study the strongly interacting matter and its phase transition. The QCD is known to be the only gauge theory where phase transition is reachable experimentally. High temperatures and densities reached in the ultra-relativistic nuclear collisions give rise to the medium of deconfined quarks and gluons, called Quark Gluon Plasma[1] (QGP) [4] and this is the main objective of study of the ALICE [5], one of the four major LHC experiments.

The integral part of the URHIC program is also to study the pp and p–A collision in order to understand the "reference" (unmodified) particle production (in pp) and the "cold" nuclear phenomena in p–A. The main focus of this thesis is to study the parton shower evolution in p–Pb collisions in ALICE by analyzing jet fragmentation

---

[1] Nowadays we know that the properties of the deconfined nuclear medium can be characterized as ideal liquid rather than plasma, the QGP acronym is used in this theses to refer to deconfined "liquid-like" nuclear medium.

transverse momentum (j_T). The analysis of j_T in p–Pb collisions, for which ALICE has a high quality data set, lays bases for later extension to pp and Pb–Pb data in order to study the induced gluon radiation. Additionally, the yields of π^0 meson were studied in Pb–Pb $\sqrt{s_{\mathrm{NN}}} = 2.76$ GeV collision. The π^0 analysis was followed for continuity of work with EMCal detector and as a complement to already progressing π^0 yield analysis in pp.

The thesis also focuses on ALICE Electromagnetic Calorimeter (EMCal) and the single-photon Level-0 trigger. Development of the Level-0 trigger system was an important part of this work. From the data analysis point of view it is evident that without the L0 trigger it would be difficult to obtain many of the results presented in this thesis. EMCal is the sole large acceptance calorimeter in ALICE, which usage is crucial for full reconstruction of jets. Triggering in EMCal is important for enhancing sample of fully reconstructable jets.

This thesis is organized as follows: Chapter 1 provides introduction into the physics of the conducted analysis. A basic overview of QCD and URHIC physics is provided. Additionally, some elementary facts related to the jet production and the soft QCD radiation are discussed.

The following chapter 2 introduces the LHC machine and the ALICE experiment. The EMCal detector played an important role in this analysis and thus the EMCal performance is discussed in more details in chapter 3. Especially the topics that have potential impact on functionality of the calorimeter trigger are studied. Chapter 4 presents development and performance of EMCal Level-0 trigger system. Interesting solutions that were developed in order to circumvent some hardware limitation are highlighted.

Chapter 5 describes the π^0 yield analysis. The π^0 yield is reconstructed based on invariant mass of photon pairs captured in EMCal. The reconstruction efficiency, mass spectrum originating from photon conversions and the residual background subtraction are discussed. The π^0 invariant yield extracted from Pb–Pb $\sqrt{s_{\mathrm{NN}}} = 2.76$ TeV minimum bias and triggered data samples is analyzed. Some physics implications related to the apparent disagreement between NLO expectation and the π^0 yield measured in pp $\sqrt{s}$ = 0.9 and 7 TeV are also discussed.

Chapter 6 contains a description of the jet fragmentation transverse momentum (j_{T}) studies in p–Pb $\sqrt{s_{\mathrm{NN}}} = 5.02$ TeV data. Jets have been reconstructed using the anti-k_{T} algorithm and the distribution of the transverse component of the jet constituents with respect to jet axis is studied in bins of jet virtuality. Discussion of the j_T analysis results and the comparison to NMLLA theory and PYTHIA models is presented.

Finally the thesis is concluded in chapter 7.

1.1 Quantum ChromoDynamics

The Quantum ChromoDynamics (QCD) is a non-Abelian gauge quantum field theory that describes the strong force interaction [6–8]. Together with Quantum ElectroDynamics (QED) and weak interaction they comprise Standard Model (SM) of electroweak and strong interactions.

Large numbers of discovered hadrons in 1950s led Gell-Mann [9] and Zweig [10] to a proposition that hadrons were composed of spin-1/2 fermions quarks (or aces) and anti-quarks of three flavors (u, d, s). Existence of the spin-3/2 Δ^{++} baryon composed of three u quarks, violating the Pauli exclusion principle, led to introduction of an additional degree of freedom called "color" [11]. Success of the quark model was marked by discovery of predicted Ω^- baryon [12].

Data from electron-proton deep inelastic scattering experiments at SLAC [13] resulted in extension of the quark model to parton model presented by Faynman [14] and Bjorken [15]. In the parton model, the nucleon is composed of multiple quarks with their net sum being identical to values in quark model (valence quarks). The additional quarks present in the nucleon are called sea quarks.

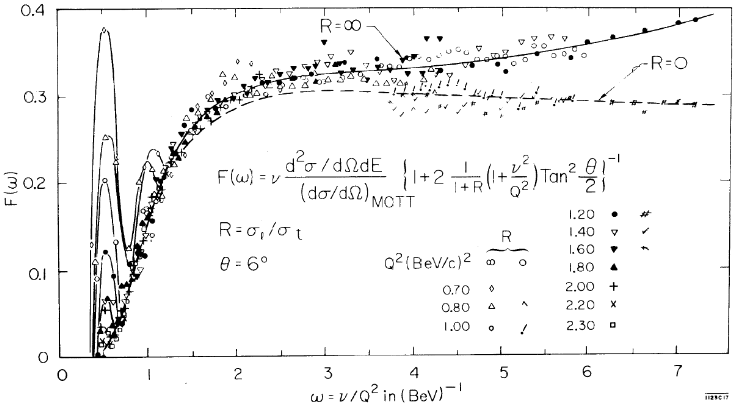

Figure 1.1: Figure of function $F(\omega) = \nu W_2(Q^2, \nu)$ plotted against variable $\omega = \nu/Q^2$ [16]. The figure shows first observation of independence of W_2 on Q^2 (dependence of $F(\omega)$ on ν/Q^2 ratio), later called the Bjorken scaling.

The cross section of the deep inelastic scattering process can be written as a sum of structure functions $W_1(Q^2, \nu)$ and $W_2(Q^2, \nu)$,

$$\frac{\mathrm{d}^2\sigma}{\mathrm{d}\Omega \mathrm{d}E'} = \frac{\alpha^2}{4E^2 \sin^4\left(\frac{\theta}{2}\right)} \left[W_2(Q^2, \nu)\cos^2\left(\frac{\theta}{2}\right) + 2W_1(Q^2, \nu)\sin^2\left(\frac{\theta}{2}\right)\right] \tag{1.1}$$

where α is fine-structure constant ($\alpha \approx 1/137$), Q^2 is the momentum transfer squared and ν is the recoil energy. Observation of the Bjorken scaling [17] (Fig. 1.1), independence of the W_2 on Q^2, which led to proposition of the parton model, and later observation of the predicted 3-jet events [18] resulted in acceptance of the parton model. Nowadays we know six flavors of quarks ("up", "down", "strange", "charm", "bottom", "top") with the latest top being discovered relatively recently in 1995 [19,20]. It is also known from the measurements at the Large Electron-Positron Collider [21] that number of light neutrinos is 3, with 3 neutrinos (and e, μ and τ) the fermion family in Standard Model is complete.

The QCD color quantum number ("red", "green", "blue") has symmetry described by the SU(3) group. Experimental results e.g. the measurement of the π^0 decay width confirm the number of colors to be 3 [22]. There are 8 generators of the SU(3) group, which give 8 gluons. The generators do not commute, the SU(8) group is non-Abelian, so the gluons carry color charge and can interact amongst themselves.

1.1.1 Asymptotic freedom

The non-Abelian nature of QCD results in existence of purely gluon-gluon fluctuations. The spin magnetic alignment of the gluon-gluon fluctuations causes anti-screening of the color charge, opposite to screening, effect caused by the dipole alignment of $q\bar{q}$ virtual pairs (alike $e^{\pm}$ virtual pairs in QED) [23].

With the given number of colors, $N_c = 3$, and flavors, $N_f = 6$, the anti-screening effect caused by gluon loops dominates over the screening effect due to the dipole alignment of $q\bar{q}$ fluctuations. In other words the 1-loop approximation of beta function $\beta_0 = (11N_{\mathrm{c}} - 2N_{\mathrm{f}})$ in Eq. (1.2) is positive and the denominator grows with Q^2. It is the reason why the strong coupling constant vanishes at small distance/large momentum transfer $\alpha_s \to 0|_{Q^2 \to \infty}$ (Fig. 1.2). In the leading order of the perturbative expansion the strong coupling is given by Eq. (1.2)

$$\alpha_{\mathrm{s}}(Q^2) = \frac{\alpha_{\mathrm{s}}(\mu_0^2)}{1 + \beta_0 \alpha_{\mathrm{s}}(\mu_0^2) \ln\left(\frac{Q^2}{\mu_0^2}\right)} \tag{1.2}$$

where Q^2 is the momentum transfer and μ_0 is the renormalization scale. The one loop approximation of the beta function, β_0, comes from the renormalization group equation

$$\mu^2 \frac{\partial \alpha(\mu^2)}{\partial \mu^2} = \beta(\alpha_{\mathrm{s}}(\mu^2)) \approx -\beta_0 \alpha_{\mathrm{s}}^2(\mu^2) - \beta_1 \alpha_{\mathrm{s}}^3(\mu^2) + O(\alpha_{\mathrm{s}}^4) \tag{1.3}$$

The 1-loop approximation, β_0, becomes negative for $N_{\mathrm{f}} \geq 17$ and such a strongly coupled theory would be screened as it is in the case of QED.

The $\alpha_{\mathrm{s}}(Q^2)$ describes the change of the strong coupling with Q^2. Absolute value of the coupling is measured usually at $Q = M_Z$, which is large enough to be in the perturbative region. It is also useful express the $\alpha_{\mathrm{s}}(Q^2)$ using a dimensionful parameter Λ, in the leading order

$$\alpha_s(Q^2) = \frac{1}{\beta_0 \ln\left(\frac{Q^2}{\Lambda^2}\right)}$$

For number of active flavors = 5, the $\Lambda \equiv \Lambda_{\mathrm{QCD}} \approx 220$ MeV, gives a value, where the coupling starts to diverge.

The asymptotic behavior of α_s was realized by Gross, Wilczek [24] and Politzer [25] and confirmed experimentally [26]. The strong coupling goes to zero for interaction with large momentum transfer, the quarks are seen asymptotically as free objects and hence the name "Asymptotic Freedom".

In the standard conditions, the quarks are observed bound (confined) to color singlet states, colorless baryons and mesons. A free colored object has not been observed.

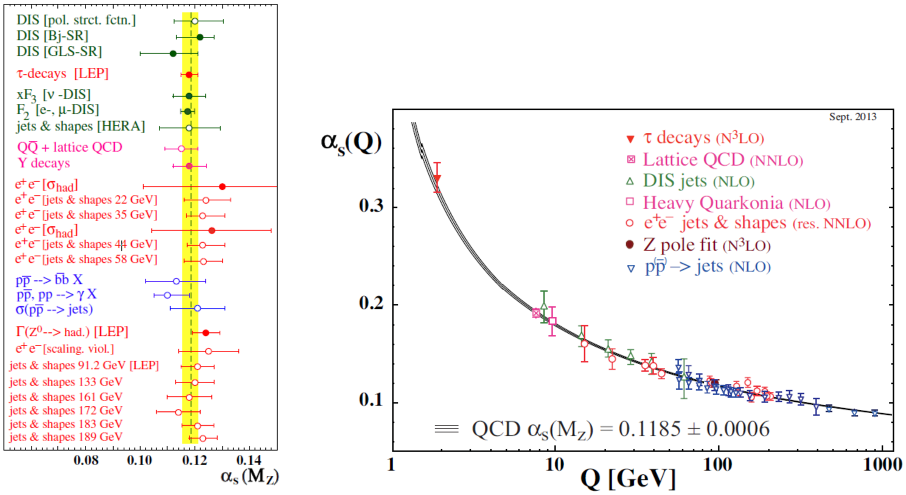

(a) (b)

Figure 1.2: (a) Summary of $\alpha_s(M_{Z^0})$ (filled symbols represent results based on complete NNLO QCD) [27]. (b) Summary of measurements of α_s as a function of the energy scale Q. The respective degree of QCD perturbation theory used in the extraction of α_s is indicated in brackets (NLO: next-to-leading order; NNLO: next-to-next-to leading order; res. NNLO: NNLO matched with resummed next-to-leading logs; N^{3}LO: next-to-NNLO) [28].

1.1.2 Quark Gluon Plasma

Based on the asymptotic freedom, Collins and Perry predicted that a matter composed of deconfined quarks may exist in extreme conditions in super dense matter of neutron stars cores, exploding black holes or at the early big bang [29]. One step further, Shuryak explored idea of a state of matter *"When the energy density ε exceeds some typical hadronic value ($\sim$1 GeV/fm^3), matter no longer consists of separate hadrons (protons, neutrons, etc.), but of their fundamental constituents, quarks and gluons. Because of the apparent analogy with similar phenomena in atomic physics we may call this phase of matter the QCD (or quark-gluon) plasma."* [4].

The prediction of QGP existence marked the beginning of URHI era, quest for the experimental evidence of QGP. In fact, the QGP is not a plasma, but rather an ideal liquid, as will be discussed in the next section.

1.2 Heavy Ion Physics

Collisions of heavy nucleons provide access to hot and dense environment, required to create the deconfined state of strongly interacting matter, the QGP. Exploration of the new state of matter started in 1980s and gave birth to the physics of Ultra Relativistic Heavy Ion Collisions (URHIC).

With two distinct states of QCD matter a transition is expected to occur at given values of system temperature (T) and baryon chemical potential (μ_B). Schematic view of the phase diagram of matter is shown on Fig. 1.3.

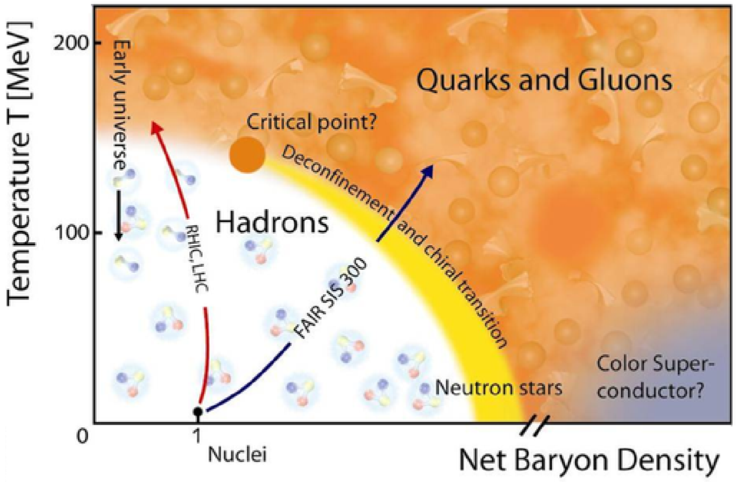

Figure 1.3: Schematic view of the QCD phase diagram. Ground state or unexcited nuclei are located at $\mu_\mathrm{B} \approx 1$ GeV and zero temperature. Arrows indicate the trajectories of URHI collisions at different c.m. energies crossing the "cross over" or first order phase transition. Since the existence of the cross over transition is experimentally confirmed, existence of the first order transition would imply then the existence of the critical point.

Perturbative techniques are not applicable for computation of the deconfined matter properties due to relatively large values of α_s in the deconfined phase [30]. The lattice QCD (lQCD) calculation [31] are capable of providing predictions for the given conditions. lQCD predicts the phase transition to happen at the critical temperature $T_c \approx 170$ MeV [32]. The critical point is predicted to be at non-zero μ_B [33] and 1st order phase transition takes place at the higher μ_B. The search of the critical point is an subject of intensive experimental effort at RHIC.

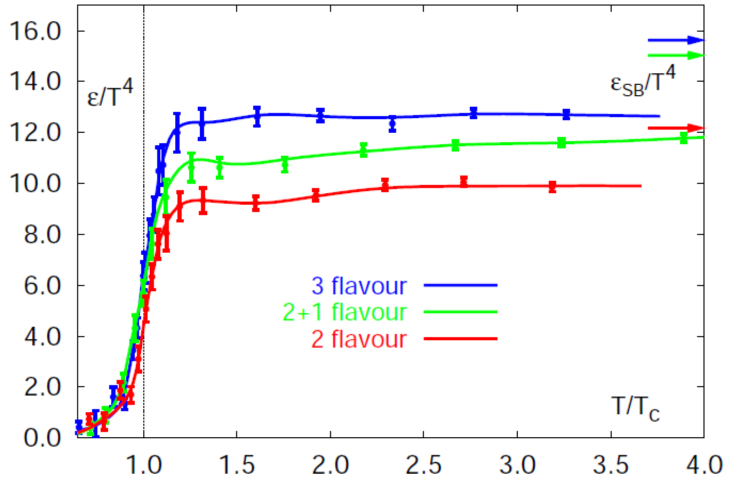

Figure 1.4: The energy density over T^4 as a function of the relative temperature T/T_c for $\mu_B = 0$ GeV [34, 35]. The calculation is done for 2 or 3 light quarks or 2 light and 1 heavy strange quark. Arrows represent the ε_{SB} limit.

Fig. 1.4 shows lattice results for the energy density as a function of system temperature. The horizontal arrows indicate the Stephan-Boltzmann (ε_{SB}) limits for 2+1 (green) and 3 (blue) flavor lQCD. Stephan-Boltzmann limit Eq. (1.4) is energy density limit for non-interacting relativistic ideal gas of particles.

$$\varepsilon_{SB}/T^4 = (n_{\text{dof,fermions}} 7/8 + n_{\text{dof,bosons}}) \frac{\pi^2}{30} \tag{1.4}$$

where n_{dof} is number of degrees of freedom for fermions (quarks) or bosons (gluons).

The lattice results suggested that the QGP is not an ideal gas of quarks and gluons, as thought initially. Later results that show presence of a strong flow and viscosity [36] in the medium point towards QGP being an ideal fluid.

1.2.1 Heavy ion collisions

Collisions of heavy ions are used to create thermalized medium of energy density above 1 GeV/fm^3, when the QGP is created. The nuclear collision evolves in space and time and goes through several stages as schematically shown on Fig. 1.5.

In the first stage of collision, parton scatterings and re-scatterings occur and thermally equilibrated plasma is created at proper time τ_0. The QGP then expands and cools down. Viscous or ideal hydrodynamics can be applied to describe the expanding system during this time. At some point, the temperature of the system decreases below the critical temperature (T_c), quarks become confined inside hadrons again. The created hadrons have enough energy to scatter inelastically, until chemical feeze-out time, when the species and multiplicities of hadrons become fixed. The collision evolution continues by elastic scattering, until kinetic freeze-out, when the momenta of products become stable.

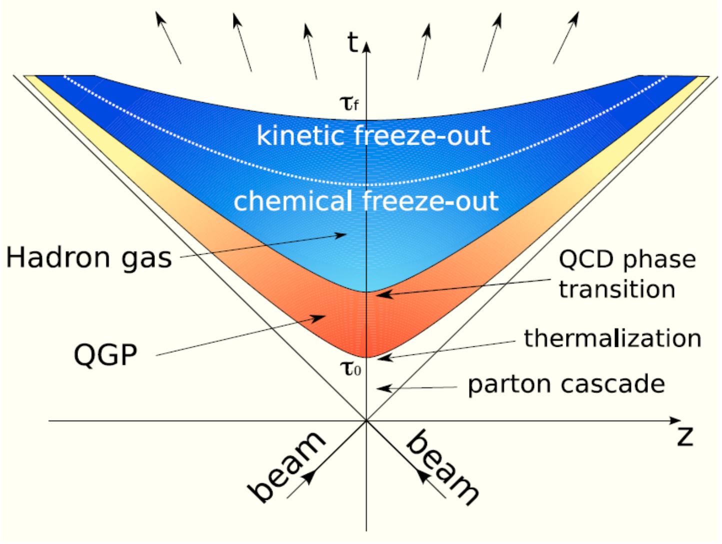

Figure 1.5: The schematic view of the space–time evolution of ultra relativistic heavy ion collision [37].

Due to the size of the nuclei, the collision of two nuclei is not necessarily head on. The overlap region (dependent on the impact parameter) of the two nuclei, which contains nucleons that actually collide, can range from full overlap (central collision) to minimal overlap (peripheral collision). With the help of Glauber model, the collisions are then sorted in centrality percentiles [38].

1.2.2 Search for QGP

The search for QGP signatures began at Berkeley Bevalac (not shown on Fig. 1.6), continued at Alternating Gradient Synchrotron (AGS) accelerator at Brookhaven National Laboratory (BNL) and at Super Proton Synchrotron at CERN with $\sqrt{s_{\mathrm{NN}}} =$ 4.5 GeV and 17 GeV respectively (lower branch on Fig. 1.6). The results at SPS provided hints of QGP existence, although some alternative explanations for the SPS observations, discussed below, were offered leaving some of heavy ion physicists unconvinced. Nevertheless, CERN announced discovery of the new state of matter in the spring 2000 [39].

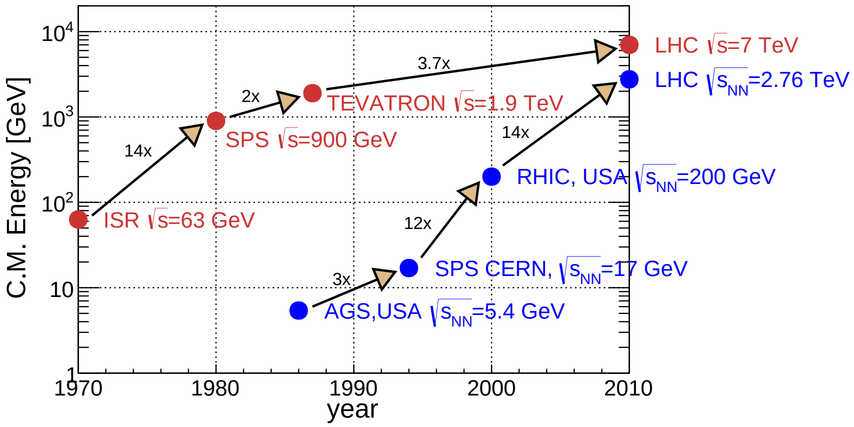

Figure 1.6: Sketch of center of mass energies (per nucleon) for recent accelerators. The blue point show energies of URHI collisions, the red points stand for pp collisions.

The main experimental evidences for the observation of the new state of matter at SPS were based for example on the observation of the low-mass dilepton enhancement [40], quarkonia suppression [41, 42] or strangeness enhancement [43, 44]. For example the dilepton mass spectrum is shown on the left panel of Fig. 1.7. The measured distribution is compared to the hadronic "cocktail", the sum of all contributions from know hadronic decays. An excess between π and ρ/ω mass range is interpreted as a partial restoration of the chiral symmetry in QGP [45]. These observations certainly support the expected trends induced by QGP. On the other hand, there were observations like high-p_{T} π^0 production at $\sqrt{s_{\mathrm{NN}}} = 17$ GeV S–S and Pb–Pb data by WA80 [46] and WA98 [47] experiments (right panel of Fig. 1.7). The solid lines represent the expectation from the pQCD calculations scaled up by number of binary collisions. The deconfined opaque medium is expected to suppress the high-p_{T} particle yield (discussed in details in section 1.4.1). This is, however, not seen on the right panel of Fig. 1.7 where the measured data (solid black symbols) show no sign of suppression as compared to scaled pQCD calculation (solid lines) [48].

The first results from Relativistic Heavy Ion Collider (RHIC) at BNL surprised everybody by strikingly large suppression of hard particle production in central Au–Au $\sqrt{s_{\mathrm{NN}}} = 130$ GeV collisions [52]. More recent data [50, 51] are shown on (Fig. 1.8). The observation of jet quenching was a strong hint towards confirmation of the QGP existence. Yet it was not clear until four years later, when results from the control d–Au run at RHIC proved that the suppression is not an initial state effect, the Color

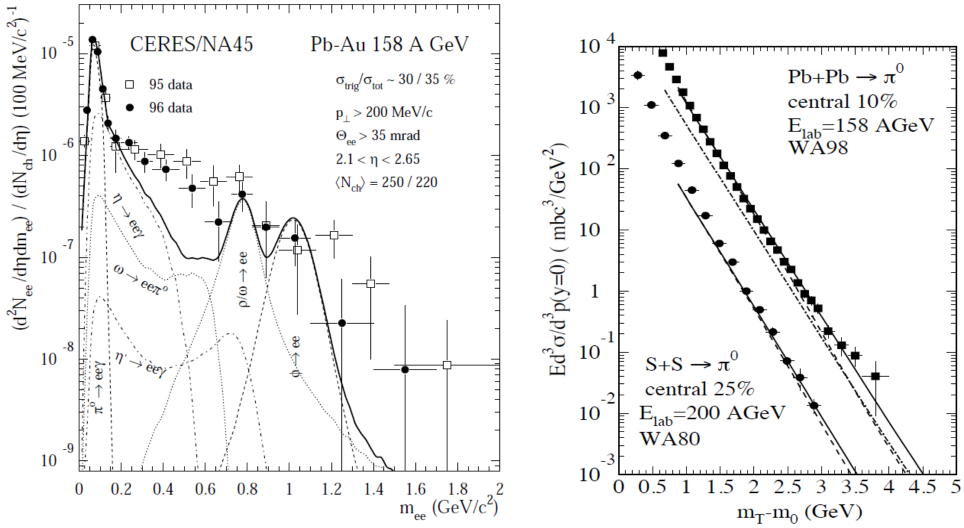

Figure 1.7: Left: e⁺e⁻ mass spectrum from CERES/NA45 experiment [49]. The data are compared to the sum of the expected contributions from hadron decays (solid line). An excess in the low mass region is interpreted to be due to the (partial) chiral symmetry restoration in QGP [45]. Right: Single-inclusive π^0 spectra in central S + S at $E_{\rm lab} = 200$ GeV (WA80) [46] and Pb + Pb collisions at $E_{\rm lab} = 158$ GeV (WA98) [47]. The solid and dashed lines represent the pQCD expectations [48]. Existence of opaque QGP should lead to a suppression of the high-$p_{\rm T}$ yield wrt pQCD scaled expectations contrary to the data.

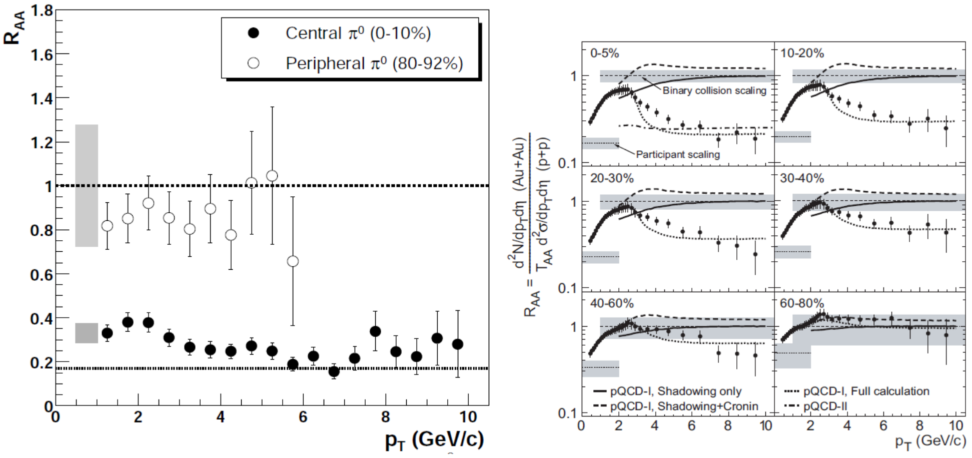

Figure 1.8: Left: Nuclear modification factor $R_{\rm AA}(p_{\rm T})$ for π^0 in central (closed circles) and peripheral (open circles) Au+Au at $\sqrt{s_{\rm NN}} = 200$ GeV [50]. Right: $R_{\rm AA}(p_{\rm T})$ for $(h^+ + h^-)/2$ in $|\eta| < 0.5$, for centrality-selected Au+Au spectra relative to the scaled p+p spectrum [51].

Glass Condensate picture see e.g. [53]. Nowadays the suppression is understood as suppression by induced gluons radiation e.g. [54–59] and many others. The p–A runs are a crucial reference to the measurements conducted in heavy ion collisions, which provide access to initial and "cold" nuclear matter effects. Another important results that support the QGP formation at RHIC are observation of flow of the medium [60,61] or studies of direct photon yields [62,63].

The importance of high p_{T} particle suppression in A–A collisions and the importance of p–A collisions as a reference measurements was also a motivation for me to study the π^0 yield in Pb–Pb (see Chapter 5) and soft QCD radiation in p–Pb collisions (Chapter 6) in ALICE at LHC.

1.3 Hard Scattering

Since the main focus of this work is on the hard probes of nucleon and nuclear collisions I will review some basic facts related to the hard scattering in the pQCD picture.

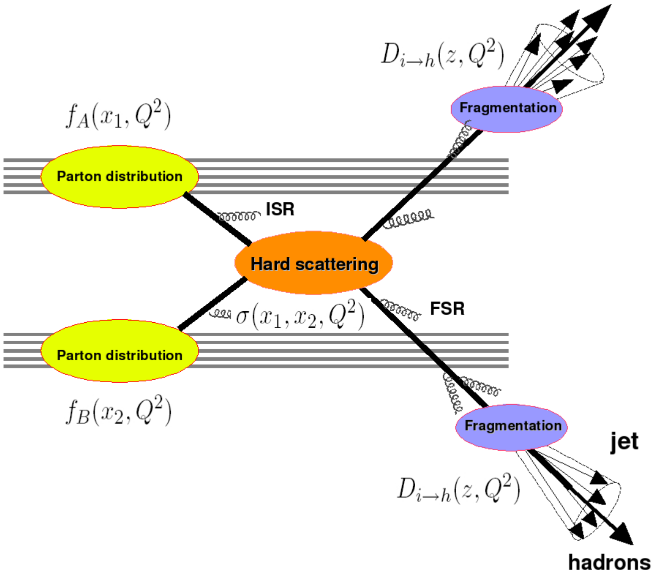

Figure 1.9: Sketch of the hard scattering event: $f_A(x,Q^2)$ are the parton distribution functions, $D_{i\to h}(z)$ the fragmentation functions, and ISR (FSR) represents initial (final)-state radiation. [54]

Hard Scattering (HS) process refers to the large momentum transfer ($Q^2 \gg \Lambda_{\mathrm{QCD}}$) scattering of the two incoming point-like constituents (quarks or gluons) mediated by an exchange of the colored quantum (sketch of HS event shown in Fig. 1.9). For a comprehensive overview see e.g. [64]. As discussed in section 1.1.1, the partons (quarks or gluons) [65] are surrounded by virtual fluctuations causing an anti-screening effect [23]. These fluctuations are partially released from the wave functions of the incoming partons in the HS process forming a spray of collimated particles (jets) in the direction of the incoming (two beam jets) and outgoing (two final state jets) parton momenta. And thus as a results of the lowest order (2→2 procces) HS four jets are produced. The radiation forming the beam jets is usually called Initial State Radiation (ISR) and the one forming the final state jets is called Final State Radiation (FSR). In the final stage of the HS all outgoing partons fragments into final state particles.

1.3.1 pQCD factorization

In the HS regime ($Q^2 \gg 1$ GeV^2), the strong coupling α_s is small and hence the perturbative expansion in powers of α_s can be applied. In the lowest order there are 8 elementary QCD suppresses involving quarks (q) and gluons (g) interactions in hadron-hadron collisions. For example the cross section of $qq' \to qq'$ scattering can be evaluated as [66]

$$\left.\frac{\mathrm{d}\sigma_{qq'\to qq'}}{\mathrm{d}\hat{t}}\right|_{\hat{s}} = \frac{\pi\alpha_s^2(Q^2)}{\hat{s}^2}\frac{4}{9}\frac{\hat{s}^2+\hat{u}^2}{\hat{t}^2} = \frac{\pi\alpha_s^2(Q^2)}{\hat{s}^2}\frac{4}{9}\left[\left(\frac{2}{1-\cos\theta^*}\right)^2 + \left(\frac{1-\cos\theta^*}{1+\cos\theta^*}\right)^2\right]$$

where $\hat{s}, \hat{t}, \hat{u}$ are the Madelstam variables, θ^* is the scattering angle and α_s is the strong coupling constant. All variables are defined at parton-parton center-of-mass frame.

The hard-scattering production cross section of hadron h in the $A + B$ nucleon-nucleon collision can be written as the sum over parton reactions $a + b \to c + d$ [67]

$$\begin{aligned}&E_h\frac{\mathrm{d}\sigma}{\mathrm{d}^3p_h}(A+B\to h+X) = \\ &\sum_{abcd}\int dx_a dx_b dz_c f_a(x_a) f_b(x_b) D_{i\to h}(z_h)\frac{\hat{s}}{z_h^2\pi}\frac{\mathrm{d}\hat{\sigma}}{\mathrm{d}\hat{t}}(ab\to cd)\delta(\hat{s}+\hat{t}+\hat{u}) \qquad (1.5)\end{aligned}$$

where $f_a(x_1)$, $f_b(x_2)$, are the differential probabilities for partons a and b to carry momentum fractions x_1 and x_2 of their respective protons. These distributions are known as a Parton Distribution Function (PDF). The $D_{i\to h}(z_h)$ function describes the distribution of the momentum fraction z_h of the parton carried out by outgoing hadron h. This function is know as a Fragmentation Function (FF). More about PDF and FF is given in section 1.3.2.

Eq. (1.5) corresponds to the incoherent sum over individual parton-parton cross sections known as the “impulse approximation” [68]. It assumes that the individual partons in a nucleon do not interact with each other during the short collision time given by the Lorentz contraction at high $\sqrt{s}$ values. Also the large Q^2 corresponds to a small distance so that it is assumed that only one parton in each nucleon is involved in the scattering. Secondarily it is assumed that the long range parts (PDFs and FFs) are universal (can be measured in different processes). The separation of the short- (cross section) and long-distance (PDF and FF) phenomena together of the assumption PDF and FF universality is known as a factorization theorem [69].

1.3.2 Parton distribution functions

The differential probability for parton a to carry the momentum fractions x of the proton momentum is described by a parton distribution function $f_a(x)$. As mentioned earlier, PDF cannot be calculated from the first principle. However, the universality assumed in the frame of the factorization theorem allows us to use PDFs measured for example in Deeply Inelastic Scattering (DIS) experiment and extrapolate these to the relevant momentum scale by use of Dokshitzer-Gribov-Lipatov-Altarelli-Parisi (DGLAP) evolution scheme [70–72] Eq. (1.6)

$$\mu_{\mathrm{F}}^2 \frac{\partial f_i(x,\mu_{\mathrm{F}}^2)}{\partial \mu_{\mathrm{F}}^2} = \sum_j \frac{\alpha_s(\mu_{\mathrm{F}}^2)}{2\pi} \int_x^1 \frac{\mathrm{d}z}{z} P_{ij}(z) f_j\left(\frac{x}{z}, \mu_{\mathrm{F}}^2\right) \tag{1.6}$$

where μ_{F} is a factorization scale. The splitting functions, P_{ij}, describe a probability to radiate parton i from parton j as a function of the momentum fraction z carried away by the offspring parton. in the leading order the splitting functions are of the form:

$$\begin{aligned}
P_{qq}(z) &= C_F\left[\frac{1+z^2}{1-z}\right] \;;\; C_F = \frac{4}{3} \\
P_{gq}(z) &= C_F\left[\frac{1+(1-z)^2}{z}\right] \\
P_{qg}(z) &= T_R\left[z^2+(1-z)^2\right] \;;\; T_R = \frac{1}{2} \\
P_{gg}(z) &= 2C_A\left[\frac{1-z}{z} + \frac{z}{1-z} + z(1-z)\right] \;;\; C_A = 3
\end{aligned} \tag{1.7}$$

The partons participating in the scattering can be any of the valence and sea quarks or gluons, where the dominance of either type of the partons changes with x and Q^2 (Fig. 1.10). There are various PDF sets based on the various data and theory interpretation: CTEQ [73], HERAPDF [74], PDF4LHC [75], etc.

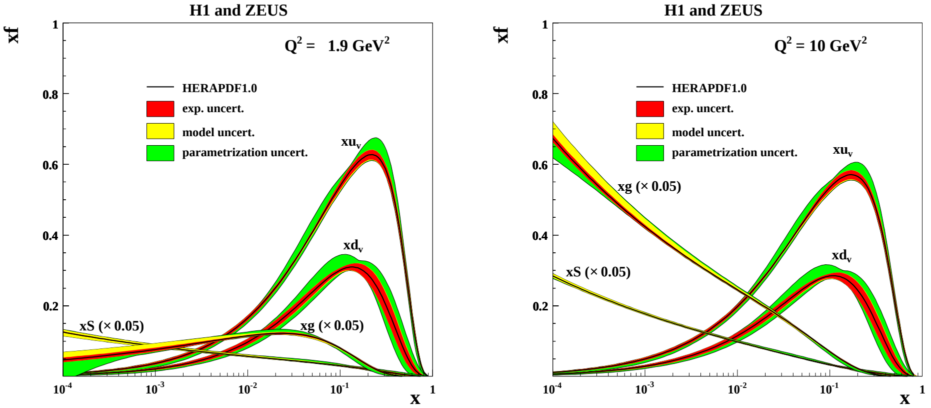

Figure 1.10: The parton distribution functions from HERAPDF1.0, valence quarks $\mathrm{xu_v}$; $\mathrm{xd_v}$; sea quarks $\mathrm{xS} = 2\mathrm{x}(\bar{\mathrm{U}} + \bar{\mathrm{D}})$; gluons xg, at $Q^2 = 1.9\ \mathrm{GeV}^2$ (left) and $Q^2 = 10\ \mathrm{GeV}^2$ (right). The gluon and sea distributions are scaled down by a factor 20. The experimental, model and parametrization uncertainties are shown separately [76].

1.3.3 Fragmentation functions

Partons, due to the color confinement, cannot be observed in the laboratory. The hard scattered partons, in the initial stage of the hard scattering, are highly virtual and they radiates gluons in order to “shake-off” the initial virtuality (more details in section 1.3.5.). When the virtuality is reduced close to the hadronic scale ($\approx 1\ \ \mathrm{GeV}/c$) then the hadronization process (modeled e.g. by Lund string model [77]) takes place. The fragmentation function describes the distribution of the fractional momenta of particles radiated from the parton.

The momentum fraction z is defined as a longitudinal momentum fraction of jet momentum p_{jet} carried away by the jet fragment p_{part}

$$z = \frac{\vec{p}_{\mathrm{part}} \cdot \vec{p}_{\mathrm{jet}}}{p^2_{\mathrm{jet}}} = \left.\frac{p_{\mathrm{part}}}{p_{\mathrm{jet}}}\right|_{\vec{p}_{\mathrm{part}} \times \vec{p}_{\mathrm{jet}} = 0}$$

Fragmentation function $D(z)$ is then defined as the “average multiplicity m of jet fragments having $z > z_0$” [78]

$$m(z_0) = \int_{z0}^{1} D(z)\mathrm{d}z \quad \Rightarrow \quad m(0) \equiv \langle m \rangle = \int_0^1 D(z)\mathrm{d}z$$

The momentum conservation requirement, sum of all jet fragments must equal to the jet momentum, implies

$$\sum_i p_{i,\mathrm{part}} = p_{\mathrm{jet}} \Rightarrow \sum_i z_i = 1 \Rightarrow \int_0^1 z\ D(z)\mathrm{d}z = 1$$

Here we ignore the transverse momentum components of jet fragments. These transverse components are coming from the jet virtual mass. One interesting consequence is that $\langle z \rangle = 1/\langle m \rangle$

$$\langle z \rangle = \frac{\int_0^1 z\, D(z) \mathrm{d}z}{\int_0^1 D(z) \mathrm{d}z} = \frac{1}{\langle m \rangle}$$

It is important to note that fragmentation function does not represent the probability density function $D(z) \neq dP_{\mathrm{part}}/\mathrm{d}z$. It represent the average multiplicity density $dm/\mathrm{d}z$. Generally, particles coming from the quark jets are having quite substantially harder spectrum than fragments of the gluon jets [79].

Fragmentation function measurement is usually performed in e^+e^- collisions where the collision kinematics is better controlled. The momentum fraction x distribution for a given hadron h in $e^-e^+ \to \gamma, Z \to h + X$ process can be calculated as

$$\frac{\mathrm{d}\sigma_h}{\mathrm{d}x} = \sum_c \int_x^1 \frac{\mathrm{d}z}{z} C_c(z, \alpha_s(\mu), Q, \mu) D_{c \to h}(x/z, \mu) \tag{1.8}$$

where the c goes through parton flavors; C_c denote production probability of parton c in a short-distance process; and $D_{c\to h}$ is a fragmentation function of parton c fragmenting to hadron h.

1.3.4 Jets

The final state particles originating from the parton fragmentation described in section 1.3.3 form a collimated spray of particles known as jet. Jets were first observed by SPEAR collaboration [80, 81], where di-jet events originating from $q\bar{q}$ pair coming from e^+e^- annihilation have been studied. First observation of 3-jet events, including two quark and one gluon jet, happened at PETRA accelerator [82–85]. It has been shown that such entity, the jet [86], is well in reach of pQCD computation. In such case the Eq. (1.5) can be changed to provide jet cross section by replacing the $D_{c\to h}$ with $\delta(1-z)$. Fig. 1.11 shows examples of jet cross section measurements (for CDF left, LHC right) on hadron collider experiments, overlaid by the NLO pQCD calculation curves. The agreement between the data and the NLO calculation is excellent. One of the reason is that the jet cross section is not influenced by the uncertainty coming from the fragmentation function as it is in the case of the analysis of the hadronic cross section. An example of the influence of the fragmentation function uncertainty is discussed in section 5.4.1.

Jet algorithms

Jet is an object which depends, to some extend, on its definition. What final state hadrons will be combined into a single jet depends on the jet definition (for example cone size, choice of the jet algorithm or scale which defines how hard radiated

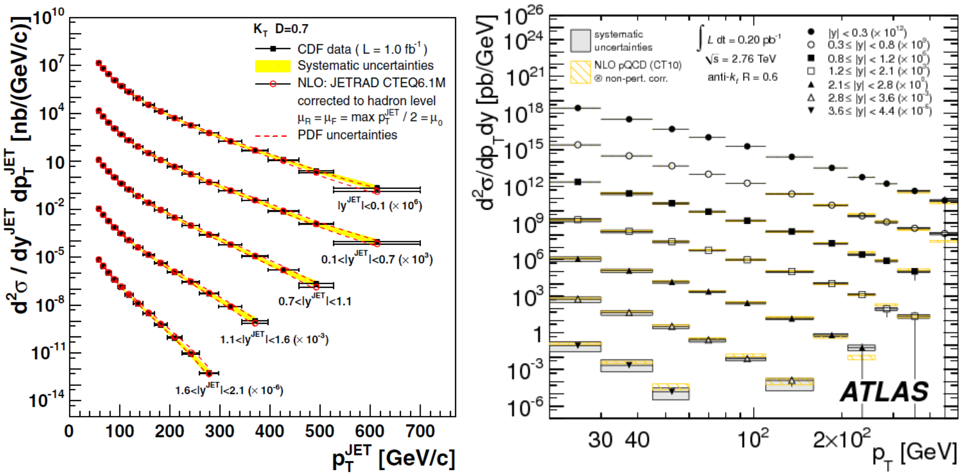

Figure 1.11: Examples of inclusive jet cross sections with theory fits. Left: CDF collaboration p$\bar{\text{p}}$, $\sqrt{s} = 1.96$ TeV. The data for other bins than $0.7 < |y^{\text{jet}}| < 1.1$ are scaled by factors $10^{\pm 3}$ consecutively for better visibility [87]. Right: ATLAS collaboration p–p, $\sqrt{s} = 2.76$ TeV. Similar scaling used as for the left plot, with unscaled bin $2.1 < |y^{\text{jet}}| < 2.8$ [88].

gluon will still be part of a jet). Jet definitions are ideally collinear and infrared safe. Term collinear safety describes immunity of jet finder against splitting or emission of a collinear particle, infrared safety is immunity against merging two separate jets when a soft particle is radiated in between them.

Algorithms that cluster the detected final state particles into jets are called jet finding algorithms. Those can be separated into two larger groups (i) cone algorithms and (ii) sequential recombination algorithms.

The cone algorithms optimize a position of a fixed size cone inside acceptance. They are usually based on finding a seed to start with and are often infrared or collinear unsafe (with exception of the SISCone algorithm [89]).

The sequential clustering algorithms use a distance measure in between two particles $d_{ij} = \min\left(k_{\text{T},i}^{2p}, k_{\text{T},j}^{2p}\right) \frac{\Delta_{ij}}{R}$ where the Δ_{ij} is distance of particles in azimuth-rapidity plane and R is a "radius" parameter. Distance to beam $d_{iB} = k_{\text{T},i}^{2p}$ is also used, usually as a cutoff to stop jet clustering. The algorithms differ in the value of p, which gives them different behaviors like preferring harder particles to start clustering and keeping a rather circular shape (anti-k_T algorithm [90], p = -1) or starting from soft particles and having a very vague shape (k_T algorithm [91], $p = 1$).

1.3.5 Parton shower evolution

Partons that underwent hard scattering (Fig. 1.12) act as a free colored object before it is able to hadronize and produce final state color singlet. In case of scattered $q\bar{q}$ pair for example, the scattered quarks can be seen as losing a part of their proper fields in the scattering. The regeneration time of the proper field can be linked with the time when the parton can enter hadronization t_{hadr}. The time in between scattering and hadronization is then governed by perturbative QCD processes which do evolve the initial parton into a partonic shower.

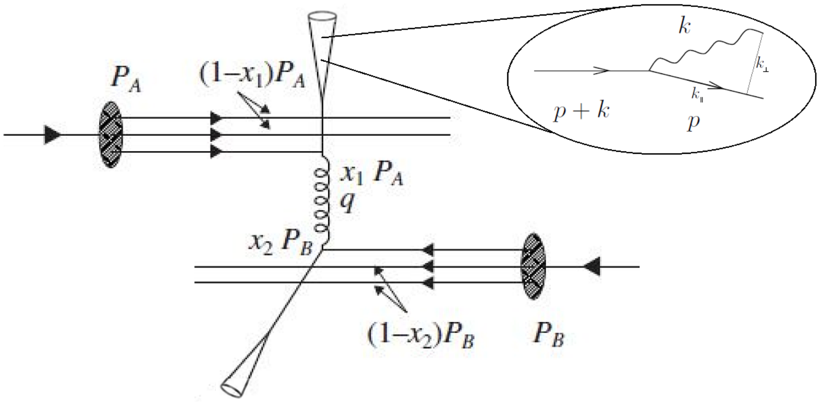

Figure 1.12: Schematics of parton scattering in p–p collision and kinematics of gluon emission. Two partons scatter with momentum fractions x_1 and x_2 of the incoming protons P_A and P_B respectively. The outgoing parton with momentum $p+k$ then emits gluons with momentum k.

The regeneration time for a proper filed component with momentum k can be written as

$$t_{\mathrm{regen}}(k) \approx \frac{k_\parallel}{k_\perp^2}$$

the momenta in the rest frame of the hadron can be approximated by hadronic size R, $k'_\perp \sim k'_\parallel \sim R^{-1}$ and moving back to lab frame $k_\perp \sim k_\perp \sim R^{-1}$, $k_\parallel = \gamma k_\parallel = E/mR$, $\gamma = E/m$ one gets

$$t_{\mathrm{regen}}(k) \approx \frac{\gamma k'_\parallel}{{k'_\perp}^2} \approx \frac{ER^{-1}}{m}\frac{1}{R^{-2}} = \frac{E}{m}R$$

where the $k_\perp$ and $k_\parallel$ are perpendicular and parallel fractions of the radiated gluon in respect to the outgoing quark (see Fig. 1.12), R is the hadronic size, E and m are energy and mass of the quark [92].

Thus for an example light quark ($m_{\mathrm{constituent}} \sim \sqrt{k_\perp^2} \sim R^{-1}$) of E = 200 GeV, the $t_{\mathrm{hadr}} \sim ER^2 \sim 10^2$ fm/c. The time before the hadronization is in the $q\bar{q}$ example filled by gluon QCD Bremsstrahlung.

Still in the example of the $q\bar{q}$ scattering, the differential spectrum of the gluon radiation can be written as [92]

$$d\omega_{q\to qg} = \frac{\alpha_s(k_\perp^2)}{4\pi} 2C_F \left[1 + \left(1 - \frac{k}{E}\right)^2\right] \frac{dk}{k} \frac{dk_\perp^2}{k_\perp^2}$$

The spectrum exhibits double logarithmic dependency on k and k_{perp}.

If a gluon shall be radiated, than the formation time of the radiation t_{form} must be smaller than the hadronization time

$$\begin{aligned} t_{\text{form}} &\approx \frac{k}{k_\perp^2} \\ t_{\text{form}} &\sim \frac{k}{k_\perp^2} < t_{\text{hadr}} \sim kR^2 \end{aligned}$$

which leads to condition $R^{-1} < k_\perp$. A possible ordering of

$$R^{-1} \ll k_\perp \ll k \ll \sqrt{Q^2}$$

which in words means that t_{hadr} is much larger than t_{form}. This will lead to a cascade of gluon radiation that produces large number of partons in a collimated shower.

Coherent emissions and angular ordering

Formation time t_{form} of large angle gluon radiation is too short to allow the mother parton separate enough form the preceding branching. The separation $\rho_{q\bar{q}}$ of the two colored objects from the preceding branching is below the resolution level of the arising gluon given by its transverse wavelength $\lambda_\perp$, or opening angle θ_{qg} in respect to mother parton, Eq. (1.9). The gluon can not resolve then the two colored objects ($\rho_{q\bar{q}} < \lambda_\perp$). As such it is probing the summed color of the two partons (color of the mother parton) and can be seen as radiating from the mother parton (Fig. 1.13).

$$\begin{aligned} t_{form} &\approx \frac{1}{k\theta_{qg}^2} \approx \frac{k}{k_\perp^2} \\ \rho_{q\bar{q}} &\approx \theta_{q\bar{q}}\, t_{\text{form}} \approx \frac{1}{k_\perp} \frac{\theta_{q\bar{q}}}{\theta_{\text{qg}}} \\ \lambda_\perp^{-1} &= k_\perp \end{aligned} \tag{1.9}$$

Large angle soft gluon radiation is then independent on the amount of the parton branchings because it is probing the state of the initial parton. The amount of large angle radiated gluons then does not increase with increasing amount of the partons in

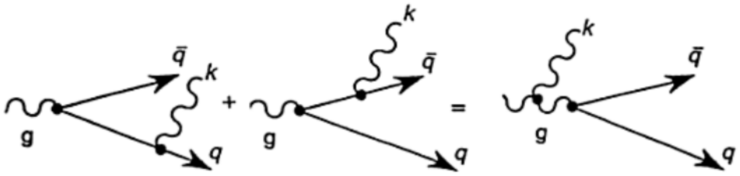

Figure 1.13: Wide–angle emission of soft gluon k, of q and $\bar{q}$, acts as if the emission came of the parent g imagined to be on shell [92].

the shower. The yield of the soft gluons can be considered as being suppressed by the color coherence [93].

The color coherence leads to effect, when new branching from the increasing amount of partons are preferred for the cases when the gluons are able to resolve the previous parton pair, i.e.: the transverse wavelength which can be linked to the opening angle is smaller than the opening angle of the previous branching. It is then preferred that consecutive branching opening angles follow the ordering $\theta_1 > \theta_2 > \theta_3,$ *etc.* (Fig. 1.14). The effect is called angular ordering [94–96].

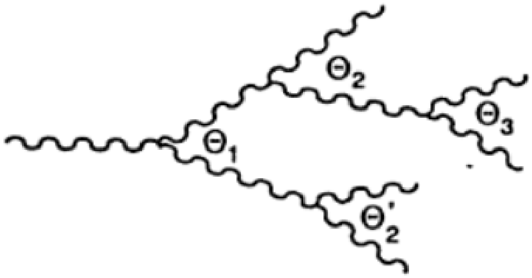

Figure 1.14: Angular ordering in parton shower. $\theta_1 > \theta_2 > \theta_3,$ *etc.* [92]

Logarithmic approximations

The momentum transfer Q^2 in a hard process sets limit on the $k_\perp$ of the produced partons Eq. (1.10). Probability of parton production is then Eq. (1.11), in other words: for higher Q^2 branching of additional partons becomes more probable.

$$d\omega \propto \frac{\alpha_s}{\pi}\int^{Q^2}\frac{1}{k_\perp^2}dk_\perp^2 \tag{1.10}$$

$$\omega \propto \frac{\alpha_s}{\pi}\ln Q^2 \sim 1 \ , \quad \frac{\alpha_s}{\pi} \ll 1 \tag{1.11}$$

The Leading Log Approximation (LLA) keeps track of corrections of order $(\alpha_s/\pi \cdot \ln(Q^2))^n$ and neglects other that are not accompanied by the large logarithm. The LLA successfully describes the breaking of Bjorken scaling, $F(x, Q^2)$ dependence.

The Double Logarithmic Approximation (DLA) Eq. (1.12) targets description of the soft collinear gluon radiation in jets, using the color coherent angular ordering effect [93,97,98]. The summation of only the double logarithmic terms $(\alpha_s/\pi \cdot \ln^2(Q^2))^n$ is performed. With taking into account the soft collinear gluon radiation, the DLA can predict, with some limits, particle multiplicities in jets. The DLA tends to overestimate the branching, because it operates in soft limit, ignores recoil of the mother parton (energy of radiation mother parton remains unchanged before and after radiation).

$$\frac{\alpha_s}{\pi} \ll 1 \quad , \quad \frac{\alpha_s}{\pi} \ln Q^2 \ll 1 \quad , \quad \frac{\alpha_s}{\pi} \ln^2 Q^2 \sim 1 \tag{1.12}$$

The single logarithm corrections $\alpha_s \ln Q^2$ that miss in the DLA are important for accounting of hard collinear gluon radiation. The DLA and LLA were taken as a basic stones to create the Modified Leading Logarithm Approximation (MLLA) [99], which still keeps the probabilistic approach of the DLA and include the single logarithmic correction terms. In this way the MLLA is keeping a better track of the energy conservation in the developing parton shower.

Comparison of MLLA calculation to data [100] showed that the MLLA prediction of jet fragmentation transverse momentum j_{T} still overestimates the hard part of the spectra. To improve the energy conservation description in MLLA, and limit the overestimations, a higher order corrections can be included in the computation. This is called Next-to-Modified Leading Logarithm Approximation (NMLLA) [101, 102].

Local parton hadron duality

The jet evolution is first describable up to a certain cutoff by the pQCD followed by colored charge blanching and hadronization of the partons. The two stages being separated by a cutoff energy.

There is no definite model to describe the process of turning parton shower into final state hadrons. A hypothesis was formulated in [99], that there can an a constant scale in between the parton and final hadron distribution. During the hadronization, a local charge blanching would turn the partons into hadrons, without being effected by longer range interactions, thus the final hadron distinction would resemble very much the initial parton distribution. Hence the name Local Parton Hadron Duality (LPHD).

The later stages of the pQCD part of parton shower evolution govern the final particle distributions into large extent, simply due to multiplicity of the partons. A scale to which the pQCD showering is used to describe the evolving jet defines the balance between pQCD and hadronization. The scale set to $\approx \Lambda_{QCD}$ can be used to give duality in between partons and light hadrons.

It should be noted, that the hypothesis does not enforce the duality to function on event–by–event bases, but rather averaged over larger statistics. The LPHD is an important part of MLLA an NMLLA predictions of j_{T}.

Humpback plateau

The DLA or MLLA, together with LPHD can provide prediction for final state particle energy spectrum inside jets. The soft gluon radiation is constrained by the condition $R^{-1} < k_{\perp} \rightarrow (kR)^{-1} < \theta$ coming from necessity of hadronization time being larger than the radiation formation time. On the other hand, the color coherence lowers the probabilities of the large angle gluon emissions due to the angular ordering of subsequent emissions. Thus the parton energy spectrum inside a jet shall be influenced by depletion in the lower energy region [103].

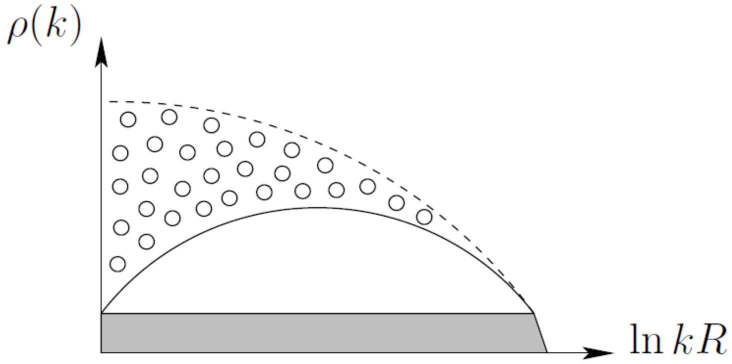

Figure 1.15: The effect of color coherence on particle energy spectrum $\rho(k) = \mathrm{d}n/\mathrm{d}\ln(k)$. Dotted area corresponds to the contribution which is removed when turning from the incoherent model (dashed) to the coherent one (solid). Shaded area shows the old-fashioned plateau, without taking account of bremsstrahlung [92]

Fig. 1.15 shows the sketch of the effect. The displayed spectrum is depleted in soft region after coherent radiation model is considered, on contrary to situation where the incoherent radiation model is assumed. The depletion results in a specific humpback shape of the spectrum. Fig. 1.16 shows the comparison of the theory curves obtained from the MLLA theory to the data. The data show humpback shape of the spectrum. The NMLLA theory curves of the coherent branching reproduce the data well.

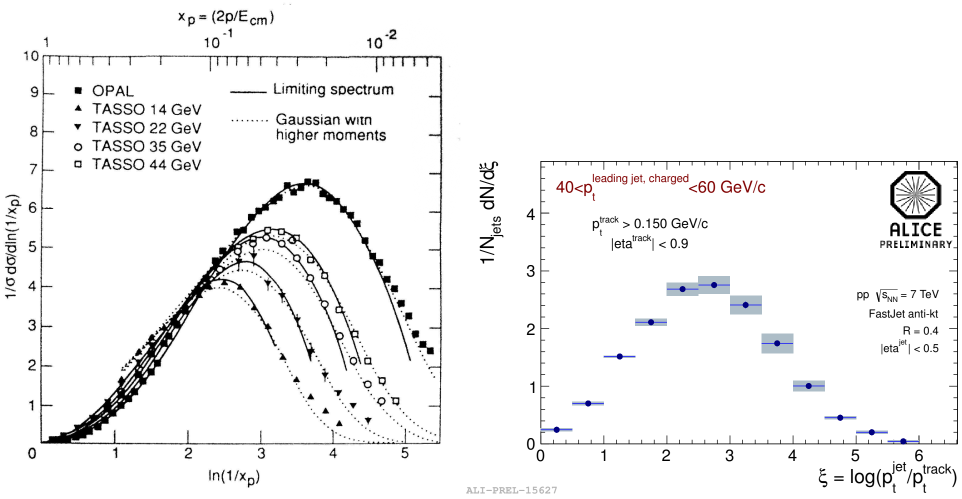

Figure 1.16: Left: $\ln(1/x_p)$ distributions of charged hadrons at $E_{\mathrm{cm}} = 14$, 22, 35, 44 and 91 GeV compared with distorted Gaussian and evaluated MLLA limiting distribution [92] [104]. Right: ALICE p-p $E_{cm} = 7$ TeV.

1.4 Nuclear matter effects

Presence of nuclear medium around the point of a hard scattering event results in interaction of the products of the hard scattering with the matter. The initial conditions before the hard scattering can also be altered. In case of the strongly interacting hot and dense QGP, the propagating partons can radiate gluons in vicinity of scattering centers, which is called induced gluon radiation [105]. Mean energy loss of a parton in medium can then be described by the medium transport coefficient [106]. For the heavier quarks, energy loss from elasatic re-scattering needs to be also considered.

Nuclear effects can also arise from presence of "cold" nuclear matter. For example initial state effects as shadowing and anti-shadowing [107] or Cronin [108] effect have been observed in p–A or d–A collisions. When observing modifications in between pp and A–A collisions, it is important to study the effects of cold nuclear matter as well, to be able to correctly disentangle the initial and final state modifications.

1.4.1 Jet quenching

The partons propagating through medium lose energy, their p_{T} is lowered. The energy loss then demonstrates as suppression of final state p_{T} hadrons (jet quenching). The effect energy loss in the inclusive transverse spectra can be quantified with nuclear modification factor

$$R_{\mathrm{AA}}(p_{\mathrm{T}}) = \frac{d^2N/dp_{\mathrm{T}}dy|_{\mathrm{AA}}}{\langle T_{\mathrm{AA}}\rangle\, d^2\sigma/dp_{\mathrm{T}}dy|_{pp}} \tag{1.13}$$

where the nuclear overlap function $\langle T_{\mathrm{AA}}\rangle$ is related to the average number of inelastic nucleon-nucleon collisions as $\langle T_{\mathrm{AA}}\rangle = \langle N_{\mathrm{coll}}\rangle / \sigma_{\mathrm{inel}}^{pp}$. N_{coll} is a scaling of binary collisions based on Glauber modeling [38]. $R_{\mathrm{AA}} = 1$ represents no modification by nuclear matter. R_{pA} is defined analogically.

The nuclear modification factor can be constructed for final state particles which come from processes that are affected by the interaction with medium same as for particles which are expected to traverse the medium without interacting with it, for example photons. Observation of R_{AA} for various particle species is shown on Fig. 1.17. A large suppression of production of hadrons in central A–A collisions is observed, on contrary to p–A or peripheral A–A collisions. Also the photon and intermediate vector boson yields seen unchanged.

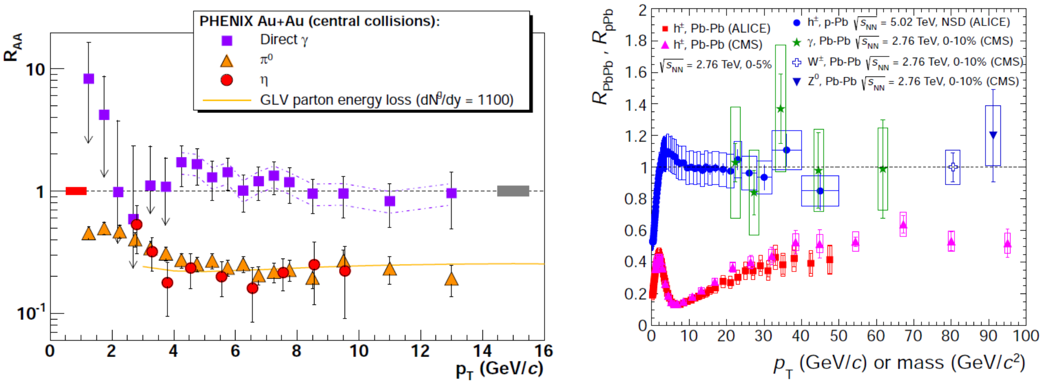

(a) (b)

Figure 1.17: (a) R_{AA} (p_{T}) measured in central Au+Au at $\sqrt{s_{\mathrm{NN}}} = 200$ GeV for η, π^0 and direct γ [109]. The pp reference for γ measurement is NLO calculation. The solid yellow curve is a parton energy loss prediction. (b) Transverse momentum dependence of the nuclear modification factor R_{pPb} of charged particles ($h^{\pm}$) measured in minimum-bias (NSD) p–Pb collisions at $\sqrt{s_{\mathrm{NN}}} = 5.02$ TeV in comparison to data on the nuclear modification factor R_{PbPb} in central Pb–Pb collisions at $\sqrt{s_{\mathrm{NN}}} = 2.76$ TeV. [110].

Two particle correlation method also provides a good handle to study the jet quenching. The yields of particles associated to a high-p_{T} trigger are studied in azimuth (or rapidity) e.g. by PHENIX [52]. The azimuthal hadronic correlation produce a specific function shape (Fig. 1.18). The shape originates from the fact that due to the in-medium energy loss it is likely that a high-p_{T} hadron originates from a hard scattering close to medium surface [111]. The recoiling (away side, $\Delta\varphi = \pi$) jet is expected to traverse the medium and get quenched more that the trigger one (near side, $\Delta\varphi = 0$). Vanishing of the away side yields is another sign of energy loss induced by medium.

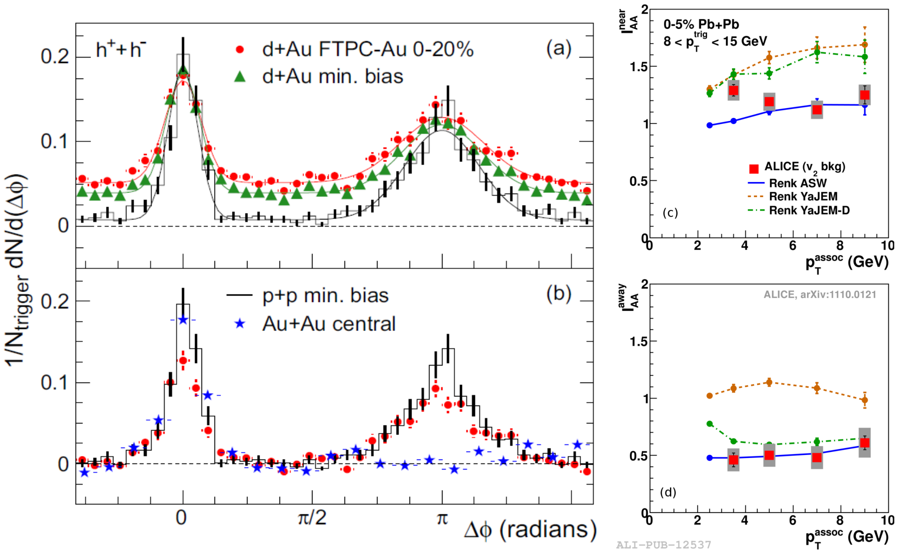

Figure 1.18: (a) Efficiency corrected two-particle azimuthal distributions for minimum bias and central d–Au collisions, and for pp collisions. (b) Comparison of two-particle azimuthal distributions for central d–Au collisions to those seen in pp and central Au–Au collisions. [112] (c),(d) Charged hadron I_{AA}, $p_{\mathrm{T,trig}}$ = 8-15 GeV (background subtraction: v2). Compared to T. Renk [111] [113]. Near side (c), away side (d).

The correlated yields I_{AA} Eq. (1.14) can be constructed as ratio of near or away side yields Y in A–A and pp collisions

$$I_{\mathrm{AA}} = \frac{Y^{\mathrm{AA}}(p_{\mathrm{Tassoc}}, \eta)\big|_{p_{\mathrm{T,trigg}}}}{Y^{\mathrm{pp}}(p_{\mathrm{Tassoc}}, \eta)\big|_{p_{\mathrm{T,trigg}}}} \tag{1.14}$$

1.4.2 Cold nuclear matter

Low-x partons in nucleus have higher chance of recombination with another parton inside the nucleus and thus creating a higher-x particle [107]. This effect is called shadowing and leads to lowering of hadron spectra in range below the 2 GeV/c. On the other hand, when energy conservation is considered, the recombined parton will increase yields of the final state hadrons in the higher p_{T} region, this is called anti-shadowing [114].

In addition to (anti)shadowing, the nuclear matter contributes to the non-zero transverse momentum of parton k_{T}. Given the total k_{T} as a sum of contributions $\langle k_{\mathrm{T}}\rangle \approx \langle k_{\mathrm{T,Fermi}}\rangle + \langle k_{\mathrm{T,NLO}}\rangle + \langle k_{\mathrm{T,SoftQCD}}\rangle$, the presence cold nuclear matter alter the NLO and Soft QCD contributions, which will lead to harder hadron production and larger di-jet acoplanarity. As a consequence, the aways side part of two particle correlation function is expected to be widened.

The discussed cold nuclear matter effects occur at the initial state and can be accounted for in theory by modifying the nuclear PDFs.

Chapter 2

Experimental setup

2.1 The Large Hadron Collider

The Large Hadron Collider (LHC) [1] is a collider facility designed to deliver collisions of protons and nuclei. The maximal dipole magnetic filed of 8.33 Tesla allows for energies up to 7 TeV for protons and 2.76 TeV per nucleon for lead ions (14 TeV and 5.5 TeV in colliding system center of mass respectively). The two-in-one magnet design of the LHC does not allow for different energies of the clockwise and counter-clockwise beams. Center of mass of the non-symmetric colliding system moves in the laboratory frame in direction of the more energetic beam. Luminosity is expected to rise up to $10^{34}\text{cm}^{-2}\text{s}^{-1}$ for pp and $10^{27}\text{cm}^{-2}\text{s}^{-1}$ for the Pb–Pb running. Up to the point of writing of this thesis, the LHC delivered collisions at center of mass of $\sqrt{s}$ = 900 GeV, 2.76, 7 and 8 TeV for pp, $\sqrt{s_{\text{NN}}}$ = 2.76 TeV for Pb–Pb and $\sqrt{s_{\text{NN}}}$ = 5.02 TeV for p–Pb (in both directions). The luminosities delivered are shown on Fig. 2.1.

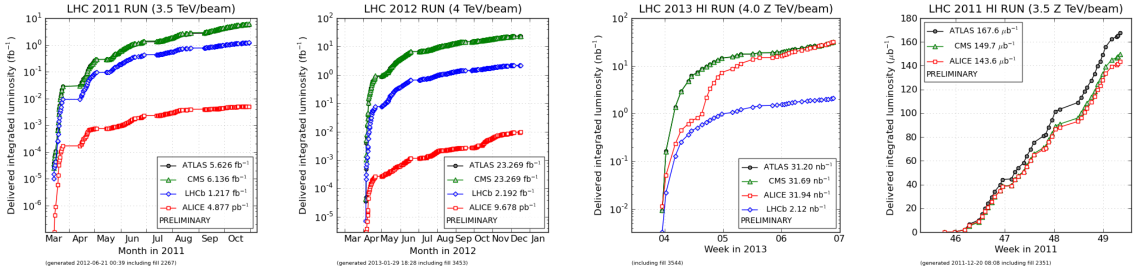

(a) (b) (c) (d)

Figure 2.1: The luminosities delivered by the LHC to the four experiments. For the pp running of 7 (a) and 8 TeV (b), p–Pb (c) and Pb–Pb (d).

The LHC is the latest stage of the accelerator complex at CERN (Fig. 2.2). Circumference of the LHC is 27 km, the ring is 50 to 170 meters under ground. It is composed of 1232 dipole and 392 quadrupole magnets with superconducting coils, cooled down to 1.7 K. The radio-frequency (RF) acceleration and injection system operates at 400 MHz frequency (decrease to 200 MHz is foreseen), the main LHC operating frequency is 40 MHz (25 ns bunches). Single bucket (RF slot) out of 10 is filled with a bunch. Out of 3564 possible bunches in the ring, maximum of 2808 are filled. The energy stored in the beam is up to 362 MJ, additionally there are about 600 MJ stored in the magnets.

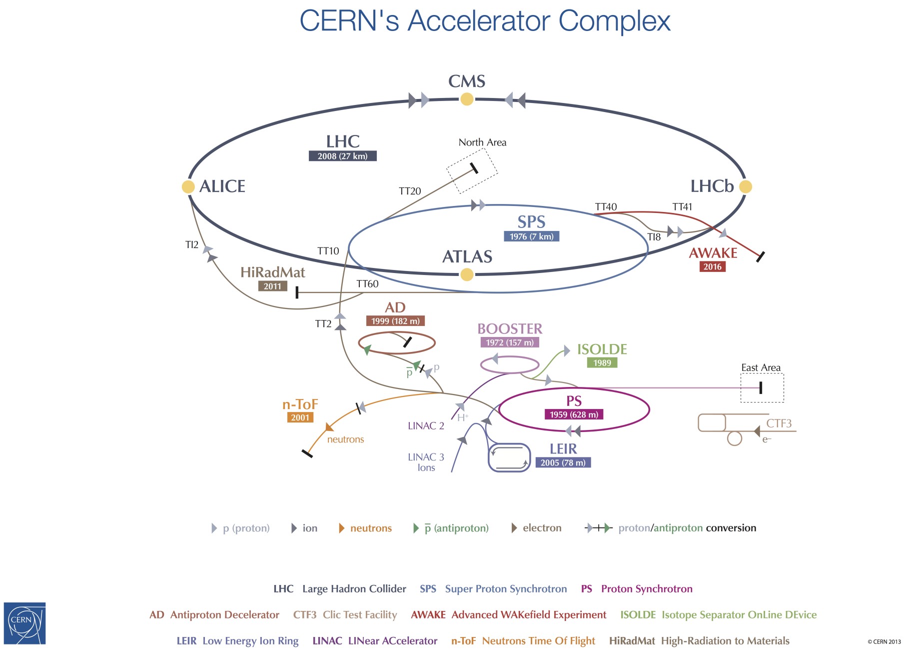

Figure 2.2: The CERN accelerator complex.

The operating cycle for one fill of the LHC can be extended to about 10 hours, thanks to ultra high beam vacuum of about 10^{-10} Torr (equivalent of outer space vacuum at around 1000 km above Earth surface) and to the system of horizontally and vertically focusing quadrupoles. The quadrupoles provide strong focusing [115] of the beam to correct for different angular momenta of the protons in the bunches. A proper series of vertically and horizontally focusing (defocussing in transverse direction) magnets leads to overall beam focusing. The magnets focusing in a given plane are placed at positions, where the deviation from circular orbit is large in the focusing plane, but small in the defocussing plane. The sequence of magnets is optimized to provide minimal betatron oscillation amplitude (β) at the interaction points (narrow distribution in the transverse plain).

The longitudinal profile of the bunch is focused by the property of the RF cavity, which gives higher momentum kick to particles arriving later (the lower momentum ones). The particles escaping the focusing ability of the RF system are still kept oscillating around synchronous position (synchrotron oscillation). This is due to interplay of velocity and orbit length in constant magnetic field. The quadrupole setting define energy threshold, below which the orbit time decreases with increasing momentum and above which the orbit time increases with increasing momentum.

The filling of the LHC requires 12 SPS cycles of 21.6 s. Though due to injection of pilot bunches, recalibration of the machine based on the pilots, ramping the beam and magnets, the theoretical minimum of the LHC turnaround is close to 60 minutes. The turnaround is several hours in the real life operation. Fig. 2.3 shows an example of LHC cycles for 2013 p–Pb period.

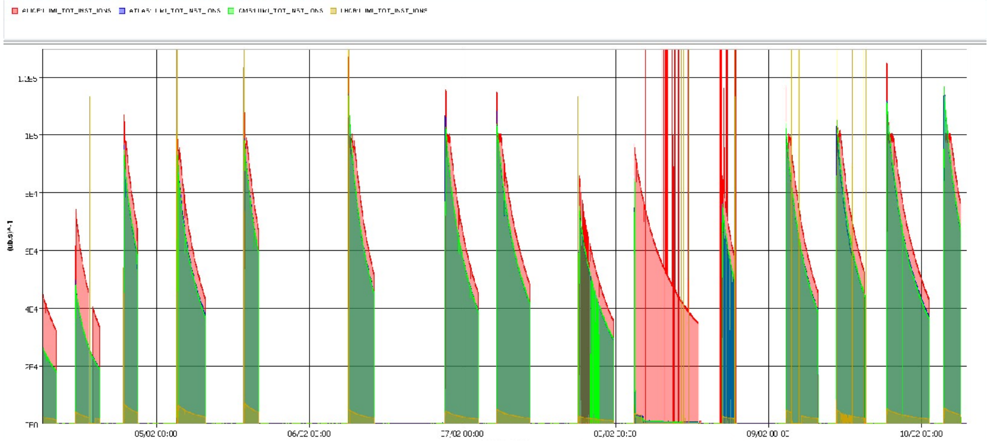

Figure 2.3: The LHC luminosity cycles for the 2013 p–Pb running, spanning over 5 days. The irregular three fills little after middle of the displayed period are Van der Meer scan [116] fills.

The ring is subdivided into 8 octants (Fig. 2.4), each bearing one experimental cavern or beam facility. There are four major experiments located on the LHC ring and several smaller ones. Two multi purpose experiments ATLAS [117] and CMS [118] are targeting mainly the particle physics of the standard model and search for hints beyond the model. The LHCb [119] experiment specializes in study of b quark physics and CP symmetry violation. The ALICE [120] experiment targets the physics of heavy ion collisions.

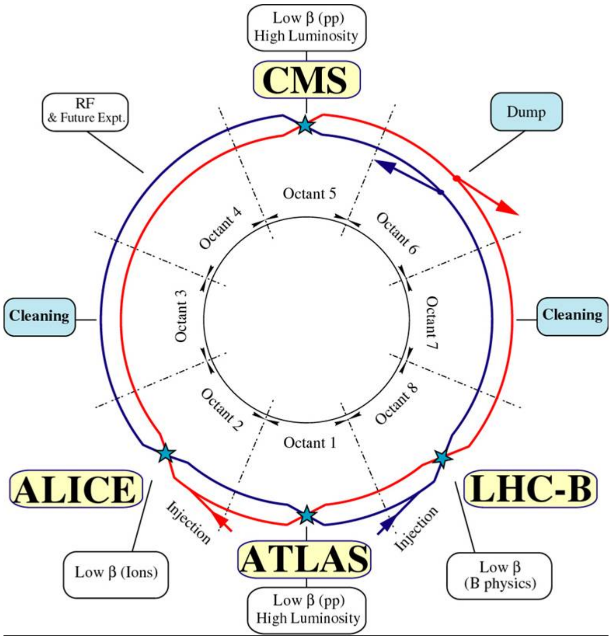

Figure 2.4: LHC schematics with division to the octants.

2.2 A Large Ion Collider Experiment

A Large Ion Collider Experiment (ALICE) scientific program concentrates on study of the strongly interacting hot and dense medium that arises in the heavy ion collisions. For this purpose, ALICE design is optimized for high multiplicity environments of the heavy ion collisions and has powerful particle identification capabilities.

ALICE (Fig. 2.5) central barrel is fully enclosed in 0.5 Tesla solenoid magnet and it's combined tracking covers at least $|\eta| < 0.9$ units of pseudorapidity. There is a forward muon spectrometer [121] outside of the magnet with coverage of $-4.0 < \eta < -2.5$ and equipped with 0.2 Tesla dipole magnet.

The core of ALICE are tracking detectors ordered in the central barrel. The main tracking performance is delivered by the gas filled Time Projection Chamber (TPC) [122] [123] of 88 m^3 with outer radius of 250 cm. There are six layers of silicon based Inner Tracking System (ITS) [124] closer to beam pipe in the barrel. The ITS increases precision for the tracking, especially for low energetic particles, enhances primary and secondary vertexes resolution and provides PID for low energetic particles.

There are two layers of PID detectors outside the TPC; Transition Radiation Detector (TRD) [125] and Time of Flight detector (TOF) [126], additionally there is a partial coverage of High Momentum Particle Identification (HMPID) [127].

Array of forward detectors [128] provide basic collision triggering and centrality measurements (V0), precise collision time and vertex position (T0), forward multiplicity

(FMD), impact parameter (ZDC) and forward photon multiplicity (PMD) measurements.

Electromagnetic calorimetry in ALICE is supported by three detectors with partial coverage; Electromagnetic Calorimeter (EMCal) [129] [130], PHOS [131] and DCal [132].

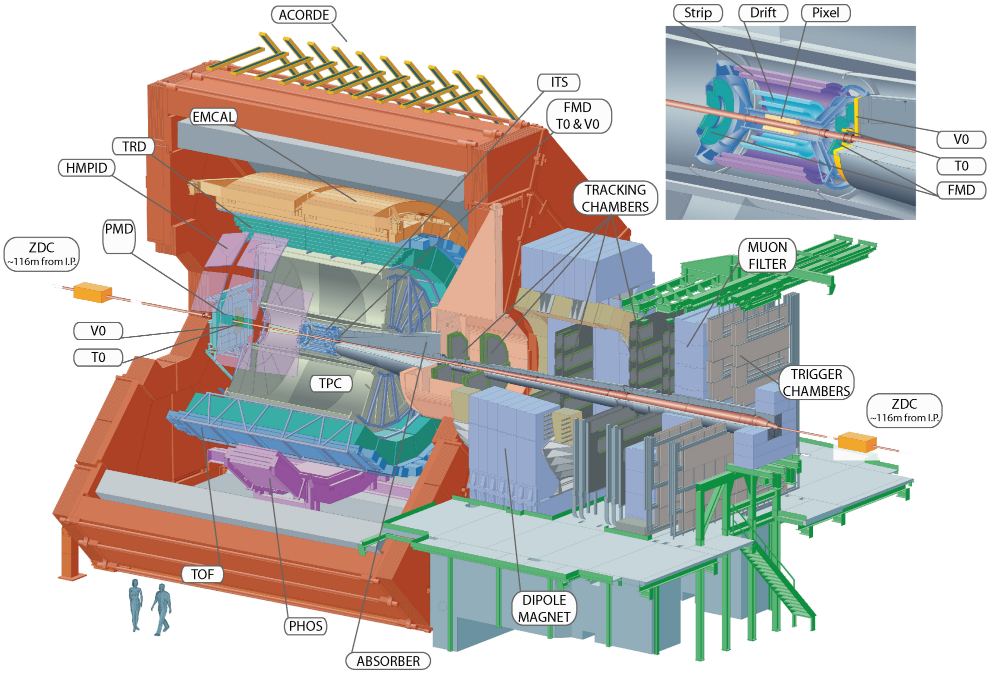

Figure 2.5: The ALICE experiment schematics.

2.2.1 Tracking detectors

Tracking of the charged particles is performed by the TPC and ITS. The TPC is a large drift chamber filled with mixture of neon, carbon dioxide and nitrogen gases. The drift volume is separated into 18 sectors in the azimuth, each having inner and outer readout chamber. The readout is carried out by multi-wire proportional chambers with cathode pad readout (Fig. 2.6). Longitudinally the TPC is separated into two regions each with drift field oriented towards end cap of the detector, separated by the central 100 kV electrode (400 V/cm drift field). Due to the drift time of approx. 88 μs, the event rate of TPC is limited and it is susceptible to pileup events.

The ITS is composed of six silicon layers of three different detector technologies. The innermost two layers are populated with high granularity Silicon Pixel Detectors (SPD), middle layers with Silicon Drift Detectors (SDD) and outer layers with Silicon Strip Detectors (SSD). The four outer layers feature analog readout and are therefore

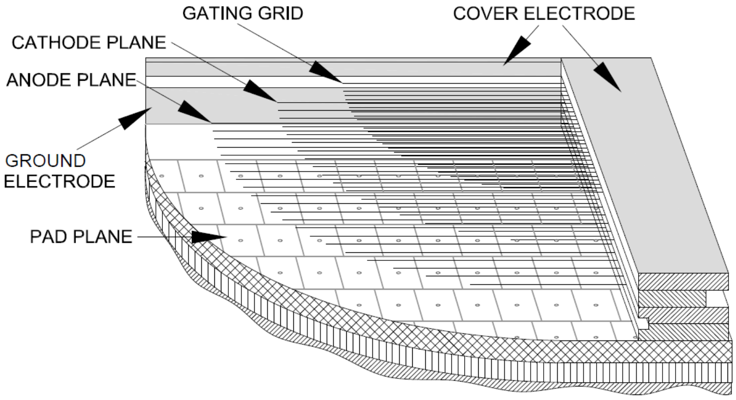

Figure 2.6: The multi wire proportional chamber used in TPC readout.

capable of dE/dx measurements. Spatial resolutions of the silicon technologies are 12×100, 35×25 and 20×830 μm respectively ($r\phi \times z$, where z is along beam axis). Allowing for impact parameter resolution of around 70 μm in $r\phi$.

The performance of TPC and ITS tracking allows to track particles of transverse momenta (p_{T}) up to 100 GeV/c with less than 20% resolution on the momentum and down to 0.1 GeV/c with resolution around 3% (Fig. 2.7) and provides impact parameter resolution and vertex resolutions shown on Fig. 2.8. The ITS vertex resolution is also good enough to allow for detection of decays of single charmed mesons down to approximately p_{T} = 2 GeV/c.

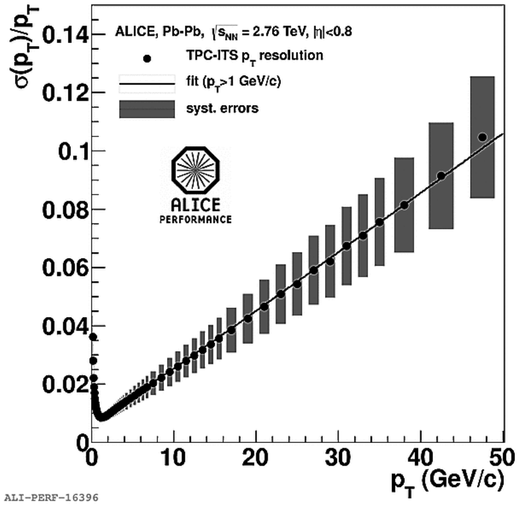

Figure 2.7: Track momentum resolution as a function of p_{T} of combined ITS and TPC tracking.

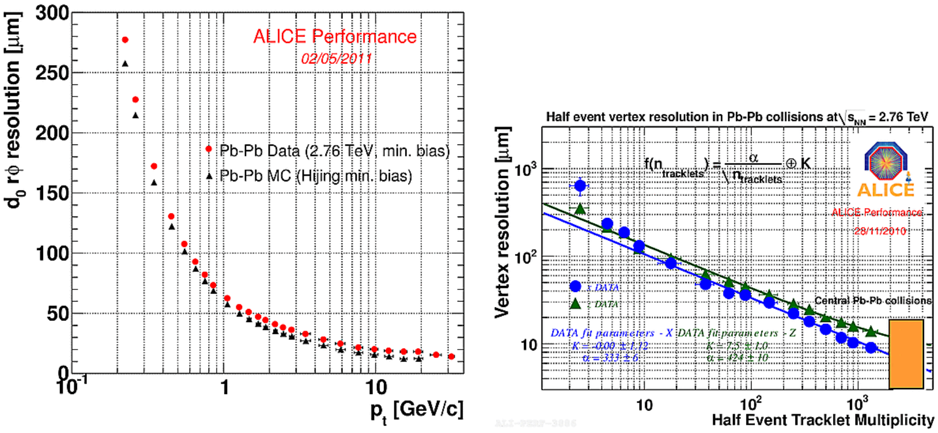

Figure 2.8: Left: ITS transverse impact parameter resolution in Pb-Pb, data and MC. Right: Vertex resolution in Pb–Pb collisions at $\sqrt{s_{NN}} = 2.76$ TeV as a function of half of the tracklets multiplicity of the event.

2.2.2 Particle identification

As already mentioned, the tracking detectors are also capable of particle identification through the dE/dx method. ITS can provide dE/dx for very low momentum particles below approx. $p_\mathrm{T} = 0.2$ GeV/c, TPC for particles below approx. $p_\mathrm{T} = 1$ GeV/c (Fig: 2.9) [133, 134].

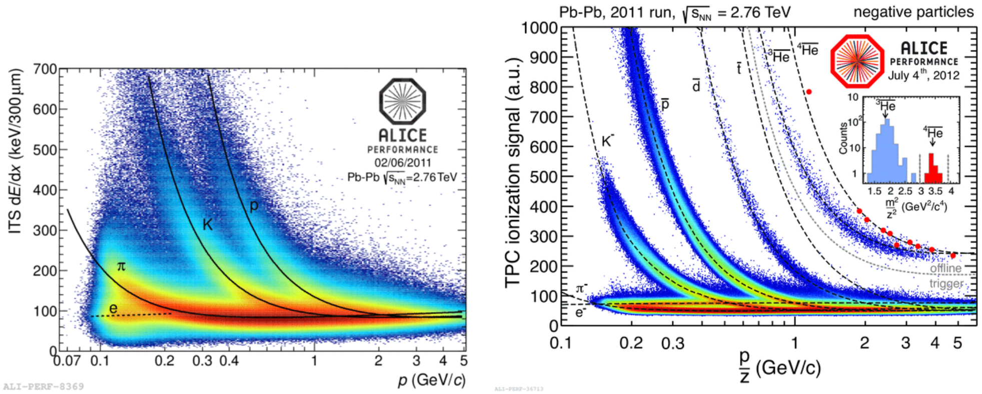

Figure 2.9: Left: ITS dE/dx PID versus particle p_T. Right: TPC dE/dx PID versus particle p_T [135].

The TRD [125] acts primarily as a pion rejection for particle momenta above the TPC electron/pion distinction ability ($p_\mathrm{T} > 1$ GeV/c). Transition radiation photons coming from particles passing through boundary of two media with different refraction indexes are exploited. The TRD is composed of polypropylene radiator, xenon and carbon dioxide filled drift region and multi wire proportional chamber readout. The TRD way of operation is shown on Fig. 2.10. The detector is located right after TPC and is composed of 6 layers of modules. The provided electron/pion rejection is in order of 100.

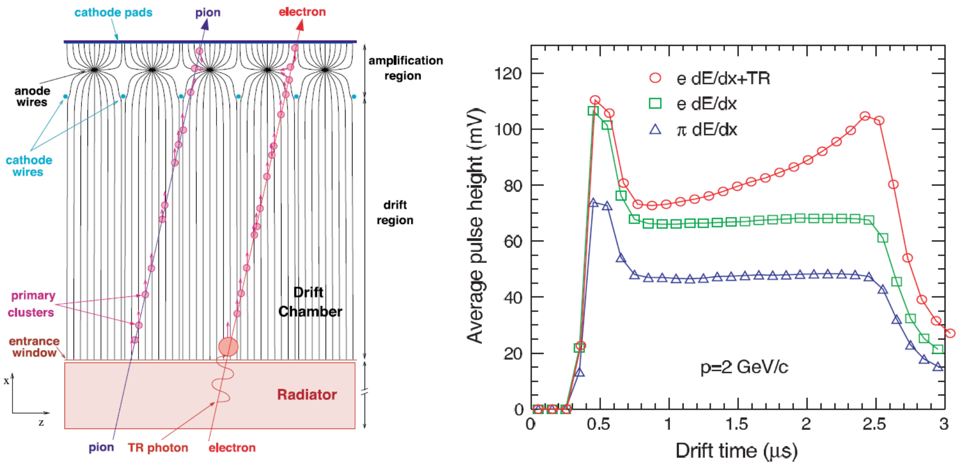

Figure 2.10: Left: TRD module function principle. Right: TRD signal shape as a function of time. Electrons shown with and without the transition radiation [125].

The TOF detector [126] is an array of fast Multi-gap Resistive Plate Chambers, with time resolution in order of 50 ps. The purpose of the TOF is to provide a time of flight PID for charged particles up to $\sim p_{\mathrm{T}} = 4$ GeV/c (Fig. 2.11).

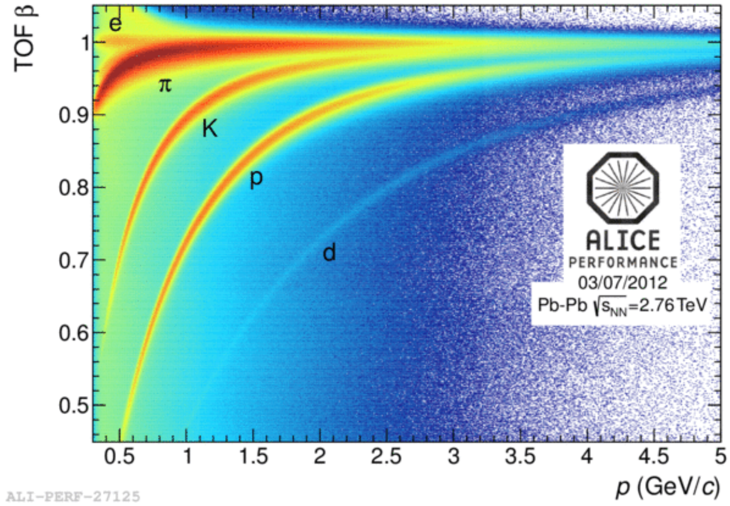

Figure 2.11: TOF β-p performance in Pb–Pb run 2011.

The HMPID [127] is a detector with partial central barrel coverage (about 5%). It uses Cherenkov radiation to extend the PID of charged particles above the PID capabilities of the other central barrel detectors. The detector is composed of C_6F_{14} UV transparent Cherenkov radiator, followed by mutli wire proportional chamber. The gap in between radiator and MWPC is filled with methane and any electrons generated inside are collected by positively charged electrode to prevent them from entering the MWPC sensitive volume (Fig. 2.12). The Cherenkov photons and ionization electrons are read out by CsI coated pad cathode of the MWPC. PID performance of the HMPID is shown on Fig. 2.13. With the HMPID it is possible to differentiate pions from kaons up to ∼3 GeV/c and kaons from protons up to ∼5 GeV/c.

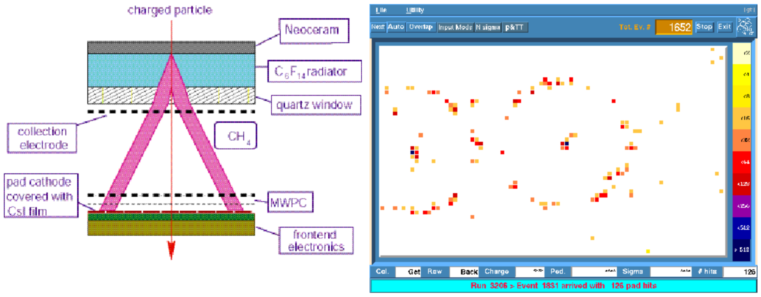

Run 3206 > Event 1831 arrived with 126 pad hits

Figure 2.12: Left: HMPID function principle. Right: Signal example in HPMID [127].

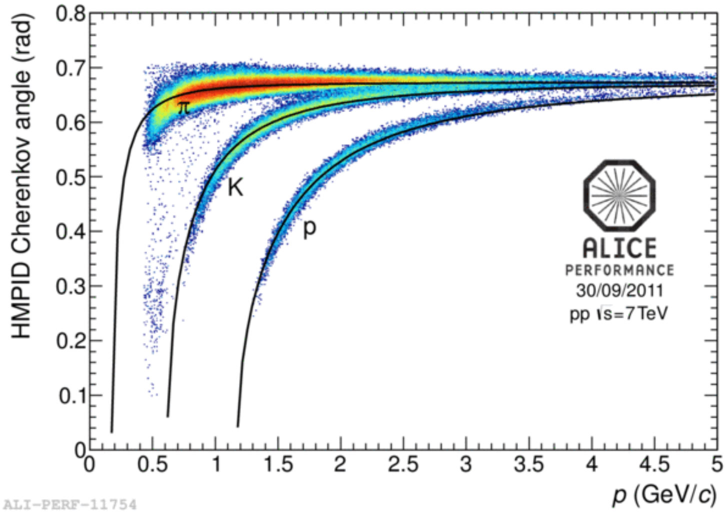

ALI-PERF-11754

Figure 2.13: HMPID particle identification performance [135].

2.2.3 Calorimetry

The ALICE EMCal detector [130] is a sampling calorimeter of shashlik design and consists of 10 full size super-modules (SM) that cover the pseudorapidity range $|\eta| < 0.7$ and 100 degrees in azimuth and two additional 1/3 size SMs, which increase the coverage in azimuth by 6.6 degrees. One SM consists of 1152 towers, each with individual avalanche photodiode readout. The tower dimensions are $6 \times 6 \times 24.6$ cm^3 with an average Moliere radius of 3.20 cm. The DCal is technologically identical to EMCal. The DCal coverage spans over 67 degrees in azimuth, but only 2/3 coverage in pseudorapidity in respect to EMCal super modules, as the mid rapidity region is occupied by the PHOS. In between PHOS and DCal active volumes, there is a gap of 10 cm. DCal is fully back-to-back with EMCal. The EMCal will be discussed in much more detail in the following section 2.3.

The PHOS is a calorimeter with higher granularity (Fig. 2.14) than EMCal (tower size of $2.2 \times 2.2 \times 18$ cm^3), led glass scintillator and identical readout to EMCal. The whole PHOS is kept at -25 degrees of Celsius temperature to increase the light yield of the scintillator crystal by factor of 3 in respect to room temperature. PHOS covers 70 degrees in azimuth and $|\eta| < 0.12$. It is fully back-to-back with EMCal.

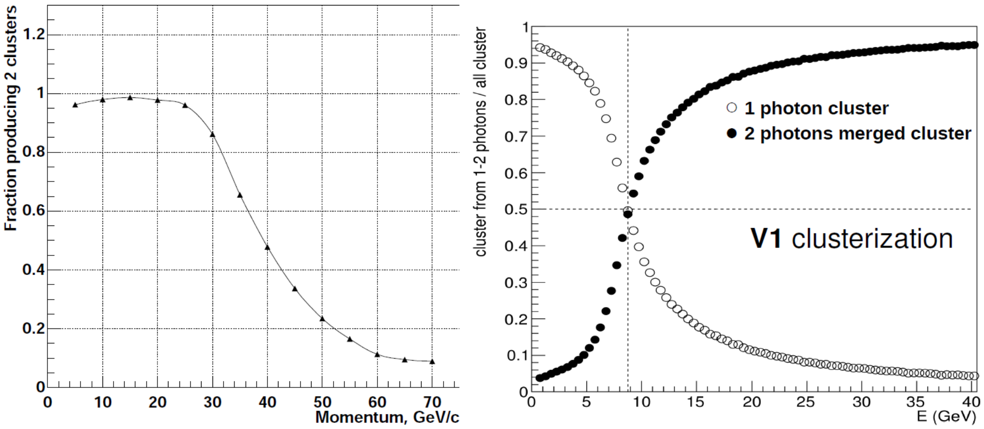

Figure 2.14: Two π^0 decay photon separation. Left for PHOS, right for EMCal [129].

2.2.4 Forward detectors

The V0 detector consists of 2 arrays of scintillators. Each interaction point side (A/C) of the array is located at different distance from the interaction point (same for T0 and FMD), due to presence of the muon arm on C side (Fig. 2.15). On top of the basic L0 interaction trigger and centrality triggers, the V0 also provides background rejection for the muon arm and centrality signal to other detectors trigger systems (EMCal, DCal, PHOS).

The T0 detector in difference to V0 consists of 2 arrays of photo-multiplier tubes equipped with Cherenkov radiators. It is capable of locating the primary vertex with 1.5 cm precision. T0 can also act as redundancy for the V0.

The FMD is composed of silicon strip detectors and it's main target is to extend the ITS charged particle multiplicity measurements to pseudorapidity range $-3.4 < \eta < 5.0$. There are small overlaps of the regions of FMD and ITS plates.

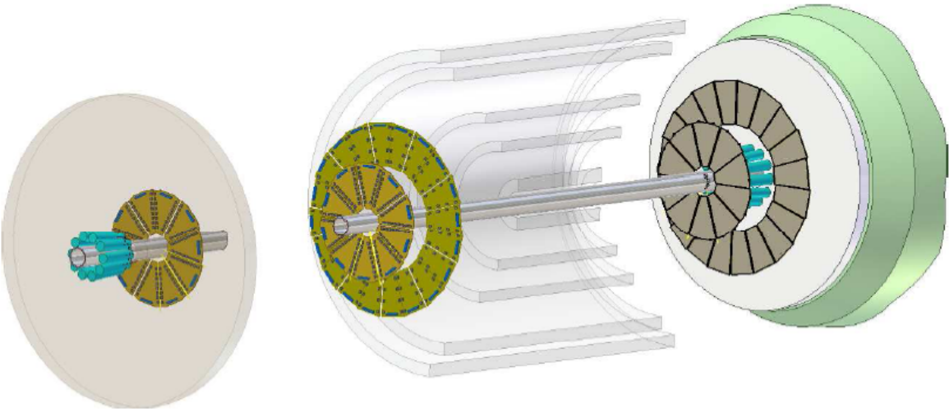

Figure 2.15: Placement of the T0 (blue), V0 (khaki) and FMD (brown) arrays in ALICE.

The ZDC is a set of calorimeters, located rather far (116 m) on both sides of the interaction point. Each set of calorimeters consists of one proton and one neutron calorimeter, located at zero degree angle to the beam (neutrons in between the two beam pipes, protons next to beam pipe to compensate for p trajectory shift by ALICE magnetic fields).

Additionally there are two electromagnetic calorimeters placed at 7 m from the interaction point. The main purpose of the ZDC is to detect spectator nucleons of the collisions. It can provide luminosity, centrality and reaction plane measurements.

2.2.5 Forward muon spectrometer

The forward muon spectrometer covers pseudorapidity one forward range of $-4.0 < \eta < -2.5$. It composes of high granularity (100 μm spacial resolution) tracking cathode pad chambers stacked in 10 levels (5 stations). There is a forward absorber made of carbon and concrete to absorb other particles coming from the collision in front of the tracking chambers. Additionally to protect from high rapidity particle background, there is beam shield of tungsten, lead a steel. Muon filter wall is located behind the tracking plates and separates the later 4 levels (2 stations) of muon trigger made of resistive plate chambers. Dipole magnet of 0.2 Tesla is placed in between the tracking strips to bend the trajectory of the muons.

The physics program of the muon spectrometer concentrates on measurements of dimuon decay channels of the heavy quarkonia and heavy flavor measurements through the open charm and beauty.

2.2.6 ALICE upgrades

There are several upgrades targeting improvement of the ALICE performance after the second LHC long technical shutdown, recently planned for the year 2018. The upgrade plan for the trigger strategy substantially concerns one part of this thesis, the development of EMCal trigger (chapter 4).

Primarily ALICE aims to increase the readout rate so that all MB Pb–Pb and pp collisions can be read out. The current event rate is limited to ≈ 500 Hz of MB Pb–Pb collisions and ≈ 1 kHz of pp. Targeted rates are 50 kHz for MB Pb–Pb and 2 MHz for MB pp collisions [136]. The data acquisition and trigger systems are being changed dramatically to achieve the planned speeds. Continuous readout is planned for the vast majority of detectors, which will read all interaction events. The trigger will be implemented at the software level, dropping collected events based on trigger detector data, before CPU demanding TPC clustering is performed.

The second target, closely related to the first one, is an upgrade of the silicon tracker (the ITS). Current readout speed of the ITS is limited. The contemporary six layers will be replaced by seven layers of pixel detectors, featuring also faster readout. The additional 7th layer will be the closest to the new thinner beam pipe. The whole material budget of the new ITS will be decreased from 1.14% X/X_0 per layer to 0.3% X/X_0 per layer. Additionally the new ITS will be capable of distinguishing secondary vertexes of charmed baryons and beauty mesons decays, with it's increased resolution of $\approx 20\ \mu$m.

The third upgrade target is aiming for installation of a forward silicon tracker, to aid the forward muon spectrometer with tracking of vertexes.

2.3 Electromagnetic Calorimeter

The EMCal was conceived as an addendum to the ALICE technical design [129], as a response to the results of the RHIC experiments in the high-p_{T} region. It is based on shashlik tower design in combination with organic scintillator, wave length shifting light guides, Avalanche Photo Diod (APD) readout and electronics copied from the ALICE TPC. As an addition to the ALICE, the EMCal suffers from the acceptance limitation (Fig. 2.16). The same radial distance from beam pipe is shared by EMCal, PHOS and HMPID, each covering a subset of the full acceptance. EMCal covers 110 degrees in azimuth and 1.4 units in pseudorapidity ($|\eta| < 0.7$). An extension of EMCal is being installed currently (DCal), which will provide a limited ability to measure back to back processes.

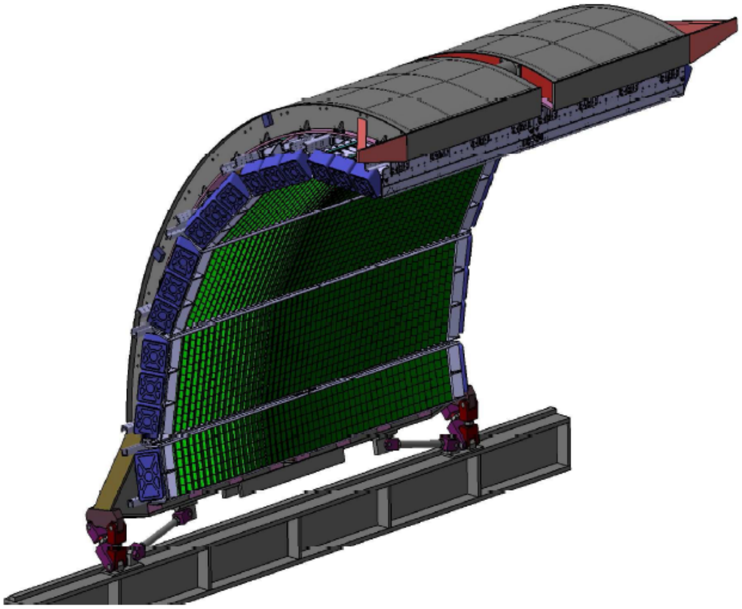

Figure 2.16: The EMCal detector arc.

EMCal is a sampling and relatively high granularity calorimeter. TDCs are not installed, so the timing resolution is poor, due to the limited precision of fitting of the digitized signal to recover the amplitude time. Performance of the EMCal will be discussed in more detail in the following chapter 3.

Apart of the event data, EMCal provides two levels of trigger signal, level-0 and level-1, which allows to trigger on single shower deposits or integrated energy deposit in a larger area (jets).

2.3.1 EMCal module

EMCal module contains $2\times2 = 4$ towers built up from 76 alternating layers of 1.44 mm Pb and 77 layers of 1.76 mm polystyrene base, injection moulded scintillator (BASF143E + 1.5% pTP + 0.04% POPOP) with an intrinsic light output of 50% Anthracene [129]. The tower average Moliere radius is 3.20 cm.

Each tower (Fig. 2.17) scintillators are equipped with reflectors on all sides to provide better gain and keep the four towers inside one module isolated to $> 99\%$. The module is encapsulated in 150 μm stainless case, covering the four transverse faces.

The towers are built with increasing diameter to allow for approximate projectivity to the interaction vertex in both η and φ. The face plate (towards interaction) is $\approx 6\times6$ cm^2 with acceptance of $\Delta\eta \times \Delta\varphi \approx 0.014 \times 0.014$.

The scintillation photons produced in the active volume of the tower are collected by 36 longitudinally placed wave length shifting light guide fibers. Each fiber is terminated

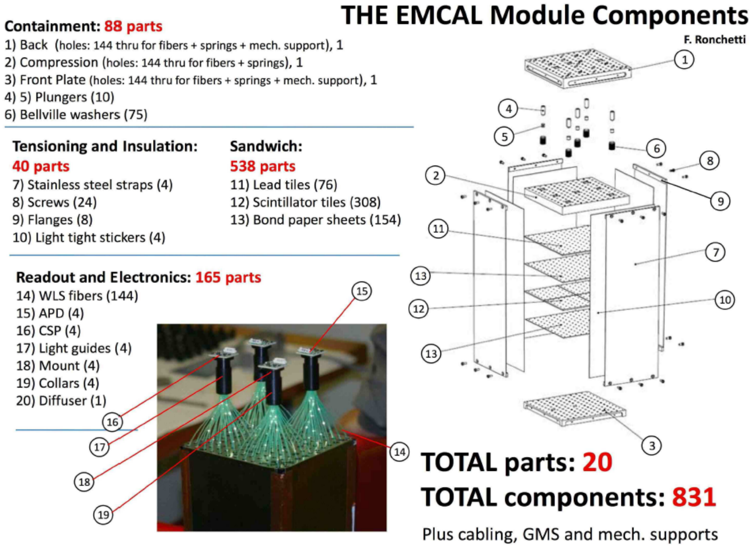

Figure 2.17: The exploded EMCal tower view.

with aluminum mirror to prevent gain losses on the face plate side. The opposite sides of the light guides are collected to a 6.8 mm diameter circular shape. A small diffusive light guide is used to connect the circle of fibers to the 5×5 mm active area of the APD. The APD shares a common small Printed Circuit Board (PCB) with a charge sensitive preamplifier. Signal from the preamplifier is driven by cables to the Front-End Electronics (FEE), which is located at the high rapidity edge of each EMCal super module.

Signal gain of each tower can be monitored on-line via LED subsystem, which transports short LED light flashes to the towers and a reference signal to the FEE. The LED system is observing the general functionality of the EMCal detection and readout chain. It is also meant to provide baseline for temperature dependent calibration. Gain of the APDs is dependent on the temperature (Fig. 2.18).

2.3.2 Signal collection

The APDs are operated with gain factor around 50. Fine tuning is available through dynamic adjustment of the bias voltage, available for each channel separately, with min and max at 250 and 400 V respectively in 0.2 V steps. The yield of the APD is measured to be 4.4 photo-electrons/MeV. The dynamic range of the system is 250 GeV, with 245 MeV per ADC count of a 10 bit ADC. For better precision of low energetic hits, each channel has a parallel ADC with ×16 gain factor (16 GeV range and 15 MeV/ADC count). Electronic noise coming from the APD and preamplifier is expected to be around 12 MeV/tower, which is smaller than the intrinsic energy resolution.

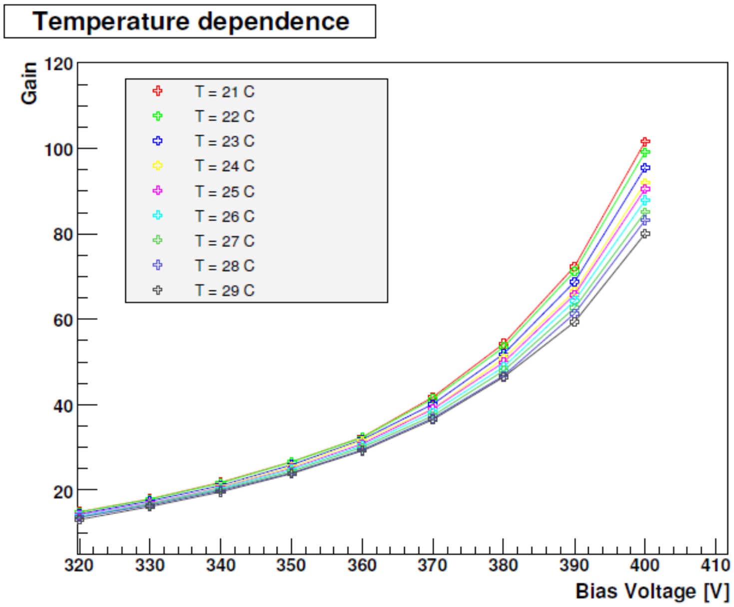

Figure 2.18: Avalanche photo diode gain dependency on the temperature and voltage.

2.3.3 Energy resolution

One module thickness is ≈ 20 radiation lengths and the final Pb to scintillator ratio is $1:1.22$. Energy leakage is below 3% for 100 GeV photons. The energy resolution is shown on Fig. 2.19. The energy resolution can be described by Eq. (2.1).

$$\frac{\sigma}{E} = \sqrt{A^2 + \frac{B^2}{E} + \frac{C^2}{E^2}} \tag{2.1}$$

The constant term A arises from systematic effects, such as shower leakage, detector non-uniformity or channel-by-channel calibration errors. The second term B represents stochastic fluctuations due to intrinsic detector effects such as energy deposit, energy sampling, light collection efficiency, etc. The third term C contains contribution from electronic noise summed over the towers and ADC sampling precision. The A and B terms put together what is called intrinsic energy resolution of the detector (in the testbeam case $11.3\%/\sqrt{E} + 1.7\%$). Decomposed contribution as comes from simulation of the intrinsic resolution and sampling and electronic noise are shown on Fig. 2.19.

Uniformity of the energy resolution as a function of different hit position in a module of towers was studied as well in testbeam. Beam was directed into tower centers, module centers, borders of two towers or borders of modules. No significant dependency was observed (Fig. 2.20).

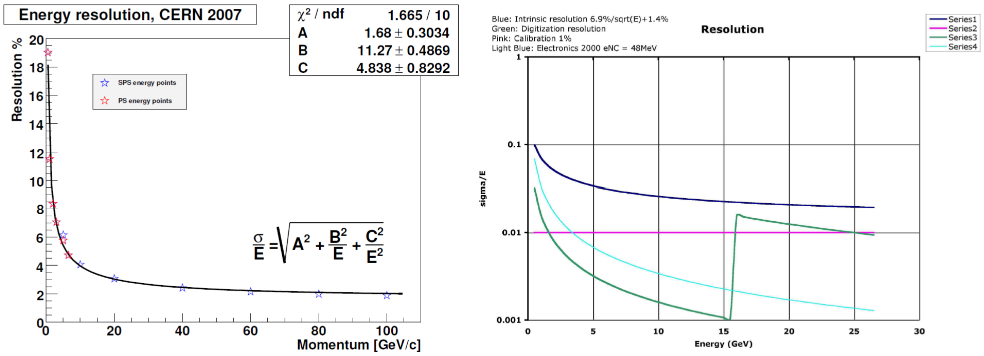

Figure 2.19: Left: Energy resolution of EMCal in testbeam. Right: contributions to the energy resolution; dark-blue - intrinsic resolution; green - ADC sampling; light-blue - electronics noise [129].

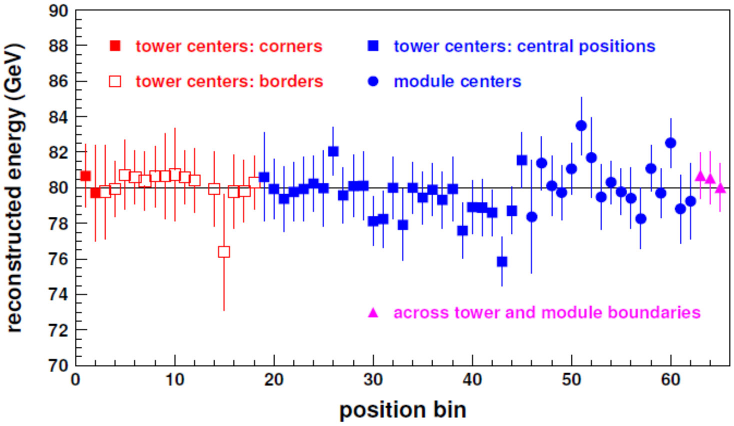

Figure 2.20: Energy resolution as a function of hit position in the module (or on module borders) in testbeam [129].

2.3.4 Position resolution

The coordinate location in calorimeter is obtained by weighting the energy deposits in towers representing one cluster. Thus one can achieve better position resolution than is the granularity.

The weighting in EMCal is logarithmic, Eq. (2.2) defines weight of a tower used in position reconstruction based on energy of the cluster E_{clus}. The constant factor 4.5 defines cutoff below which the cells are not considered.

$$\mathrm{weight} = \mathrm{Max}\left[0,\ 4.5 + \ln\left(\frac{E_{\mathrm{tower}}}{E_{\mathrm{clus}}}\right)\right] \tag{2.2}$$

Fig. 2.21 shows the position resolution as a function of beam energy and position of the beam hit in testbeam. The position resolution shows no dependency on the position of the incident beam. The dependency on the beam energy can be described as $1.5 + 5.3/\sqrt{E_{\text{clus}}}$ [mm].

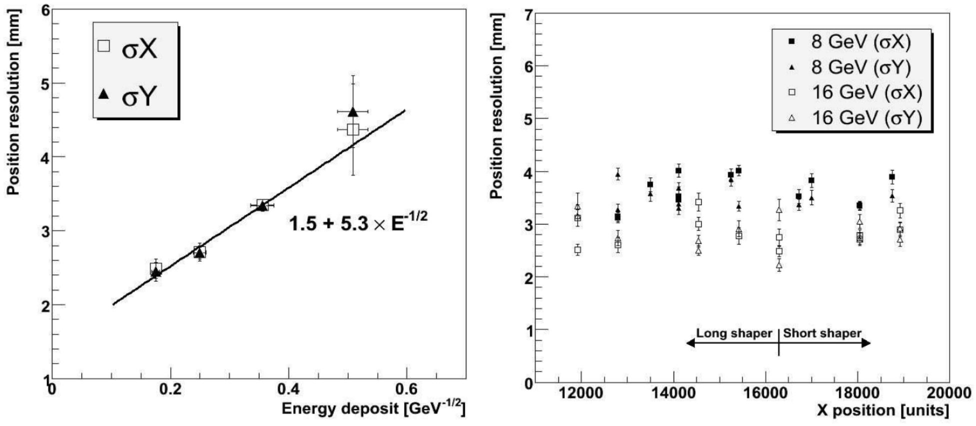

Figure 2.21: Left: Position resolution as a function of beam energy. Right: Position resolution as a function of incident beam position. Both for electron beams [129].

2.3.5 Digitization

Analog signal arrives from the APD and preamplifier to the FEE cards located in the FEE crate. The signal is processed by a shaper and delivered to the ALTRO chip [137] for digitization and digital processing.

The shapers are designed in such way that for the 4.4 photo-electrons/MeV and APD gain factor of 50, the range fills full input range of 1 V of the ALTRO chip, for each of the high (×16) and low gain channels. Signal shape with 100 ns shaping time is shown on the Fig. 2.22 and characterized by the Eq. (2.3)

$$V(t) = \left(\frac{4Q \cdot A^2}{C_f}\right) \cdot \left(\frac{t - t_0}{\tau}\right)^2 \cdot e^{-2\frac{t-t_0}{\tau}} \tag{2.3}$$

where Q is charge on APD, A the preamplifier gain, C_f capacitance in the preamplifier, τ the shaping time.

Digitization is performed by the ALTRO chip in two parallel streams corresponding to low and high gain channels. The ALTRO chip was developed for the ALICE TPC and was adopted by the electromagnetic calorimeters. The ADC range is 10 bits in each case, the sampling frequency is 100 ns (10 MHz), which brings consideration in correct time definition of the signal, as there are 4 possible phases of sampling in respect to trigger signal of 40 MHz granularity.

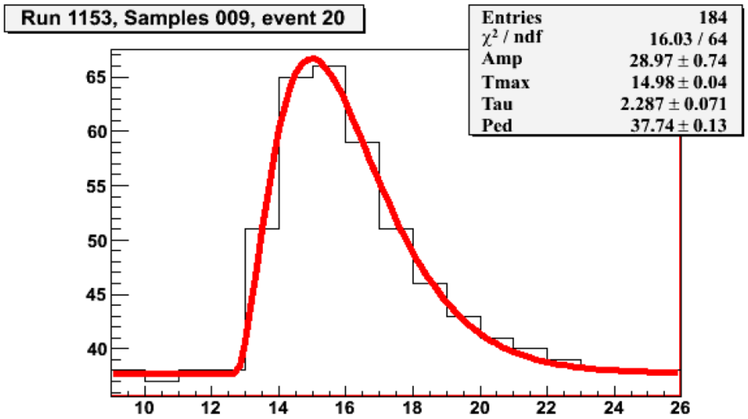

Figure 2.22: Digitized signal shape fitted by the Eq. (2.3) [129].

The ALTRO chip performs pedestal subtraction based on programmed pedestal memory. The pedestals are obtained from special runs with no preprogrammed pedestal or signal present.

After the pedestal subtraction, the ALTRO chip can perform zero suppression by removing samples with ADC counts below threshold from the data stream, reducing thus substantially the data volume provided to readout. Each sequence of consecutive samples above the threshold is enveloped by time and length word, thus the zero suppression threshold should be well above the noise level (order of 1 ADC). Zero suppression mechanism is diagrammatically described on Fig. 2.23. The zero suppression features more complex algorithm of glitch filtering, pre- and post- samples and close cluster merging, which is out of scope of this thesis and can be studied in the ALTRO manual [138].

2.3.6 Read out

The ALTRO chip copies a defined amount of samples from a rotating buffer (conserves samples consecutively, rewriting the oldest) to a Multi-Event Buffer (MEB) on reception of the level-0 trigger from the ALICE Central Trigger Processor (CTP). Reception of the level-1 signal validates the data in the multi event buffer, so it can not be rewritten by the following level-0. Read out of the multi-event buffer can be performed after each level-1 (no MEB operation) or after up to 4 triggers. Fig. 2.24 depicts the MEB operation.

Each FEE card is housing 4 ALTRO chips, each of 16 channels. One half of the channels is dedicated to low gain channels the other half to the high gain. In the basic form of the readout, all channels are being read out in series, each channel supplying all samples above the zero suppression threshold. The ALTROs are configured to record

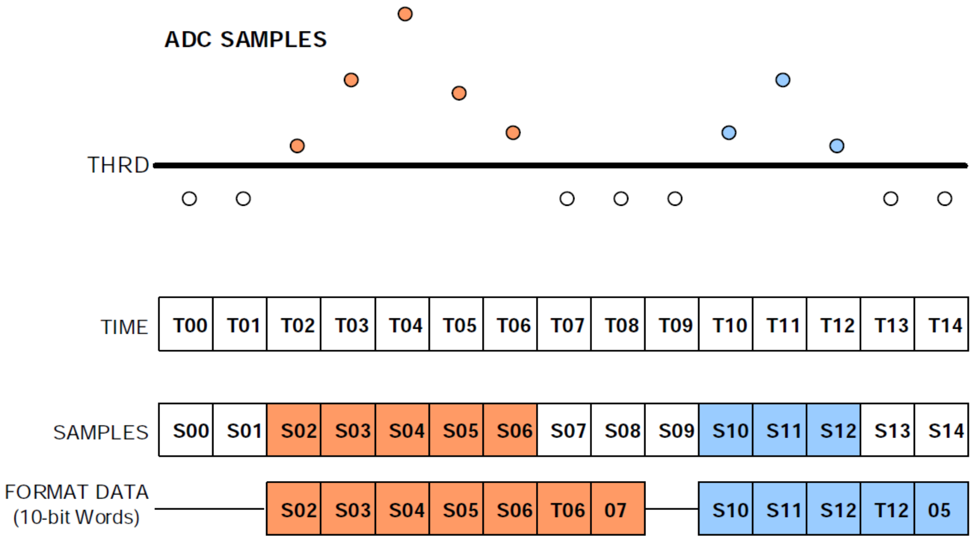

Figure 2.23: ALTRO zero suppression. The target is to conserve bandwidth and not to send ADC samples (S0-S14) which contain no signal. Thresholds is set above noise level to identify samples with no signal. Continuous bunches of samples with signal are appended by header (position in time T0-T14 and bunch length).

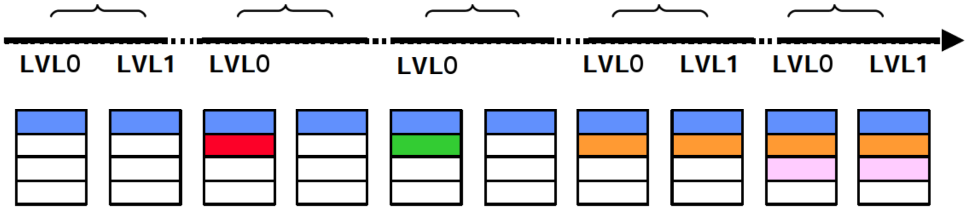

Figure 2.24: Multi-event buffer operation of ALTRO. The boxes are event records in the MEB, different events are color coded. Braces connect level-0 and consecutive (or missing) level-1 trigger. The figure shows consecutive filling and validation or discarding of an event based on arriving or missing level-1 trigger.

15 samples per event. There are up to 10 FEE cards attached to one readout bus, resulting in up to 640 channels read out in series.

The read out is controlled by the Read-out Control Unit (RCU) [139]. The RCU condenses data from 2 readout buses and forwards them to the DAQ Local Data Condenser (LDC) PC via the standardized ALICE Detector Data Link (DDL) optical link [140]. The RCU can perform a sparse data readout, each FEE card is first asked to provide a map of channels which have any samples that passed the zero suppression. Only the channels containing any data are read out. The sparse readout saves the communication setup times for each channel thus reducing the read out time of an empty detector.

Upgrade of the EMCal readout systems in being developed [141] to change the readout from serial to parallel (per FEE card). The Scalable Readout Unit (SRU) will service a whole super module and combine DAQ and DCS. The target speed of the new readout system is to comply with the ALICE operation after the second LHC long shutdown (50 kHz MB Pb–Pb).

2.3.7 Trigger

EMCal provides two lowest levels (level-0 and level-1) of the trigger decision in its acceptance. The trigger subsystem resides in specific hardware boards and is programmed on the level of Field Programmable Gateway Array chip (FPGA) code. FPGAs are integrated circuits that can be programmed and re-programmed after their production. They provide a compromise in speed and variability in between fixed application specific integrated circuits and processors.

The electronic signal from towers reaches FEE, where a stream to trigger separates from stream to the ALTRO chips. On the FEE level, exclusive sets of 2×2 towers are summed in analog way to limit number of channels that the trigger processes. The trigger does not require very good position resolution.

Analog sums (fast-OR) of the four towers are then forwarded to the Trigger Region Units (TRU) [142] for digitization and processing. The TRUs have been designed at CERN and produced by University of Jyväskylä. Their programming and operation are in hands of the author of this thesis. Result of the processing in TRU (described in detail in the chapter 4) is a single bit decision per TRU. The TRUs forward decision to Summary Trigger Unit (STU) [143] for production of a single bit OR result which is then forwarded to the ALICE CTP.

The level-0 trigger checks for energy deposits within a window of 2×2 trigger channels (4×4 towers). The 2×2 window is sliding to cover all possible combinations of channels withing the level-0 unit acceptance.

The single level-1 trigger unit receives all digital amplitude data from all the TRUs and recomputes the similar 2×2 channel decision as level-0, with advantage of producing the 2×2 channel windows on the boarders of the level-0 unit acceptance. In addition the STU can check for energy deposits inside 16×16 trigger channel window (32×32 towers). This large window trigger is considered to be jet trigger.

The trigger subsystem is capable of providing it's primitive data to DAQ. An additional link of the EMCal level-0 trigger to this thesis is a fact that both presented analysis (chapters 5 and 6) have been conducted with data collected by the EMCal trigger. The triggered data sample contribution is crucial especially for the analysis of jets in p–A collisions.

2.3.8 Control system

The control system of the level-0 trigger shares the lowest hardware level with the rest of EMCal electronics. The higher levels of the trigger control system have been as well developed by the author of this thesis, but are outside of its scope.

Chapter 3

Electromagnetic Calorimeter Performance

Detail understanding of the EMCal performance is necessary for both data analysis presented in this thesis (chapters 5 and 6). It is as well important to understand the behavior of the detector in the parts that concern performance of the trigger, so that the trigger can be operated efficiently. Especially the online calibration, noisy towers and signal timing in electronics affect the trigger performance.

This chapter presents an analysis of EMCal performance up to the level of reconstructed cluster spectra. The detector arrangement, calibration and data reconstruction is discussed first.

3.1 EMCal supermodule

EMCal is segmented in various ways into functional units. The various segmentation is using different patterns, which may introduce unexpected effects.

3.1.1 Geometry and power

The largest mechanical unit is a super module (SM), 48 towers in η, 24 towers in φ (Fig. 3.1). The SM is divided into 24 strips, each covering full φ and 2 towers in η. A strip is composed of 2×2 tower modules. There are 5 full size SMs on each A and C side[1] of the detector (labeled SMA0, SMC0, SMA1, etc.). There are also two 1/3 SMs SMA5 and SMC5.

EMCal is powered by low voltage to supply electronics and high voltage to provide enough bias for the avalanche photo diodes (APDs). Low voltage (LV) is always common to 3 SMs. One set of LV lines supplies SMA0, SMA1, SMA2; other set of LV

---

[1] ALICE is separated logically along z axis into halves (A and C), C side is the one with muon arm

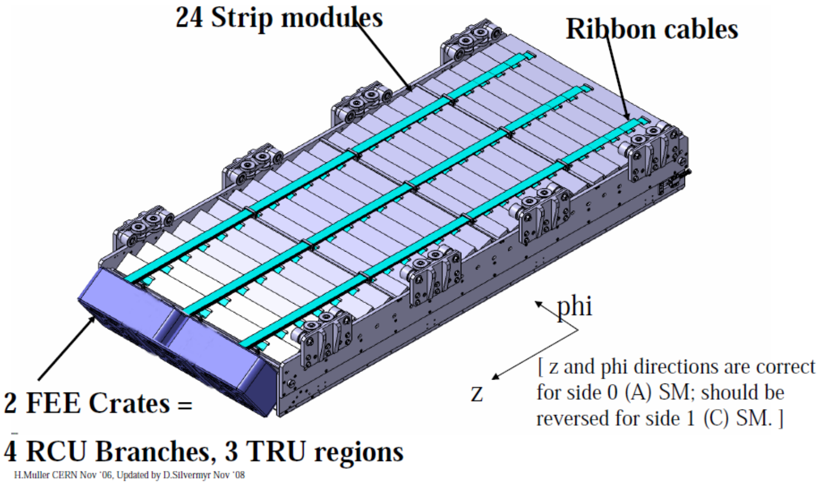

Figure 3.1: One EMCal supermodule.

lines supplies SMA3, SMA4, SMA5. Similarly on the C side. The high voltage (HV) of each SM is supplied by 4 HV channels. Each channel supplies one RCU branch (details are discussed below in the readout subsection). The HV is supplied through FEE cards, which can adjust the voltage with minimum at 250 V. There is an additional HV channel per SM that supplies on-line LED calibration system.

3.1.2 Readout

Each SM is equipped with readout electronics located in two crates. Each crate contains one readout control unit (RCU) with two branches. There are 9 front end cards (FEEs) on a branch, each card reads out a 4×8 area of towers (Fig. 3.2). There are 2 RCUs per SM. The RCU is a standalone readout segment, which operates independently on the other RCU in the same SM.

3.1.3 Trigger and LED calibration

Trigger does not share the same segmentation as readout. Instead, the SM is divided into three regions in φ each served by a trigger region unit (TRU). All TRUs that produce L0 decision supply information to a summary trigger unit (STU) for L1 processing.

Online calibration system uses LED flashes to supply artificial signal for continuous energy calibration. Single LED serves one strip, one LED driver serves one SM. LED driver is composes of three LED plates, SM is divided into three regions according to the plates, this time in η.

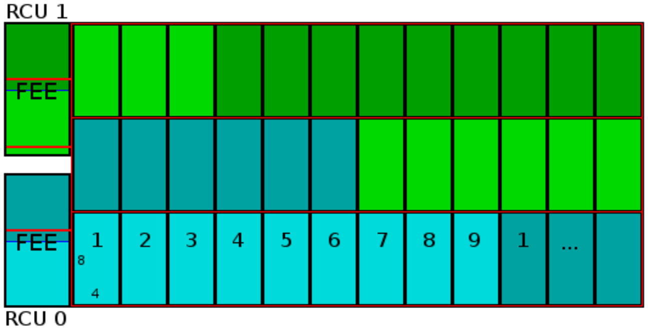

Figure 3.2: One EMCal super module with segmentation of readout in green and blue and trigger in red. Shades of green or blue separate different RCU branches.

3.1.4 Possible errors arising from geometry

The simplest failure, except of a failure of a single tower, is failure of one FEE card, affecting 32 towers. Exclusion from readout, high noise, intermittent readout failure and other adorable effects can occur. It is possible that one failing FEE card can either block or induce false data in other FEE cards on the branch. It has been observed that a FEE card can first fail on one half of its channels, grouped in η.

LED driver failure can result in fake high amplitude signals showing in any combination of the three in-SM regions in η which the driver serves. The most common observation of the LED structuring is a lower or higher intensity of flashes in one strip, which may come from either malfunctioning LED or from a problem with light guides. Another frequently observed problem was false triggering inside the LED system caused either by the led driver itself or malfunction LED Control Unit (LCU). The problem results in presence of fake signals in physics data taking.

The cables that conduct signals from APDs towards the FEE are not made of the same length. Hence the signal travel time from midrapidity regions is significantly longer than the travel time of signal from high rapidity towers. The largest in-SM difference is in order of 30 ns.

In case of RCU 1 exclusion from the readout, the remaining middle part of the SM which still has a functional readout (RCU 0) is left without a trigger. The TRU that serves the middle region is placed in RCU 1 FEE crate. This gives a rise to situation when there are only minimum bias hits available in the affected region.

3.2 Reconstruction and calibration

3.2.1 Online calibration

The only available online calibration concerns bias voltage available to the APDs. It is preferred to adjust APD biases such, that the towers have identical of very close gains. The desired online calibration precision lies around 1%, as effects on the jet trigger can be significant (as shown on Fig. 3.3). This allows to increase the precision of the trigger system which operates online. It must be however taken into account that decreasing the bias voltage deteorates the energy resolution. Hence it is not possible to equalize all the tower gains. The primary online calibration was obtained by analyzing MIP signals from cosmic radiation. Re-calibration was done later by using offline calibration constants that were obtained from analysis of π^0 (discussed in more detail in 3.2.3).

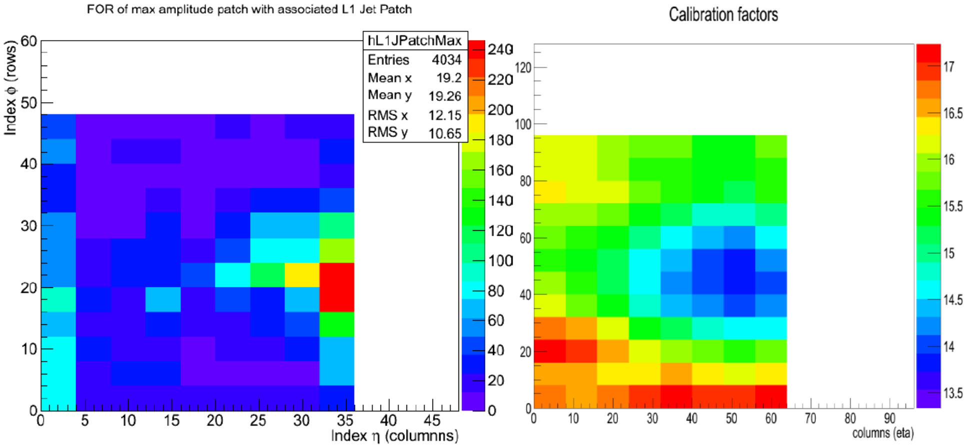

Figure 3.3: Jet trigger quality monitor showing localized jet trigger rate (left) and a corresponding offline calibration constants (right). Higher online gain on one EMCal SM (hence lower offline calibration constants) caused high rate localized jet trigger rate in the region.

3.2.2 Signal fitting

The signal from the detector comes out digitized in 100 ns frames and ordered into events. Each tower channel is already pedestal subtracted and zero suppressed (which is done on the FEE level). There is a pedestal measurement following end of each fill, when the pedestals are evaluated and recorded into the FEE memory, so those can be used for the following fill.

The ADC digitized value is always an underestimate of the input signal, because the last ADC bit is generated by a simple comparator. A simple toy MC study was performed to understand how much the ADC digitized amplitude differs from the input signal, result is shown on Fig. 3.4.

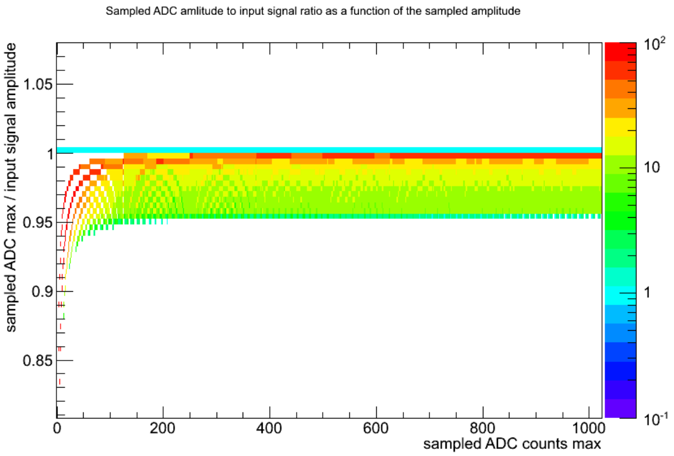

Figure 3.4: Dependence of sampled ADC value on the input signal amplitude. The ADC sampled value is always lower in respect to the input signal. The difference depends on the sampling phase. To evaluate the fraction of the signal which the ADC sample misses, all possible flat distributed sampling phases were simulated. Ratio in between the sampled value and input signal amplitude was plotted as a function of the sampled signal amplitude.

The digitized signal is fitted offline by a Γ_2 function, Eq. (3.1), to acquire the shape of the input signal, to obtain better energy and time resolution. The energy is equivalent to the signal amplitude (A), time to the amplitude position (t_{Max}).

$$f(t) = P + A \cdot x^{\gamma} \cdot e^{\gamma(1-x)} \; ; \quad x = (t - t_{\mathrm{Max}} + \tau)/\tau \tag{3.1}$$

with the P, τ and γ parameters fixed to 0, 2.35 and 2 respectively. The values of A and t_{Max} are obtained from the fit.

The performance of the fitting was checked by relating the fitted amplitude and raw ADC amplitude for physics and calibration LED signals (Fig. 3.5).

3.2.3 Energy calibration

The first energy calibration was obtained before installing the SMs inside ALICE. The method used aligning of a MIP signals induced by cosmic radiation in all towers to a similar level.

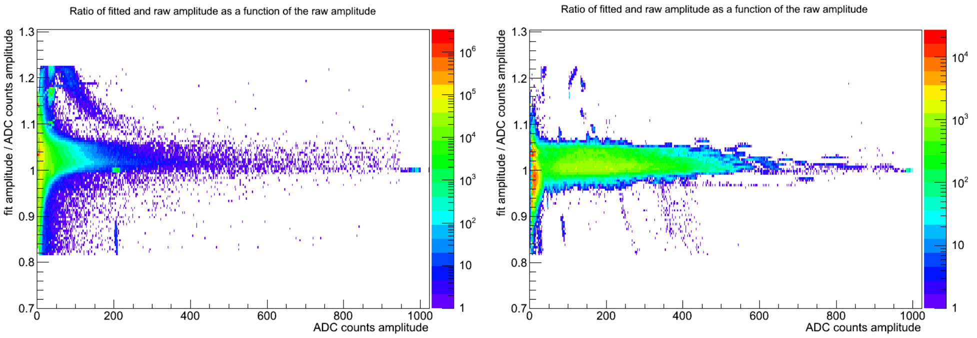

Figure 3.5: Dependence of fitted function amplitude on the sampled ADC amplitude. For physics signals on the left and calibration LED signals on the right.

With introduction of EMCal trigger (which can not trigger on MIP due to FEE signal noise above MIP level), calibration on neutral pion decays became possible (Fig. 3.6). The method uses reconstruction of invariant mass of cluster pairs, masses are reconstructed for each tower. The reconstructed mass deviation to Particle Data Group (PDG) mass, 134.97 MeV/c^2, and its sigma are minimized in several recalibration iterations.

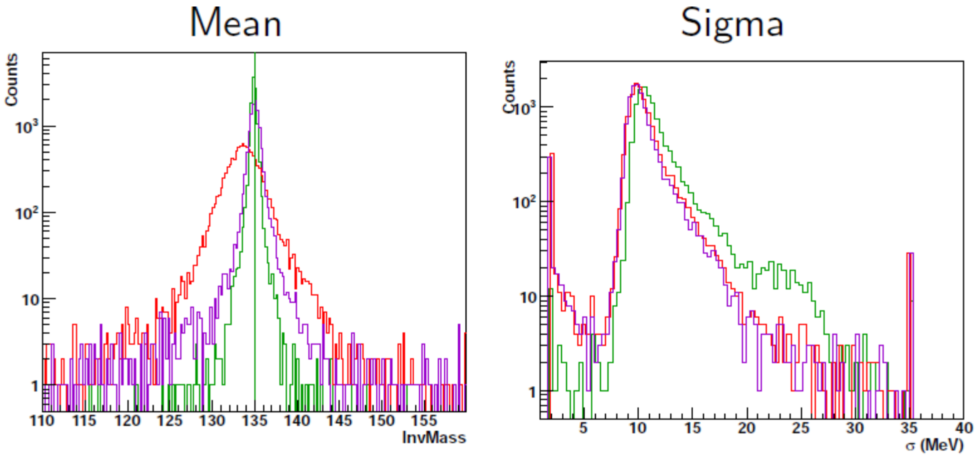

Figure 3.6: π^0 calibration. Shows several data reconstruction passes; red - year 2012 data pass 0, violet - year data 2012 pass 2, green - year 2011 data pass 2. There is possibility to use different calibration in between the reconstruction passes. It is usual that calibration is obtained with the first pass and then improved for the later passes (compare the two passes in 2012 data). Also it is not granted that calibration remains identical in between years, for example due to additions of detectors inside ALICE (compare 2011 to 2012).

3.2.4 Run dependent correction

The light yield of the towers and the gain of APDs are temperature dependent. The detector is not operated in constant temperatures. The major variations in temperature come from air conditioning and ventilation changes, other detector operation and seasonal shifts. Run by run correction factors based on temperature measurement are implemented. Fig. 3.7 shows effect of the run dependent temperature corrections.

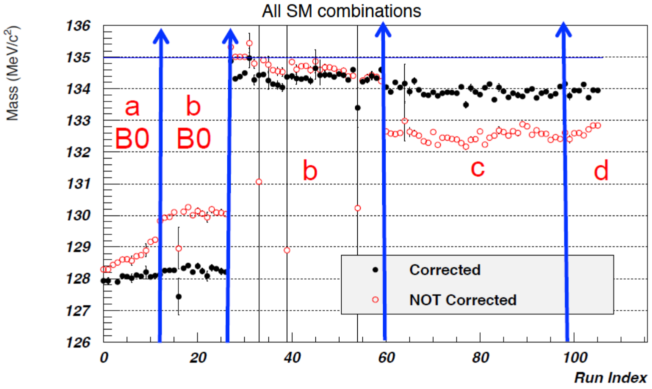

Figure 3.7: Influence of run dependent corrections (based on temperature) on π^0 reconstructed mass in EMCal. The plot shows points before and after corrections. The borders of data taking periods and periods with magnetic field OFF (B0) are displayed.

3.2.5 Noisy tower masks

Some towers may produce unphysical signals or be dead, due to failing electronics. Mask of noisy towers is used to remove signals from failing towers before the clustering.

Spectra of each tower is analyzed and towers with excessive hit counts or deviation from healthy spectrum shape are identified. In course of work on the π^0 analysis, an improvement to existing masking technique was developed. Some towers noisy in higher E_{tower} regions were not identified, because hit count integral over the whole energy range (of steeply falling spectrum) was used as a measure of amount of noise. This was simply overcome by analyzing hit counts in multiple energy bins.

3.2.6 Timing calibration

A check of EMCal timing calibration was performed. This check revealed several problems that were not discovered until then.

The timing calibration is supposed to compensate for any effects that shift the signal position in time (geometry for example). For trigger operation, it is extremely important to know precisely the timing of signals in the detector. Because of geometry effects discussed at 3.1.4, the signal travels different distances in between tower and electronics. The deviation is up to 30 ns inside a single SM. Production of trigger inside one bunch crossing (25 ns) is then very difficult. The timing analysis also provided additional bases for establishing minimal E_{clus} cuts in analysis.

The timing calibration can be obtained using a well defined signal with known timing, which is recorded and calibration is extracted relative to the known timing of the signal. High energy photon hits can be considered a good time signal. The high energy photon hits are obtained from EMCal data sample applying a minimal energy threshold. To obtain a clean sample coming from a single event, pileup events and hits with a matched tracks are removed. Exotic clusters (3.3.2) are removed as well. EMCal electronics (same as TPC) operates with 100 ns sampling clock, there are four possible phases in which an event can be sampled (LHC clock cycle is 25 ns). This difference in sampling introduces shifts. There is a separate calibration for each bunch crossing number modulo 4 (4 sets in total).

The original EMCal timing calibration was obtained by averaging all hit times in a tower, which fit a specified time window. There are various defects which can move a simple average significantly away from a true position. A method using Gaussian fitting of the timing distribution was developed. The timing calibration results were obtained using a 0.5 GeV minimal energy cut on single towers, which is considerably higher than any usual noise.

Fig. 3.8 shows EMCal tower signal times separately for all bunch crossings before and after timing calibration. There are very precisely timed signals in the uncalibrated distribution, which get smudged by the calibration. This points to existence of high magnitude electronics noise. The noise has periodicity of 100 ns and 4 different phases based on the bunch crossing modulo 4. An example of a signal time distribution inside a single tower is shown on Fig. 3.9.

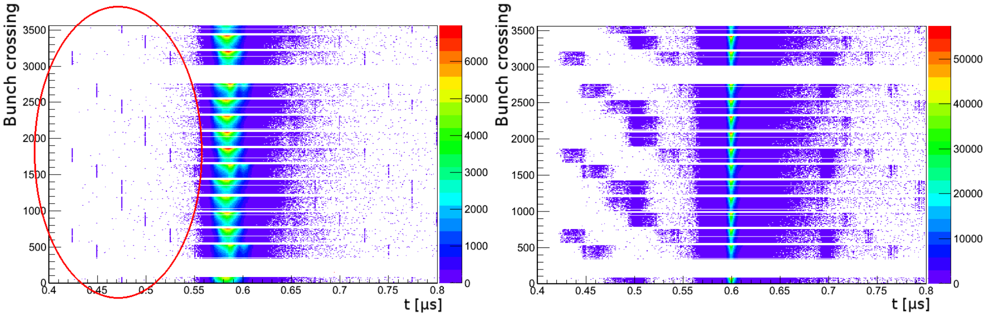

Figure 3.8: Left: EMCal tower signal times for each bunch crossing, before timing calibration. Right: after timing calibration. The red ellipse highlights a part of 100 ns periodic noise. With 0.5 GeV minimal energy cut.

Another observed defect was a systematic shift of timing for all towers in one RCU

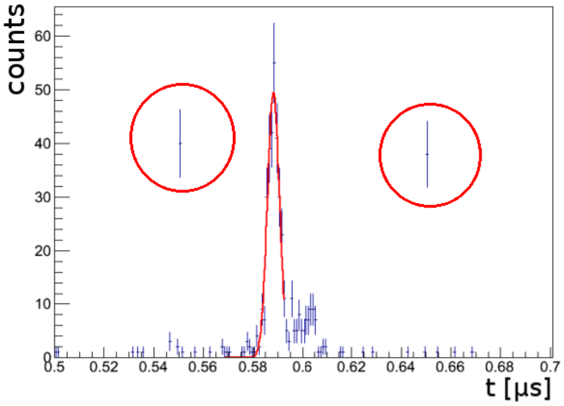

Figure 3.9: An example of one EMCal tower signal time distribution before timing calibration. The red circles highlight the 100 ns periodic noise. With 0.5 GeV minimal E_{tower}.

region. The problem was understood and traced to a reboot of the corresponding Detector Control System (DCS) board, which provides clock signal to the RCU. The DCS board reboot erased configuration of TTCrx chip present on the board, which is responsible for reception of the clock signal from the CTP. The clock phase configuration was zeroed. A process for shifters was proposed and adopted to mitigate the possible shifts.

Strange structures in the timing calibration arising probably from usage of a different APDs (Fig. 3.10) in a single super module were observed. This was later confirmed by recovering information about the super module assembly process.

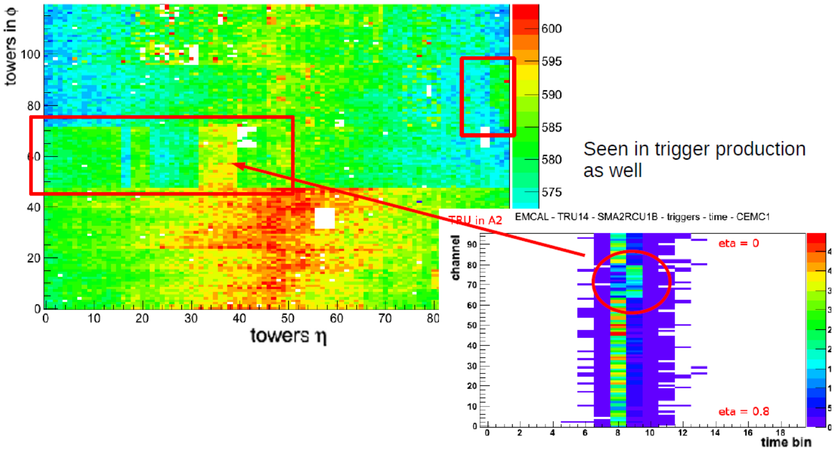

Figure 3.10: Timing calibration coefficients. With sharp structures highlighted. The same timing shift is observed in trigger timing in the given region.

Appearance of a second timing peak in towers (Fig. 3.11) was another irregularity encountered. This result concerns signals which pass the clustering threshold of 50 MeV and thus may alter the output of the clustering algorithm. The second peak appearance is probably result of a noise in the FEE at the moment of ADC sampling. This peak shifts with tower position in η and appears in two BC modulo bins only (Fig. 3.12). A sampling noise is the most likely explanation (yet not confirmed up to writing of this thesis).

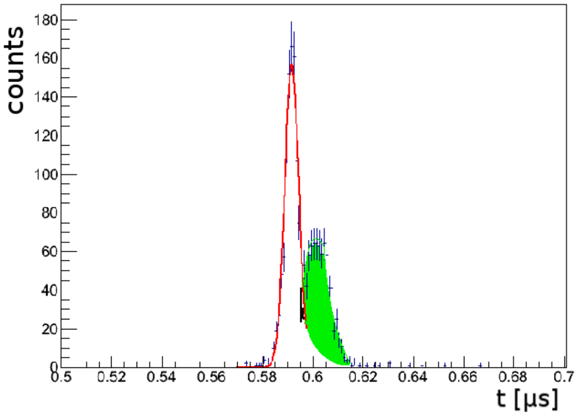

Figure 3.11: An example of a tower with second timing peak. Red is gaussian fit of the first peak, green a highlighted area outside the gaussian fit.

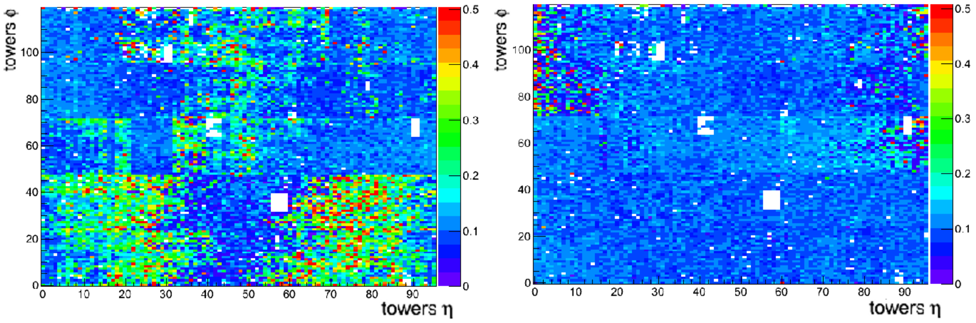

Figure 3.12: Evaluation of an amount of hits that do fall outside the gaussian fit into the second peak (green area in Fig. 3.11). Two BC modulo bins are shown. Left for BC modulo = 2, right 3. The z axis shows ratio of outliers to total. The outliers add up to 50% for some of the towers. The amount of outliers is also dependent on cable length in the SM and hence on the phase when the signal arrives to the sampling edge of FEE.

Influence of the effect on clustering is shown on Fig. 3.13. There is an evidence for existence of an excessive noise of magnitude around 200 MeV. Depending on the settings of the clustering algorithm, this noise produces cell signal that couples to existing clusters or if the noise signal is strong enough to cross the cluster seed energy, it creates low E clusters made purely out of noise. The rate of this fake hits is below 1% for cluster with $E_{\text{clus}} > 0.5$ GeV. There is a bigger effect on cluster of $E_{\text{clus}} < 0.3$ GeV. Realizing this led to application of 300 MeV E_{clus} cut in the jet analysis.

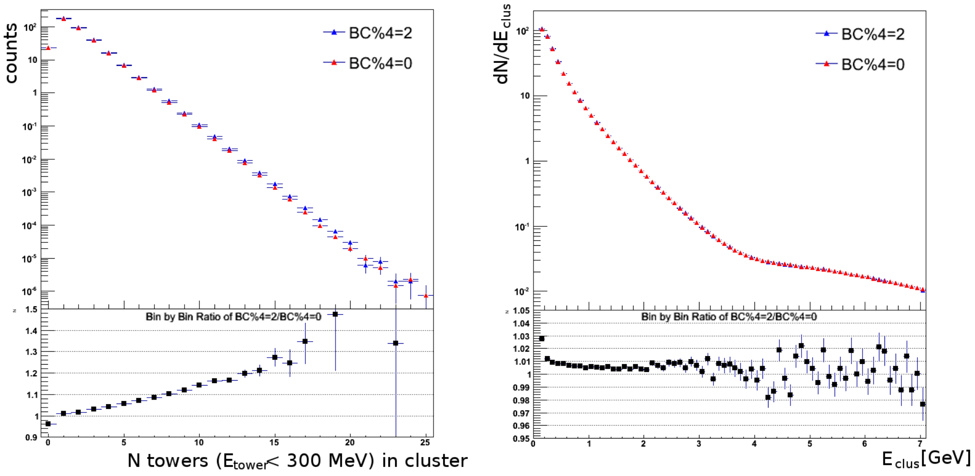

Figure 3.13: Comparison of cluster properties for two different bunch crossing modulo 4. The fraction of hits in the second peak for BC%4 = 0 is very similar to BC%4 = 3, shown on Fig. 3.12. Hence BC%4 = 0 is expected to be much less affected by noise than BC%4 = 2. On the left, distribution of amount of cells with $E_{\text{clus}} < 300$ MeV in cluster is shown. The right plot shows cluster energy spectra. There are 2 expected effects in the cluster spectra; a) there will be more low E_{clus} clusters due to clustering the noise b) the cluster spectra will be shifted higher as the clusters pick up the noise cells.

3.2.7 Nonlinearity correction

There are various sources of a non-linear response of the electronics to the energy deposited in the towers. Shower depth is dependent on logarithm of incident particle energy. The Cherenkov light produced by lower energy hits is attenuated more in the tower itself, before it reaches the readout. High energy hits may reach saturation limits of the electronics or the shower leakage due to small depth of the calorimeter becomes significant. Response function of the electronics might be non-linear and other possible sources contribute as well.

Nonlinearity of the electronics response to the deposited energy is important mainly in the low E_{clus} region (Fig. 3.14). Correction is obtained via analyzing test beam data from PS and SPS. Another possible method of studying the nonlinearity is to analyze symmetric neutral pion decays.

Both methods were used and their results agree. The nonlinearity calibration is applied on clusters, not on towers.

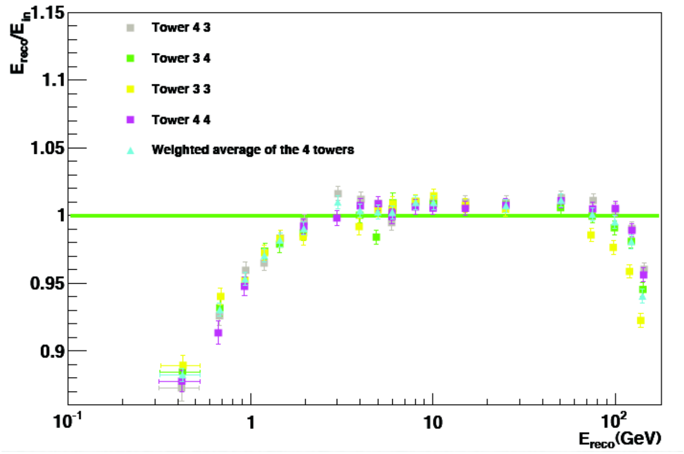

Figure 3.14: Response of EMCal to deposited energy as studied in PS and SPS test beam conditions. Shows four central towers of the test beam setup (to avoid transversal leakage). Ratio of reconstructed to incident energy.

3.3 Single clusters

3.3.1 Clustering

Three clustering algorithms are implemented for EMCal; v1, v2 and N×N. The v1 clusterizer searches for a tower with energy deposit greater than a defined seed energy and merges all surrounding (sharing a side) towers with energy deposit higher than a defined threshold. In the next step, all towers sharing a side with already included towers are added. The algorithm continues until it merges all geometrically fitting towers with energy above the threshold. The v2 algorithm is an improved version of v1. The algorithm can identify local minimum and halts the clustering in case that the neighboring tower energy is higher. Both algorithms remove already clustered towers from the pool, so one tower can not be used twice. The v2 separates roughly two close hits, unfolding must be used for the v1 algorithm to separate geometrically close clusters. The π^0 reconstruction efficiency (invariant mass method) drops significantly around $p_{\mathrm{T}} \simeq 6$ GeV with v1 and around $p_{\mathrm{T}} \simeq 20$ GeV with v2. The N×N clusterizer combines all towers in selectable N×N window.

3.3.2 Exotic clusters

High energetic calorimeter hits should spread through multiple towers as the electromagnetic shower evolves. High energetic clusters with vast majority of energy located in single tower have been observed. Such clusters are though to come from slow neutrons hitting the APD readout of the towers. The same effect was observed in CMS calorimeter, which shares the same APDs [144]. These fake clusters are called "exotic" clusters.

The removal procedure of exotic clusters is based on finding a ratio in between the most energetic tower ($E_{\max}$) in the cluster and sum of the four towers neighboring the most energetic one (E_{cross}). A measure of exoticity of the cluster is denoted as $1 - E_{\text{cross}}/E_{\max}$ with values in range of (-3,1) (Fig. 3.15). The closer to 1, the more exotic the cluster is, the more probability that it is fake. Similar algorithm can be run on all towers before the clustering to remove fake tower signals.

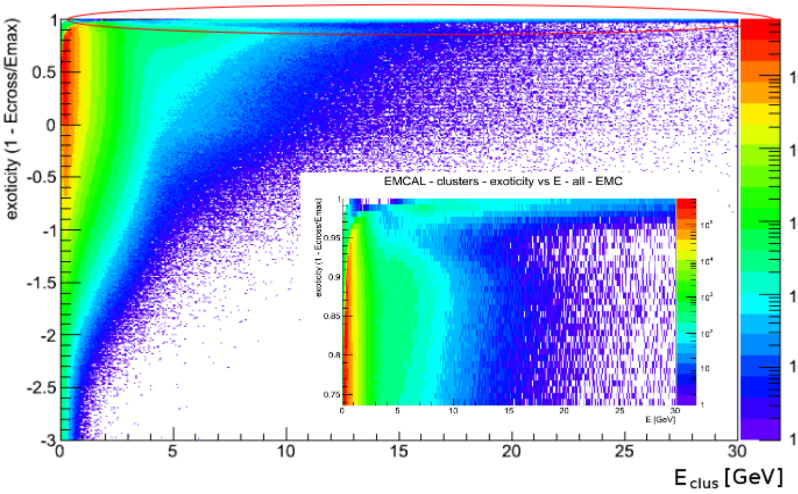

Figure 3.15: Exoticity versus energy of EMCal v2 clusters.The exotic clusters are highlighted by the red ellipse and zoomed figure is show.

It has been found that most of the high energy spectra comes from the exotic clusters (Fig. 3.16).

The procedure of removing exotic clusters precedes every analysis. Cut of 0.97 was adopted as default for the EMCal analyses.

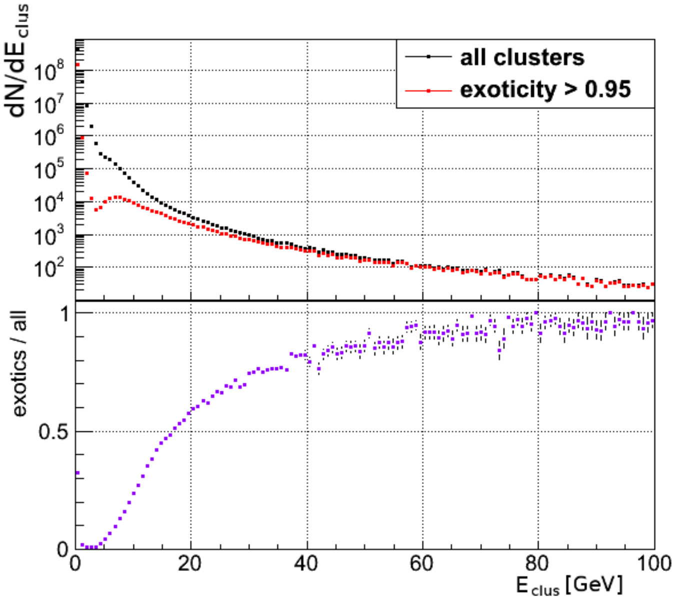

Figure 3.16: The frequency of exotic clusters as a function of E_{clus}. The lower panel shows ratio of clusters with exoticity > 0.95 to all clusters.

3.3.3 Cluster shape

The shower shape cuts evaluate the clusters in terms of different parameters arising from transverse shape [145]. The input values are usually weighted by logarithm of energies deposed in the single cells. Eccentricity of the cluster can be evaluated with analysis of eigen axis of the cluster according Eq. (3.2). The cluster's dispersion can be studied using Eq. (3.3).

Usage of these parameters is very dependent on the chosen clusterizer. The v1 clusterizer does not include any cluster splitting, and thus it is an ideal candidate to be used with shower shape analysis. With the v1 clusterizer it is possible to reject or identify merged π^0 originated clusters in relatively wide energy range (from approx. 6 GeV to approx. 20 GeV) and η-meson clusters for high energies when the two daughter clusters start to merge. One can also partially identify the converted photons.

$$\overline{\eta} = \sum_{i_{\text{cell}}} \frac{w_{i_{\text{cell}}}\ \eta_{i_{\text{cell}}}}{w_{\text{total}}}\ ,\quad \overline{\phi} = \sum_{i_{\text{cell}}} \frac{w_{i_{\text{cell}}}\ \phi_{i_{\text{cell}}}}{w_{\text{total}}}\quad ,\quad w_{\text{total}} = \sum_{i_{\text{cell}}} w_{i_{\text{cell}}}$$

$$w_{i_{\text{cell}}} = \max\left(0,\ 4.5 + \ln\left(\frac{E_{i_{\text{cell}}}}{E_{\text{total}}}\right)\right)\quad ,\quad E_{\text{total}} = \sum_{i_{\text{cell}}} E_{i_{\text{cell}}}$$

$$\delta^2_{\eta\eta} = \sum_{i_{\text{cell}}} \frac{w_{i_{\text{cell}}}\ \eta^2_{i_{\text{cell}}}}{w_{\text{total}}} - \overline{\eta}^2\ ,\quad \delta^2_{\phi\phi} = \sum_{i_{\text{cell}}} \frac{w_{i_{\text{cell}}}\ \phi^2_{i_{\text{cell}}}}{w_{\text{total}}} - \overline{\phi}^2\quad ,\quad \delta^2_{\eta\phi} = \sum_{i_{\text{cell}}} \frac{w_{i_{\text{cell}}}\ \eta_{i_{\text{cell}}}\ \phi_{i_{\text{cell}}}}{w_{\text{total}}} - \overline{\phi}\overline{\eta}$$

$$\lambda_0^2 = \frac{\delta_{\eta\eta} + \delta_{\phi\phi}}{2} + \sqrt{\frac{(\delta_{\eta\eta} - \delta_{\phi\phi})}{4} + \delta^2_{\eta\phi}}\quad ,\quad \lambda_1^2 = \frac{\delta_{\eta\eta} + \delta_{\phi\phi}}{2} - \sqrt{\frac{(\delta_{\eta\eta} - \delta_{\phi\phi})}{4} + \delta^2_{\eta\phi}} \tag{3.2}$$

$$\sigma^2 = \delta^2_{\eta\eta} + \delta^2_{\phi\phi} \tag{3.3}$$

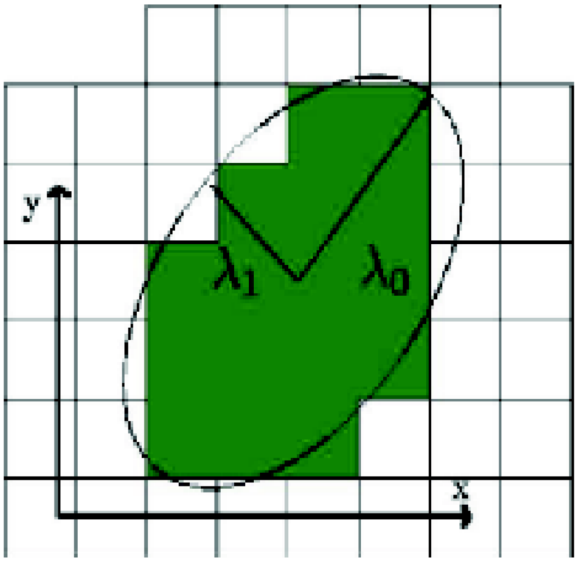

Figure 3.17: The λ eigen axes parameters visualization.

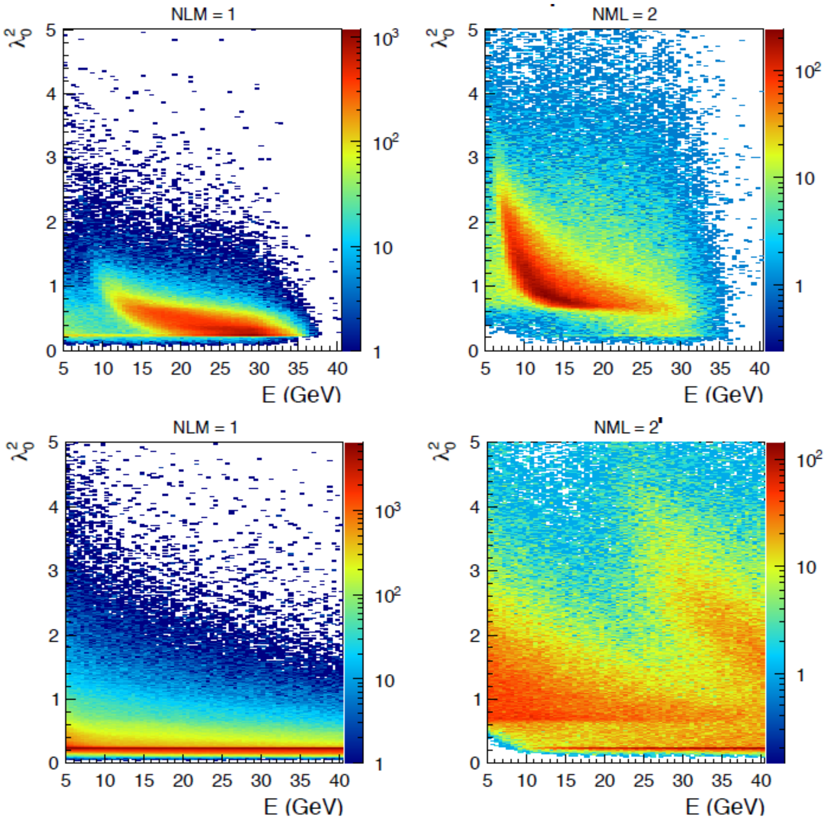

Figure 3.18: Simulation of shower shape λ_0^2 eigen axis parameter. Top for photon π^0 clusters, bottom for photons. The left and right plot differ in number of local minimum (NLM) found in the v1 cluster.

3.3.4 Track matching

A method of matching the cluster position to TPC track extrapolation is used to suppress charged hadron contribution to hits in EMCal. A track identified by the tracking detectors is extrapolated close to the EMCal surface, where the closest cluster is found and the track extrapolation is then continued until reaching the same depth as the cluster. The remaining distance in between extrapolated track and the cluster, residuals (Fig. 3.19), is then used for rejection of hadronic hits. The track extrapolation is not a straightforward process and the method depends on the data set used. For the raw data, the extrapolation happens from track definition coming from the outer TPC chambers (hence the ones closes to EMCal). ESD data[2] use inner chambers as a starting point and the AOD[3] data use vertex.

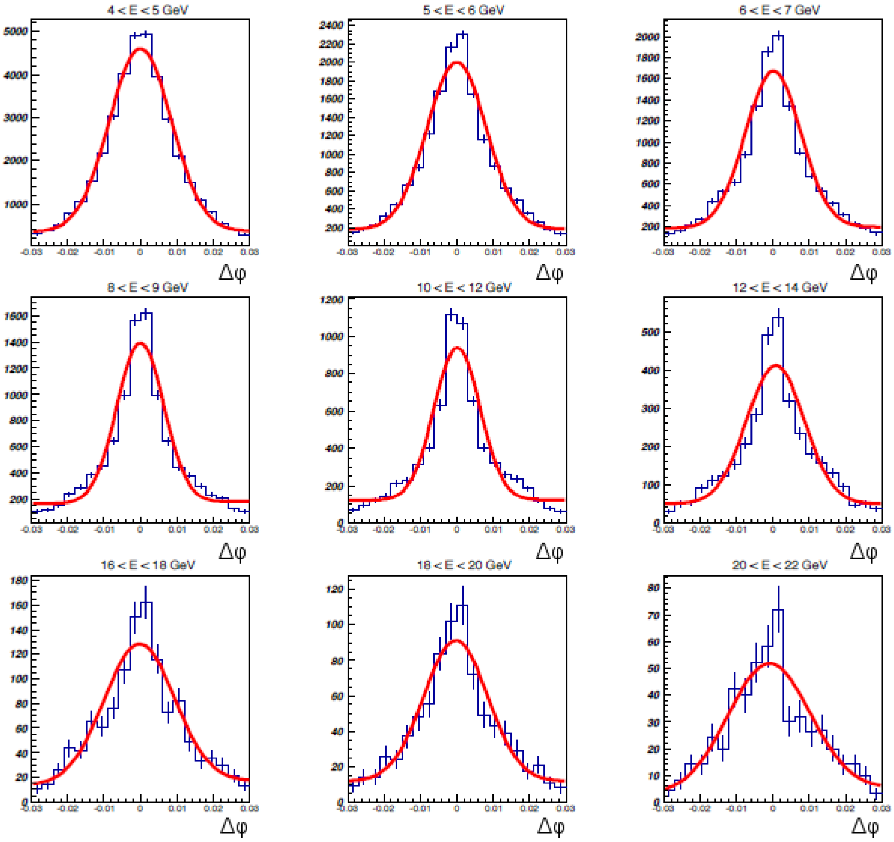

Figure 3.19: Track matching residuals in $\Delta\varphi$ for central (0-10%) Pb–Pb collisions. Different panels correspond to different E_{clus} bins. Distributions are fitted with Gauss+constant.

---

[2] ESD is data format for the data produced by reconstruction

[3] AOD is data format used to contain slimmed down information from ESD

3.3.5 Spectra decomposition

The raw spectra can be seen as being composed of various contributions. Exotic clusters, hadron and electron clusters, photon clusters, clusters from conversions all do contribute. Cuts on specific cluster parameters can be used to disentangle some cluster sources.

Exotic and track matched clusters are identified based on the methods described in sections 3.3.2 and 3.3.4. The cut on exoticity was chosen 0.95. The track matching cut was chosen standard for Pb–Pb collisions: 0.025 units in rapidity and azimuth (radians).

The decomposition of the cluster spectra is shown on Fig. 3.20.

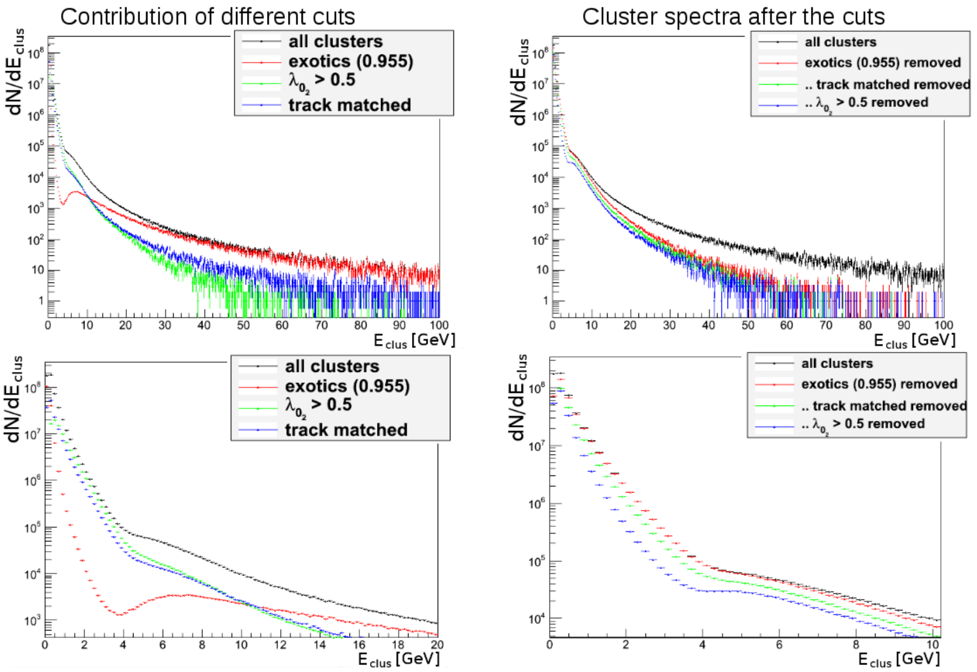

Figure 3.20: Cluster spectra decomposition as cuts identify exotic, track matched and asymmetric clusters. The bottom plots are zoom of the top row into lower E_{clus} region.

Chapter 4

Single Shower Trigger

The initial 2.5 years of the Ph.D. studies were spent at CERN working on the project of EMCal level-0 (L0) trigger. The task was to take over responsibility for already designed (and partially produced) L0 hardware, develop and program the L0 algorithm code, ensure following hardware production, installation, commissioning and trigger performance approval by the collaboration boards.

This chapter will describe the L0 trigger system in detail. The content is an extension of some information available in [142], which is a paper describing the development of the TRU firmware.

4.1 Overview

A separate stream of APD electric signals is created at the level of FEE. The stream is delivered to the dedicated L0 hardware Trigger Region Units (TRU) for composing the L0 trigger decision. Single bit OR of all TRUs in the EMCal is then forwarded to the ALICE Central Trigger Processor (CTP) as the EMCal L0 trigger decision (Fig. 4.1).

The trigger decision is based on evaluating energy deposits in area of 4×4 EMCal towers. Such area, in vast majority of cases, contains only a single shower (or two adjacent showers coming from a single decayed π^0), the trigger can be (with some approximation) called single shower trigger.

The trigger processing on the TRU is happening on the level of FPGA, which provides optimal performance in speed and reprogramming ability. A decision is produced for each LHC clock, after a specific latency given by the used hardware and algorithm. Major attention was given to speed of the algorithm during the development of the algorithm code. Optimizing the algorithm functionality much below the design specification was the only way to save invested money in the trigger system, after the hardware designers miss computed latencies of the used ADCs. To achieve the goal, various innovating algorithms have been developed for the signal processing.

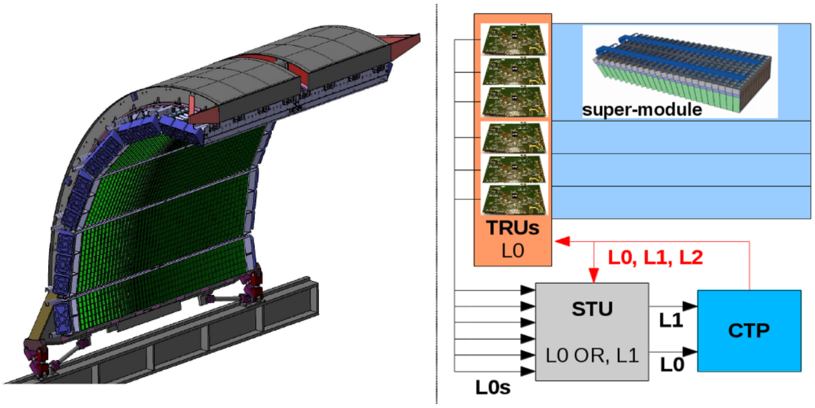

Figure 4.1: EMCal, TRU acceptance segmentation and decision path. Trigger decisions produced in TRUs are sent to STU and then forwarded as a single bit (OR) decision to CTP. CTP can confirm the event by issuing L0 message to electronics (red line). TRUs will provide primitive data to STU on reception of L0, so that STU can produce L1 trigger.

4.2 Trigger hardware

4.2.1 Trigger Region Units

The TRU is a dedicated calorimeter hardware trigger unit developed at CERN. The EMCal TRU is an enhanced version of PHOS TRU. Schematic view of TRU components is shown on Fig. 4.2, TRU picture is on Fig. 4.3. The TRU features up to 14 ADCs used to convert the electronic signal coming from the FEE (Fig. 4.4). 12 ADCs are used for EMCal. The Xilnix Virtex 5 FPGA performs all the digital processing. The algorithm code resides in FLASH memory programmable through JTAG chain. The code is loaded to the FPGA on each boot. Additionally there are LVDS and GTL divers present on the board to provide connectivity to the higher trigger and data acquisition units STU, SRU and RCU.

Power consumption of a TRU is presented in Tab. 4.1. The actual design under estimated the power requirements. The TRU has only 5 A voltage regulator on board for the 3.3 V line, causing the regulator to run above its specification when the TRU is operated (consumes 5.7 A). Additionally the least used 4.2 V line is doubled on the power connector, instead of the most used 3.3 V line. Leading to over heating of the connector in case of not “super” perfect contact. The hardware was already in production when the problem was discovered. Additional copper cooling plates were installed to cool the failing voltage regulators (there is no suitable replacement with similar foot print). Power connectors are replaced after 2 years of running to limit the current transfer problems caused by baking of the connector. The upgrade of readout electronics of EMCal/DCal and PHOS allowed optimization of the TRUs, GTL bus

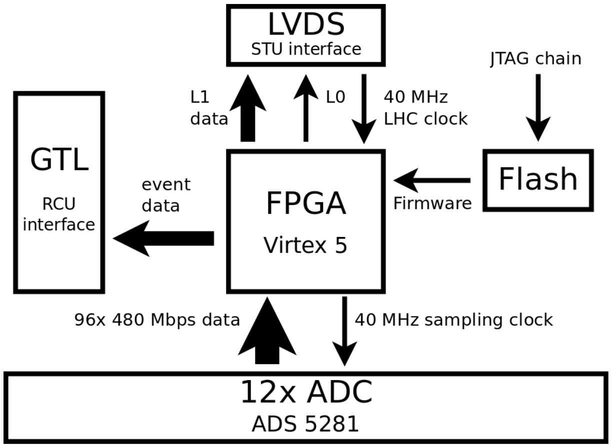

Figure 4.2: TRU functional schematics. The core part of TRU is FPGA which receives signal from towers digitized by on-board ADCs. Decisions and primitive data are shipped out via LVDS lines to STU. Flash memory keeps the FPGA program in between TRU reboots.

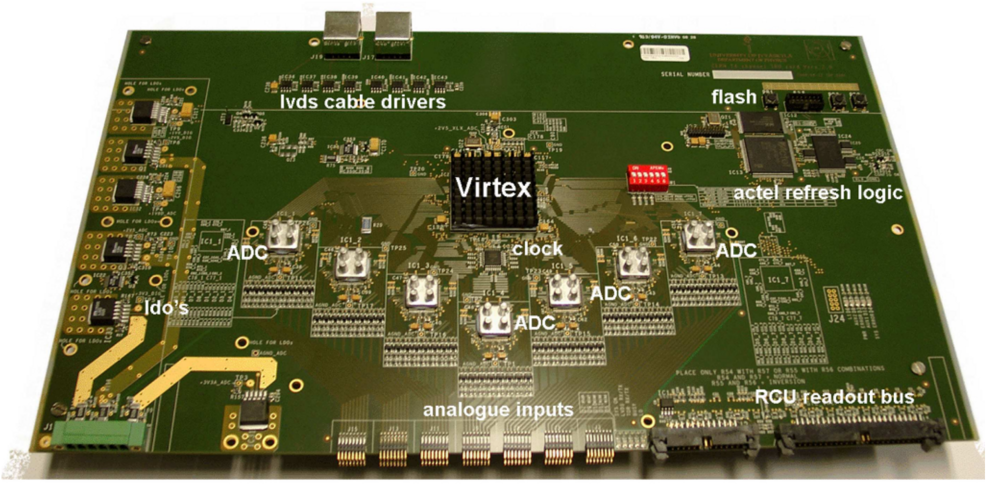

Figure 4.3: TRU prototype photograph (14 ADCs placed).

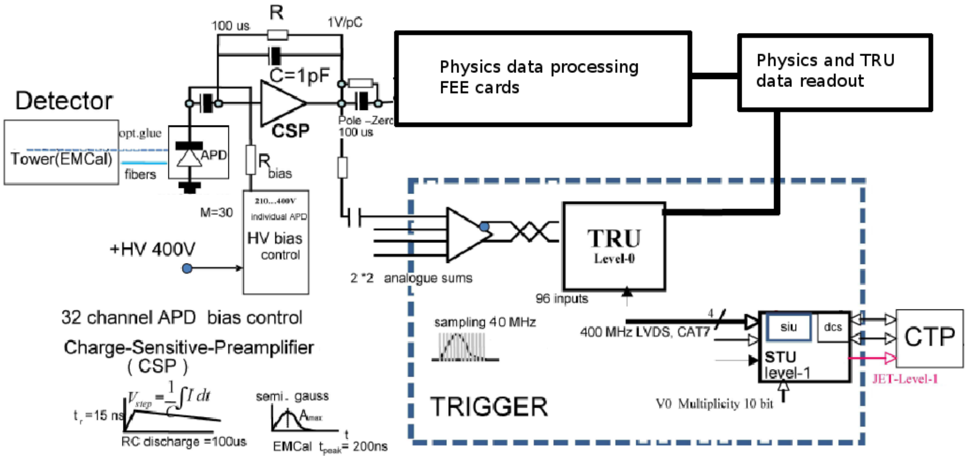

Figure 4.4: The path of the trigger signal in EMCal. Light signal from towers is captured by APDs, follows to Charse Sensitive Preamplifier (CSP) and then is forked into stream to Data Acquisition (DAQ) and to trigger. Analog sum of 4 towers is provided to TRUs. Decisions and data from TRU can be send to STU or DAQ.

drivers and several other low priority chips were not mounted on the newly produced boards. After this optimization the voltage regulators not being overloaded any more.

line/mode	3.3V	4.0V	4.2 V
programming	1.0 A	0.3 A	0.45 A
in reset	2.5 A	0.3 A	0.5 A
running	5.7 A	1.2A	0.55 A
optimized running	3.3 A	1.1A	0.65 A

Table 4.1: Power consumption of TRU for different power lines in different operation modes. The “optimized running” row corresponds to “running” mode of the new TRU version optimized for the upgraded EMCal readout.

The TRU ADCs are 12 bit flash ADCs operated at the LHC clock frequency (40.08 MHz). For testing purposes, the TRU is equipped with on-board 40 MHz oscillator, which is automatically used in case that the LHC clock is missing. Each ADC processes 8 signal channels, summing to 96 total per one TRU. Each ADC sends digital data to the FPGA via a dedicated single bit line operated at ADC word clock frequency (40 MHz per 12 bits = 480 MHz bit clock).

Data transmitted from the ADC is validated by clock also transmitted from the ADC. The receiver (FPGA) samples normally the arriving data with help of the arriving clock. Due to another failure of the hardware design, amount of returning clock lines from the ADCs conencted to a single FPGA logic bank is larger than the FPGA can handle. Special approach of recovery of the ADC data streams was developed. The arriving ADC clock can not be used due to the neglected limitation. The FPGA uses the supplied LHC clock to drive the ADCs, additionally it also synthesizes its own bit clock to recover the ADC data. This approach has proven working, but sensitive to the arriving LHC clock quality. The clock supplied by the RCU over relatively noisy GTL bus was found insufficient. Suitable clock was found to be the one coming from the STU link over high quality LVDS divers and twisted pair cat. 7 cables. The STU clock is also previously filtered on the STU by the QPLL high precision clock filer specially designed from the LHC application [146].

4.2.2 Hardware location and segmentation

There are 3 TRUs per EMCal full size Super Module (SM). The TRUs are placed along the FEE cards in the FEE crates (Fig. 4.5). The TRUs used to serve separate areas in φ. Segmentation in η will be preferred for the operation after the first LHC long shutdown stop. There are 2 reasons for segmenting in η: (i) DCal SMs will be of 2/3 length in η, one can then use the same setup in EMCal and DCal. (ii) The second reason is improvement of the time definition of the trigger. Currently the cables from APDs to FEE in EMCal are of different lengths. Arrival time of signal from mid rapidity differs in order of 30 ns to arrival time from areas in large rapidities. Trigger must be produced with 25 ns precision after the LS1 (50 ns precision was sufficient so far). The ADCs on TRUs share common clock driver (can not be phased). Hence segmentation in η will minimize dispersion of signal arrival time and provide better trigger timing, when a whole TRU is phase shifted based on region η.

There are total of 32 TRUs in EMCal. 30 in 10 full size SMs, 2 in the 1/3 SMs.

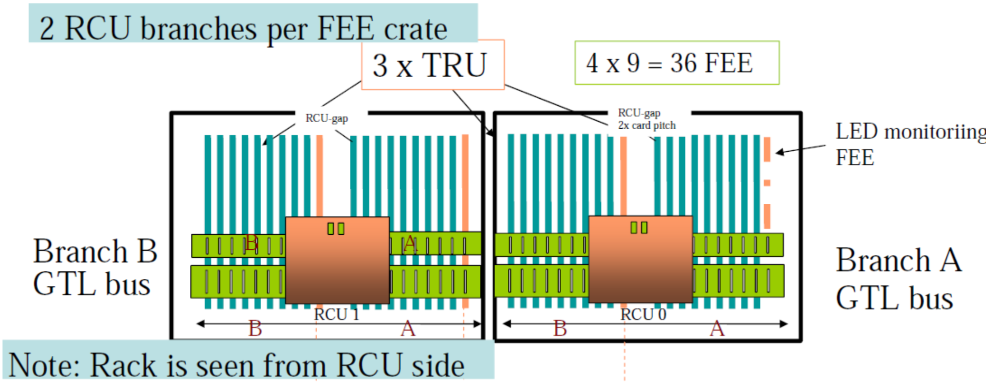

Figure 4.5: The EMCal FEE crate with FEE cards in blue, TRUs in full orange and LED calibration in intermittent orange.

4.3 Algorithm performance

4.3.1 Analog signal

The signal for trigger separates on the level of FEE from the signal that goes to the DAQ. In order to limit amount of channels, high granularity is not needed for trigger, exclusive analog sums of 2×2 towers are created (fast-OR) and provided to trigger as a single channel. Window of 2×2 trigger channels is equivalent to a window of 4×4 towers.

The fast-OR signal can be described as a Γ_2 function Eq. (4.1) and is shown on Fig. 4.6,

$$V(t) = \begin{cases} A \cdot x^{\gamma} \cdot e^{\gamma(1-x)} \; ; \quad x = (t - t_{\text{Max}} + \tau)/\tau & \text{x} > 0 \\ 0 & \text{x} \leq 0 \end{cases} \tag{4.1}$$

where A is amplitude at maximum t_{Max}, τ is time constant.

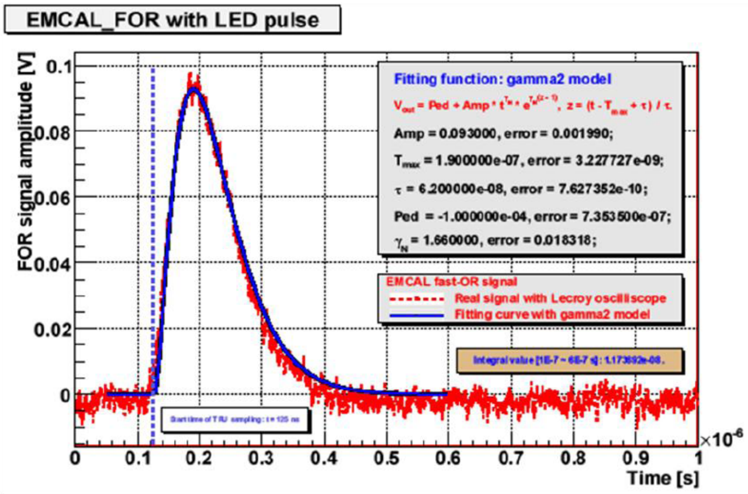

Figure 4.6: The trigger fast–OR signal as generated by a LED pulse, fit by Gamma–2 function.

4.3.2 Trigger algorithm

The level-0 algorithm compares energy deposits in a window of 2×2 channels (4×4 towers) to a constant threshold. Peak finding is implemented in addition to the threshold comparison to define correctly the time of the signal maximum. The signal shown on Fig. 4.6 is sampled by a 25 ns sampler (ADCs). High amplitude signals can cross threshold one or two samples before maximum, so a correct peak finding is necessary.

The digital data stream from the TRU ADCs is recovered in the FPGA by the deserializer. A 12–bit value is available for each channel on every clock (LHC clock of ≈ 40 MHz $= 25$ ns). The first step of the algorithm is channel masking. Faulty channel values are zeroed, so those do not interfere later. The second step is time summing and pedestal subtraction. Full algorithm scheme is available on Fig. 4.7.

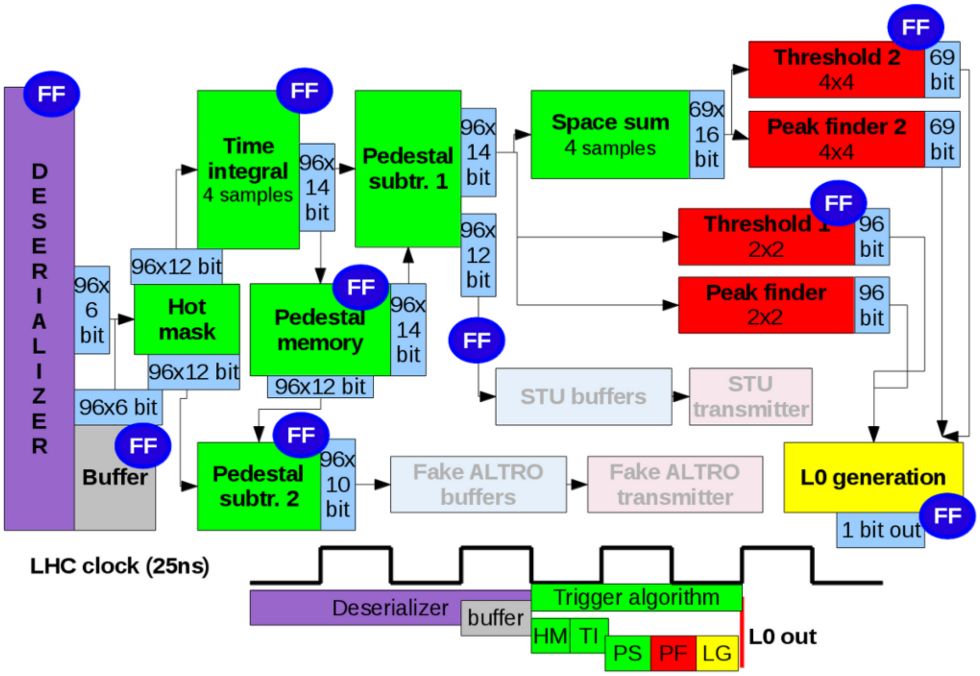

Figure 4.7: Schematics of the trigger algorithm. Bottom part of the picture shows timing analysis of the code in respect to LHC clock, blue circles with FF label show position of the FPGA flip-flop in the algorithm. Data flow and word widths are also displayed. Data reception is color-coded in violet, signal processing in green, trigger conditions in red and decision generation in yellow.

A sum of 4 latest samples is created on every clock, thus creating a 4 sample time integrated version of the signal. Based on the fast-OR signal shape, the integrated signal amplitude is a constant factor 3.4 higher than the amplitude of the fast-OR signal. The amplitude position of the integral shifts to later time (by ≈ 50 ns). Even number of samples to sum was chosen for the fact that the FEE superimpose a coherent 20 MHz noise on the fast-OR signal (Fig. 4.8). Summing only 2 samples proved to be too few to minimize the noise, summing of 6 would impose additional delay and thus not allow the trigger to function within the limited available time.

The amplitude of the digitized (and also the time integrated) signal is dependent on the sampling phase of the ADCs. Sampling the signal on different phases does deliver a different maximum sample. The uncertainty was studied on the level of time integrated

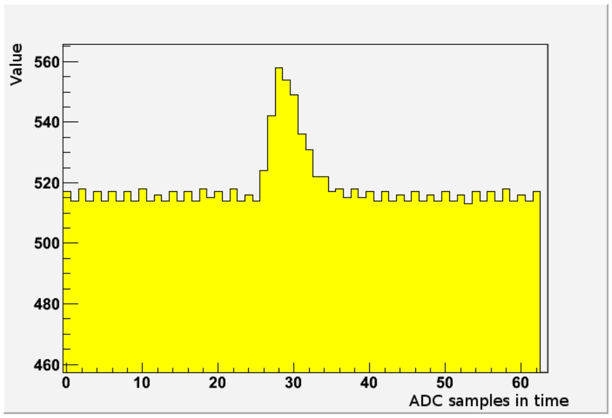

Figure 4.8: The trigger raw signal showing a LED generated pulse. The 20 MHz noise from FEE is well visible.

signal (Fig. 4.9) and was found to be very small (≈ 60 MeV for 2 GeV signals).

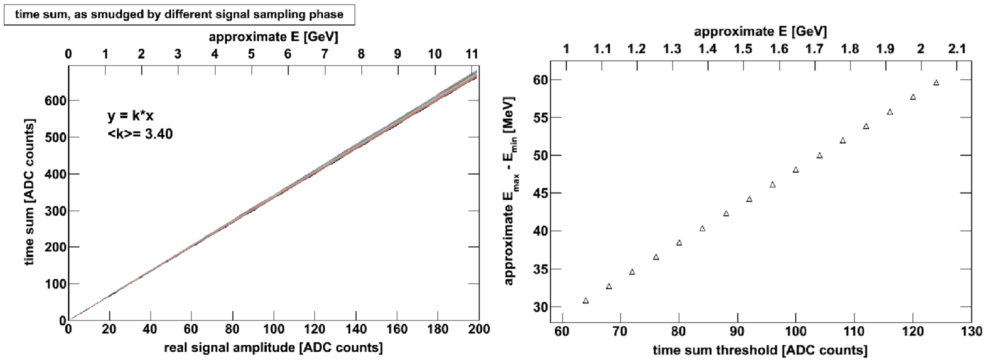

Figure 4.9: Left: time integrated signal amplitude as a function of analog signal amplitude for different sampling phases. Right: Difference between minimum and maximum time integrated amplitude for identical analog signal as a function of analog signal amplitude. The energy scale is approximate due to imprecise relation in between ADC counts and MeV, given by online calibration.

Subtraction of the signal pedestal is the next step in the algorithm. Copy of the time integrated signal is delayed for 13 clocks and then used to subtract the pedestal of the current time integrated sample. This approach was chosen as the only possible (due to algorithm complexity limitation given by the short time available). This approach could cause inefficiency in case of consecutive hits in one tower within ≈ 350 ns, which happens extremely rarely.

The pedestal subtracted signals are processed by the sliding window algorithm (Fig. 4.10) of 2×2 channels (4×4 towers) in order to produce the final amplitude that is then compared to the threshold (space sum). The 2×2 channel window is essential in order to capture correctly energy of hits that happen at the borders of the channels. Each TRU can process only it's own channels, hence the window does not cross the single TRU acceptance boarders, leaving inefficiencies at the edges. The level-1 gamma algorithm targets to remove those inefficiencies as it has data from all TRUs available.

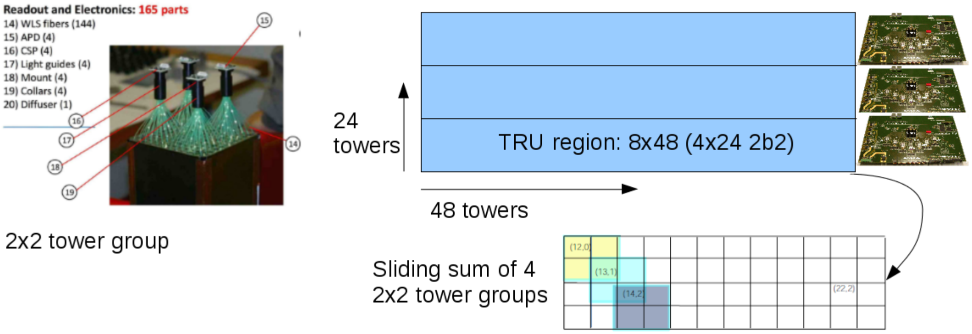

Figure 4.10: 2×2 tower module, the TRU regions in the super module and the sliding window algorithm.

The peak finding decision is issued after a defined sequence of rising and non–rising samples (Fig. 4.11). A sequence of 4 rising followed by 1 non–rising sample is used (due to signal shape). The peak finding was operating originally on single trigger channels instead of the 2×2 window. This approach provided slightly better time resolution for channels with signal, but significantly decreased the time resolution for 2×2 windows, which had one signal channel and others with noise only. The noise channels could have provided peak decision when the signal channel already passed threshold but was not at maximum yet. The peak finding was switched to run on the 2×2 space summed signal after the first months of operation.

The threshold and peak finding decisions for each 2×2 window are composed together and the ORed for a production of the final single bit signal.

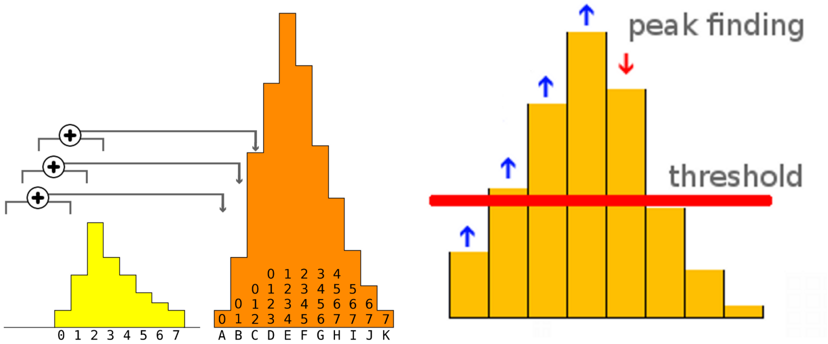

Figure 4.11: Left: the 4 time samples integration. Right: threshold and peak finding.

The time integrated signals are saved in a large rotating buffer from which a single sample is extracted and provided to the level-1 trigger unit (STU) after CTP confirms an event with L0 message (Fig. 4.1). The time integrated signals are 14–bit wide, STU accepts 12–bit words, the 2 Least Significant Bits (LSB) are cut. The raw digital signal (before time summing) is also pedestal subtracted (division by 4 of the time integrated pedestal is used) and saved in a rotating buffer. Arbitrary amount of 10 bit wide words (2 LSB cut) can be then copied to multi–event buffer and sent to DAQ. Along with the raw signals, the trigger decisions for each channel are saved and provided to the DAQ. Such data streams are very useful for debugging purposes.

The ALTRO chips (and very possibly the GTL drivers) are very noisy during the signal processing and readout time. They do generate an extensive electronics noise that propagates to the trigger system after each L0, L1 message from CTP and during the readout (Fig. 4.12). A configurable time based masking is available after L0, L1 and in readout to mask the fake trigger production. The trigger decision output is simply masked during a defined period after each strobe. The periods are listed in Tab. 4.2. The readout time is defined by activity on the readout bus. The TRU watches for read commands to other FEE cards in a crate and masks the trigger production for a defined time after a read command is detected.

after L0	5 μs
after L1	200 μs
in readout	1.2 μs

Table 4.2: Trigger production masking times after L0, L1 and in readout.

4.3.3 Level-1 trigger

The level-1 unit (STU) gathers a single 12–bit word (amplitude) per channel for the whole EMCal acceptance. The data is transmitted by all TRUs in parallel after receipt of the L0 trigger from the CTP. The STU recomputes the 2×2 sliding window to produce single shower trigger. All data are available to the L1 single shower trigger, so it does not suffer from efficiency losses TRU acceptance borders. The STU can also compute a larger 16×16 window sliding by 4 channels to produce a jet trigger.

The STU can compare to up to two thresholds for each single shower and jet trigger (thanks to multiple L1 decision signal cables that are pulled in between STU and the CTP). There is a dedicated link in between the V0 detector and EMCal STU, which can provide centrality (V0 multiplicity) information. The STU can compute a dynamical threshold (polynomial of 2^{nd} order) as a function of the V0 multiplicity.

The STU is fully digital and processes single sample in time only. The data from STU can be as well transferred to the DAQ for debugging purposes.

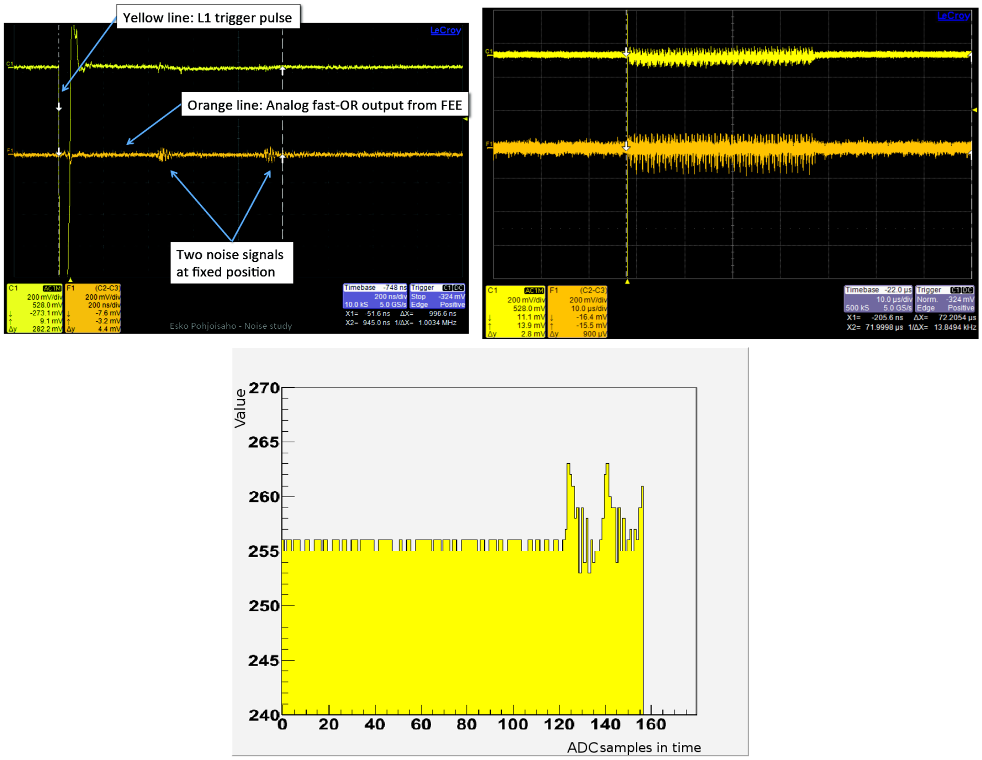

Figure 4.12: Laboratory test of noise production by FEE and propagation to the trigger on the fast-OR lines. Left: noise on the fast-OR after L1. Right: noise in read-out. Bottom: as seen by TRU ADCs.

4.3.4 Trigger timing

The ALICE CTP accepts L0 trigger arriving up to 850 ns after the collision. 1200 ns after the collision, the CTP decision reaches the FEE of the detectors. 7.3 μs after the collision, the CTP accepts decision from the L1 trigger units.

A detail timing analysis of the TRU is available at [142]. A short summary is given here. Out of the 850 ns L0 window, $\approx$ 480 ns are available for the TRU, the rest is consumed by signal transport. Detail view of timing is shown on Fig. 4.13. Out of the 480 ns, $\approx$ 315 is taken by the flash ADCs, leaving 165 ns for the FPGA processing. Out of the 165 ns available to FPGA, 75 ns are consumed by the signal shape requirements (rise time, fall time for peak finding), 50 ns are consumed by the recovery of the data stream from the ADCs (deserialization). Only 40 ns are left for the FPGA to process the algorithm. All computational operations happen within 1.5 LHC clock (37.5 ns).

Original design time for the algorithm was 160 ns (instead of 40 ns). The hardware designers miss computed the ADC latency (expected 170 ns instead of 315 ns). Several dozens of ns were recovered by shortening the cable path from STU to CTP (to bare minimum). A 1.5 LHC clock for the algorithm was secured by the cable cutting (equivalent time to signal propagating along $\approx$ 10 m of cable). The FPGA algorithms were optimized and programmed to fit in the window.

All TRUs transmit single value for each channel to STU, after reception of the confirmed L0 from the CTP at 1200 ns. The transmission happens over 2 bit wide bus with LHC word clock (12 bits per one clock = 240 MHz). The L1 unit starts to produce the decision after all data from TRUs have arrived. The L1 decision is available $\approx$ 6.1 μs after collision.

4.4 Trigger hardware commissioning

Target of the hardware commissioning is to validate functionality of the TRU boards and interplay of the TRUs with other ALICE hardware.

4.4.1 TRU board

The commissioning of a TRU board consist primarily of basic functionality checks. Voltage level check can reveal failing regulators. Unstable power supply to the chips has severe consequences to the TRU functionality. Current draw check is also required. The functionality of FLASH and programming chain of the TRU is tested next.

A programmed TRU is connected to DAQ and control buses and an ADC stability test is performed. The 480 MHz link in between the ADCs and FPGA is fast enough, that chip to chip differences change the reception phases of the serial data in the FPGA significantly. To overcome this dynamic behavior, an automated mechanism of tunning the best phase for each ADC on board of TRU was developed. Stability

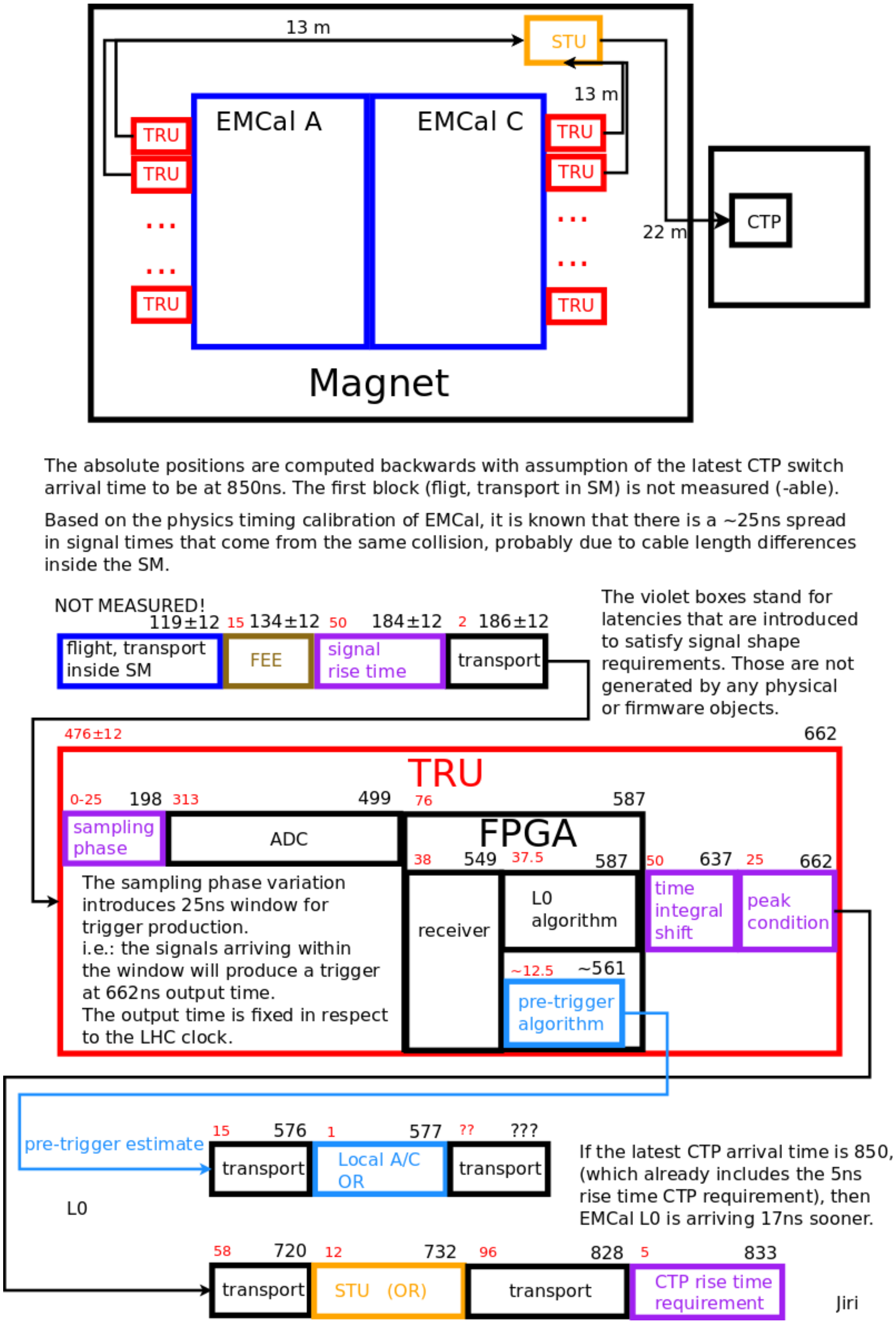

The absolute positions are computed backwards with assumption of the latest CTP switch arrival time to be at 850ns. The first block (fligt, transport in SM) is not measured (-able).

Based on the physics timing calibration of EMCal, it is known that there is a ~25ns spread in signal times that come from the same collision, probably due to cable length differences inside the SM.

NOT MEASURED!

The violet boxes stand for latencies that are introduced to satisfy signal shape requirements. Those are not generated by any physical or firmware objects.

The sampling phase variation introduces 25ns window for trigger production.
i.e.: the signals arriving within the window will produce a trigger at 662ns output time.
The output time is fixed in respect to the LHC clock.

If the latest CTP arrival time is 850, (which already includes the 5ns rise time CTP requirement), then EMCal L0 is arriving 17ns sooner.

Figure 4.13: Trigger timing in EMCal showing all latencies and delays. A fast envisaged pre-trigger for TRD is also shown.

of data reception by the FPGA needs to be tested. Fig. 4.14 shows a stability test of two TRUs. The core of the stability test is to impose an artificial delay on the data incoming from the ADCs, so that sampling phase of the serial lines changes. A pattern is programmed into the ADCs, the FPGA recovers the pattern in case of correct reception of the ADC data. Single bit sampling stability can be tested in this way. In operation, the TRUs scan automatically the stability of decoding after each reset and adjust the decoding phase for each ADC to center of one of the stable regions. This tests also validates the precision of the self–tunning mechanism.

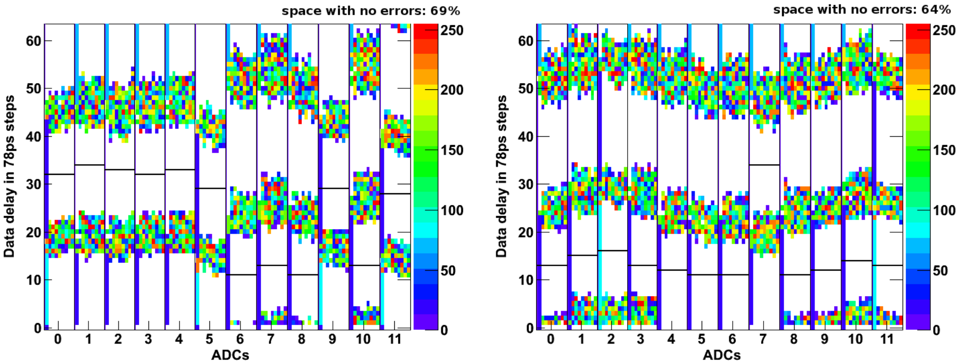

Figure 4.14: ADC stability test of 2 TRUs. The y axis shows an artificial delay imposed on the incoming data. With 480 MHz speed, single bit width is about 2 ns. The y axis spans over ≈ 2 bits. The x axis shows 12 TRU ADCs each of 8 channels (with the left most additional line showing stable single bit area). The z axis shows error counts of decoding a pre-programmed patter. The black lines show result of the automatic stable position tunning algorithm that is run after each TRU reset. It is obvious that the areas in between bit transitions do often fail to decode the patter. However it is important that the stable area is wide enough to ensure correct functionality during the running.

4.4.2 Fast–OR commissioning

It should be checked that the signal seen by the trigger is corresponding to the signal seen by the DAQ. In this way a wrong connections of cables that deliver the fast-OR from FEE to TRUs can be identified. The method consists of running a calibration run with signal supplied by the LED calibration system. TRUs and FEE both provide data to the DAQ. Amplitudes of the data are compare and should give a constant ratio. Fig. 4.15 shows a result for a random super module.

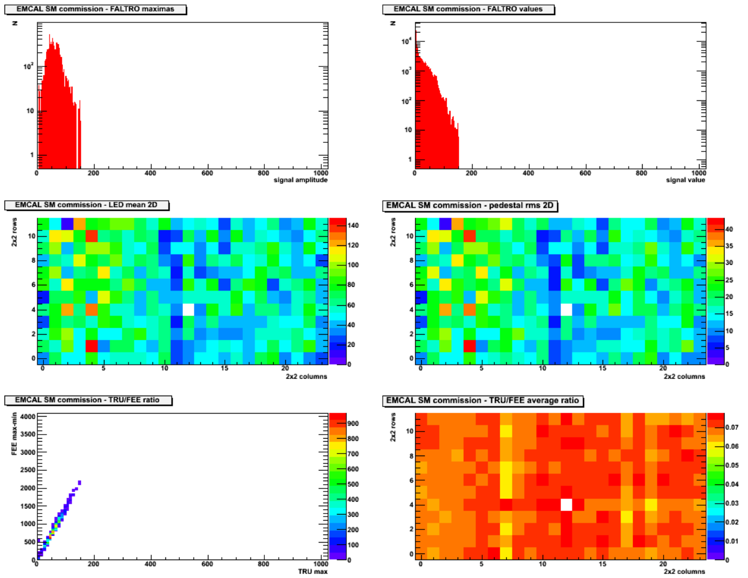

Figure 4.15: TRU to FEE data comparison. Left top: TRU amplitudes spectrum. Right top: TRU sample spectrum. Left middle: Mean FEE amplitude in 2D view of the super module. Right: Pedestal RMS Left bottom: FEE vs TRU amplitude. Right bottom: Mean TRU to FEE ratio for each channel.

4.4.3 Phase alignment in CTP

The CTP samples the incoming L0 signal from the STU. It must be assured that the CTP samples the L0 signal when it is stable, far from rising or falling edge (much like the stability of FPGA sampling the serial data lines from the ADCs). Additionally the STU is composing the L0 OR without usage of flip-flop layer (to save time), hence there can be a dispersion in arrival times from different TRUs.

The CTP can sample the incoming signal on a rising or a falling edge of the LHC clock. This provides sufficient granularity for the 25 ns long L0 signal. The CTP also provides a utility to sample the incoming signal on much finer phases, so it can be determined where the rising and falling edge of the signal lies and a correct sampling position can be chosen. The CTP decides once per 25 ns, but it can sample twice within the same time window, the sample at a falling edge of the LHC clock is delayed for half the clock to produce decision identical to sampling on the consecutive LHC clock rising edge.

The test is performed by programming sequentially the TRUs to supply periodic 20 MHz of positive trigger decisions, such that only one TRU is active at a time. The CTP then scans for the edges for each TRU signals. Fig. 4.16 shows the result of such a test. There is an ≈ 4 ns dispersion observed in between various TRUs.

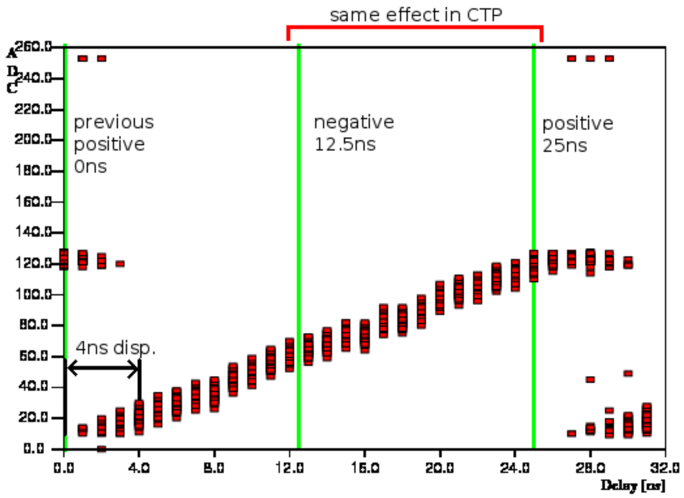

Figure 4.16: Signal arrival phase scan of all TRUs in EMCal in CTP. Green lines mark the CTP sampling positions separated by 1/2 of LHC clock. Two of the sampling phases will yield same timing always. Red boxes stand for incoming trigger signal. Incoming pulse will start to increment the y value until it is reset at the end of the pulse. The dispersion of the red boxes shows phase variation in between the TRUs.

4.4.4 Timing in CTP

The CTP accepts triggers arriving in the correct bunch crossing only. The shift in whole multiples of bunch crossings is checked in CTP via SMAQ utility[1] (Fig. 4.17). The CTP can delay incoming signals for certain amount of clocks in case that the detector supplies the decision sooner. TRUs have ability of additional delays (which are not used for obvious reasons).

It should be noted here that EMCal has a poor timing resolution given by the fact, that cables that bring the signal from APDs to FEE are of different lengths. This induces different latencies for signals from close and far towers. Additional differences in arrival time are caused by a fact, that some super modules were assembled using different sets of APDs, which seem to also induce a shift in time. More on the topic was discussed in the chapter 3.

4.4.5 DAQ loop stability

The TRUs receive the L0 confirm signal via the DCS board and RCU. It must be ensured that the signal is sampled with a correct phase, to avoid possibility of jitter. The test is performed with EMCal triggering itself by fake triggers and collecting data

---

[1] SMAQ is an utility that monitors trigger decisions registered at CTP as a function of the beam orbit. It was developed by Jan Rak et al. from University of Jyväskylä.

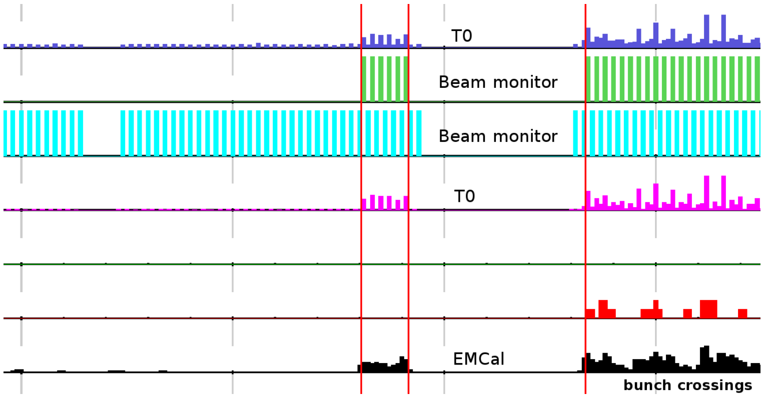

Figure 4.17: Trigger decision arrivals in the CTP, by bunch crossings, as seen by the SMAQ utility.

from TRUs. The data from TRUs contain a time marker when the TRU issued a fake trigger, hence it can be observed how far in the rotating buffer the marker falls before it is copied to MEB on L0 reception from CTP. There is no jitter in the position, when a correct sampling is set (Fig. 4.18).

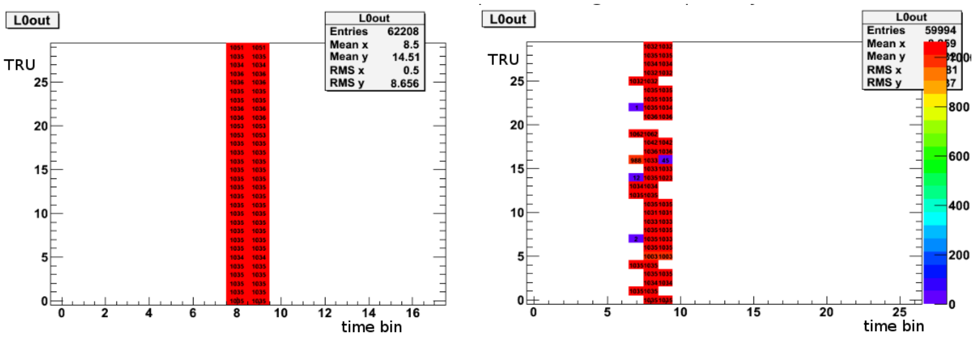

Figure 4.18: DAQ loop stability test. Left: correct sampling, with all TRUs aligned well. Right: incorrect sampling with some TRUs shifted and some jittering.

4.4.6 Rollback tunning

TRU contains the two rotating buffers, which do save the primitive data. One saves raw data for the DAQ, the other saves time summed data for the STU. It must be ensured that the correct subset of the buffer is copied to MEB or STU on reception of the L0 from the CTP (Fig. 4.19).

The rollbacks are trivial to retrieve from knowledge of correct phasing of the TRU and the functionality of it's firmware. The DAQ receives multiple signals in time, hence a check for presence of a signal is trivial. The STU receives a single value, a check of

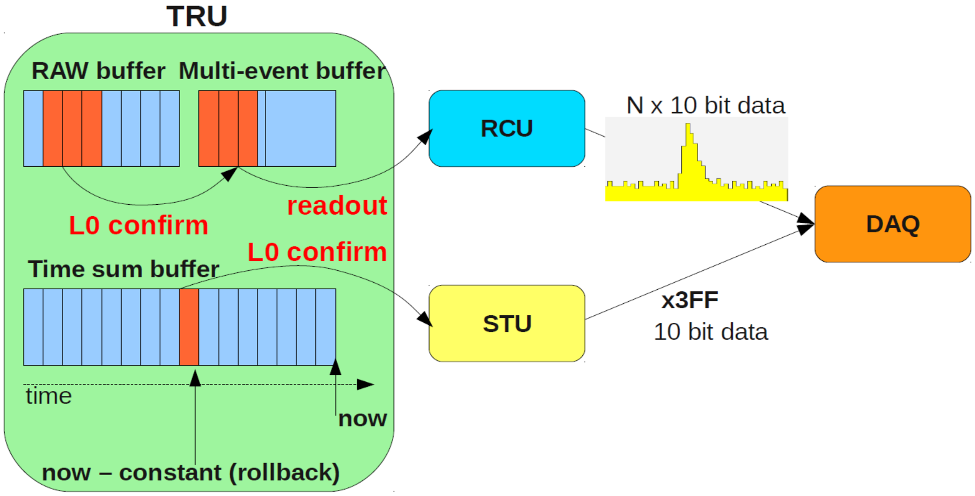

Figure 4.19: Rollback operation in TRUs.

the STU rollback can be performed by acquiring raw data from the TRU, producing a time sum offline and then comparing it to the time sum acquired from the STU (Fig. 4.20).

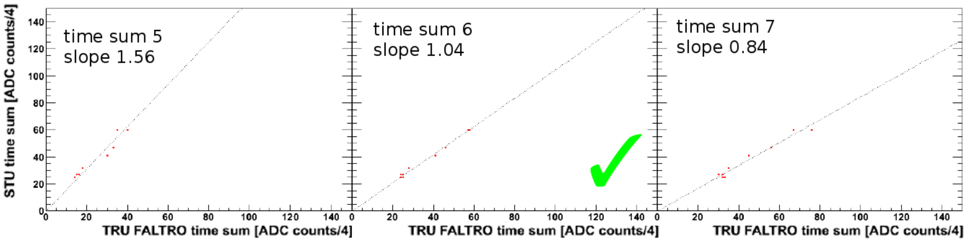

Figure 4.20: Comparing offline constructed time sum from raw TRU data with the one from STU obtained with three consecutive rollback values.

4.4.7 Online calibration

The gain of the APDs can be calibrated by changing the bias voltage, so that all towers provide roughly same signal amplitude per MeV. The bias voltage of the APD can be slightly regulated in a limited range. Decrease of the gain results in lower energy resolution of the physics data, hence it is always a compromise in between energy resolution of trigger and physics data.

The online gain calibration is not part of the trigger subsystem, yet it is desirable to have the APD gain well calibrated, as it directly influences the trigger energy resolution. Large discrepancies in the calibration could lead to trigger malfunction especially in cases of large patch size (jet trigger). The online gain calibration were discussed in more detail in the previous chapter.

4.5 Trigger performance commissioning

The performance of the trigger is evaluated in terms of efficiency, purity and energy resolution. In other words, how efficiently the trigger recognizes cases when it should trigger, if the trigger is not producing decisions without corresponding physics events and how sharply the decisions follow the energy threshold.

4.5.1 Trigger efficiency and purity

The efficiency is in general evaluated by dividing two cluster spectra; triggered spectrum $\mathrm{d}N_{\mathrm{trg}}/\mathrm{d}E$ with the minimum bias $\mathrm{d}N_{\mathrm{MB}}/\mathrm{d}E$ spectrum (Fig. 4.21). The normalization factor is the ratio of triggered events N_{trg} and the events from MB sample in which the trigger provided positive decision, $N_{\mathrm{MB,trg}}$ so that the numbers of 'triggered" events are identical Eq. (4.2). The difference to the MB spectra is then the inefficiency of the trigger (Fig. 4.22).

$$Eff(E) = \frac{N_{\mathrm{MB,trg}}}{N_{\mathrm{trg}}} \frac{\mathrm{d}N_{\mathrm{trg}}/\mathrm{d}E}{\mathrm{d}N_{\mathrm{MB}}/\mathrm{d}E} \tag{4.2}$$

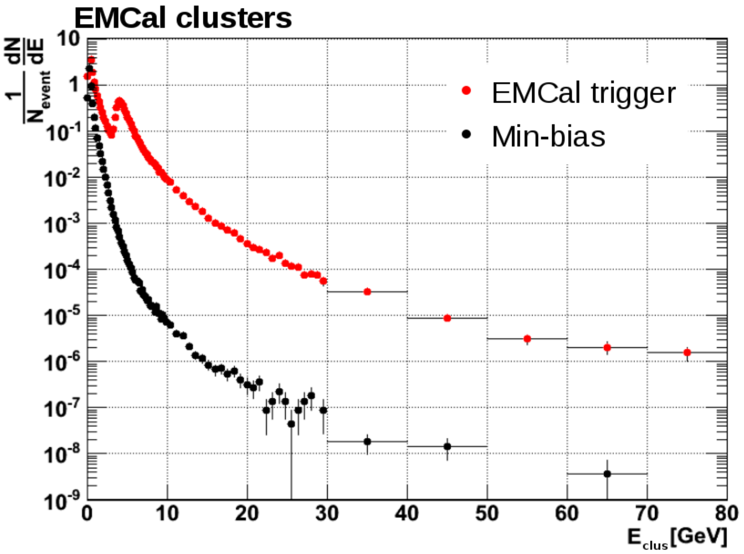

Figure 4.21: Cluster spectra in EMCal of triggered and minimum bias data sample, normalized per event.

The ability of the trigger to provide detail information on the decision to the DAQ allows for a simple and fast functionality check. Each trigger decision is recorded and can be linked to an offline reconstructed cluster. It can be then checked, as a function of energy, for what fraction of the clusters there was a decision issued (Fig. 4.22).

The energy resolution translates into the steepness of the turn on of the efficiency curve. The better energy resolution the steeper the curve.

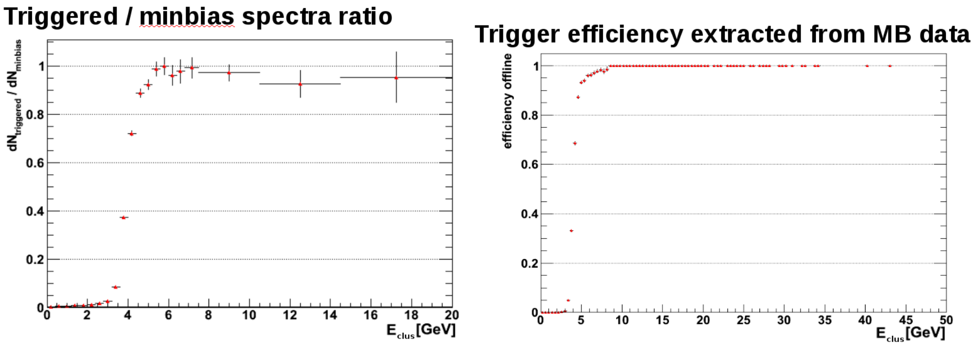

Figure 4.22: Left: Level-0 trigger efficiency. Right: Simple offline check for fraction of clusters that produce a decision.

Trigger purity is evaluate by checking how many of the triggered events do contain high energetic cluster. Fig. 4.23 shows a fraction of events which do contain a cluster of a higher energy.

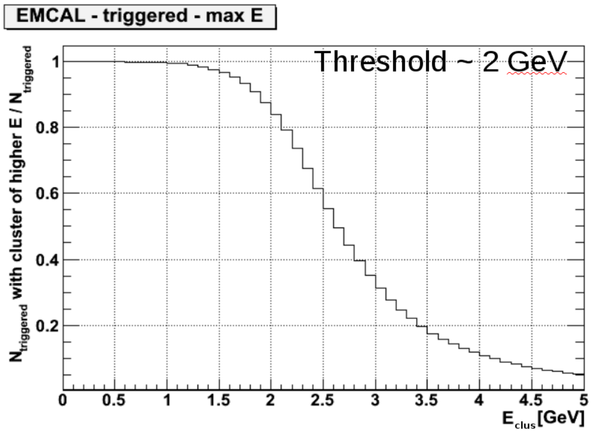

Figure 4.23: Fraction of events containing a cluster with higher E_{clus}.

4.5.2 Rejection factor

Rejection factor denotes the fraction of minimum bias events that do not satisfy the trigger condition. The factor is obtained by division of triggered and MB spectra, both normalized per event. The factor is directly dependent on the trigger threshold (Fig. 4.24).

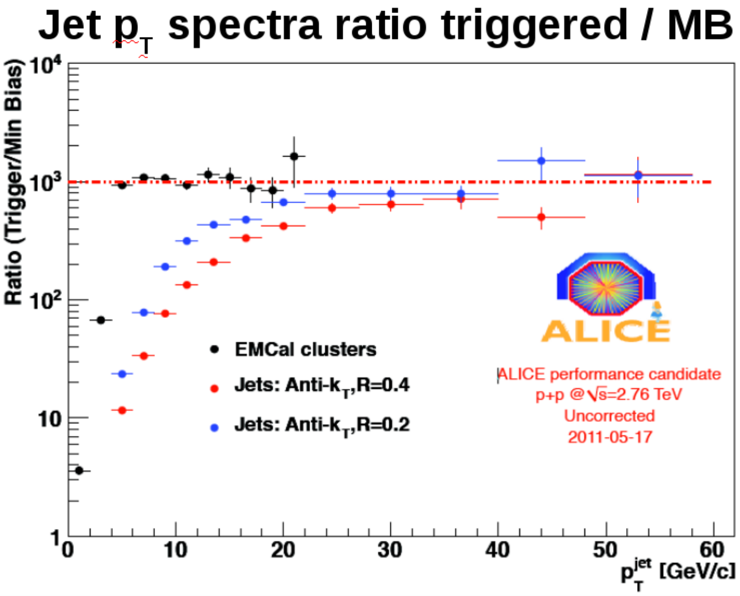

Figure 4.24: Level 0 trigger rejection factor for clusters and jets.

4.5.3 Additional performance checks

The trigger production should be homogeneous in the acceptance. A check of trigger production as a function of originating channel is possible thanks to the ability to save decision data in the event data stream. Fig. 4.25 shows such trigger production information. It can be seen from the figure that there is a repeating horizontal linear structure in the trigger multiplicity. This structure arises from inefficiencies of trigger production on the borders of the TRUs. Additionally there is a recognizable vertical structure, which corresponds to the space frame and TRD material budget. There is also an obvious rise in trigger multiplicity for one of the super modules. The rise comes from inaccurate online APD gain calibration.

The same figure shows also a check of trigger production times as seen in the offline data. Each decision leaves a time stamp in units of bunch crossing. The time stamps should be aligned in one bunch crossing. This is not entirely possible to achieve in EMCal due to dispersion of the signal arrival time.

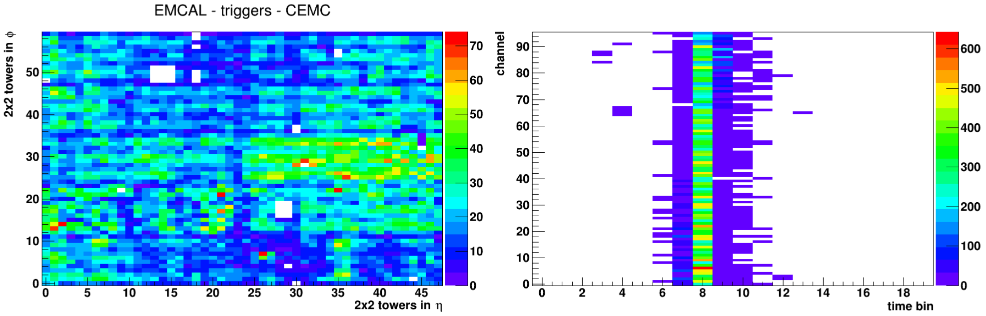

Figure 4.25: Left: Spatial production of triggers. Right: Trigger production times. Each time bin corresponds to a bunch crossing. The spread in time of the trigger production is a result of timing inhomogeneity of SMs (3.2.6), also some slower particles can produce trigger in later times.

4.6 Detector control system

The Detector Control System (DCS) for the trigger is a part of EMCal DCS, constructed with the same building blocks (PVSS, DCS boards, ...). The trigger DCS provides configuration, monitoring and archival of configuration and status data.

4.6.1 Configuration

Each TRU parameter can be configured through the DCS. The values requested by the operator are saved in the PVSS database and forwarded to the hardware. Description of the complex setup options for each TRU are out of the scope of this thesis. The detail can be found in the TRU configuration guide [147].

For each configuration change requested by the operator there is a read back value, to confirm that the configuration of the hardware did happen.

4.6.2 Monitoring and archival

All TRUs are periodically monitored. Whole TRU configuration is pulled on each start of run. Parameters crucial to monitor of the stable running condition are pulled periodically each 5 minutes. The slow polling speed is due the general EMCal DCS slow communication rates. Selected values are saved in database archive for reference purposes. Two values (on start and end of run) are transmitted to DAQ (via ALICE shuttle) for a small subset of the archived values. Those values (threshold and algorithm setting, channel masks) are then used for simulation or reconstruction.

There are alarms in place, that will alert DCS operator if any of the monitored parameters has crossed a defined threshold values. A successful attempt was made in connecting selected alarms to SMS service, so that EMCal expert receives a text message in case of problems.

4.6.3 User interface

User level panels provide configuration of each TRU (Fig. 4.26) or oversight of the whole trigger system (Fig. 4.27).

The overall control provides easy interface to mask and unmask noisy towers. There is an integrated automatic algorithm on the level of DCS, which can identify noisy towers and propose masking to the operator.

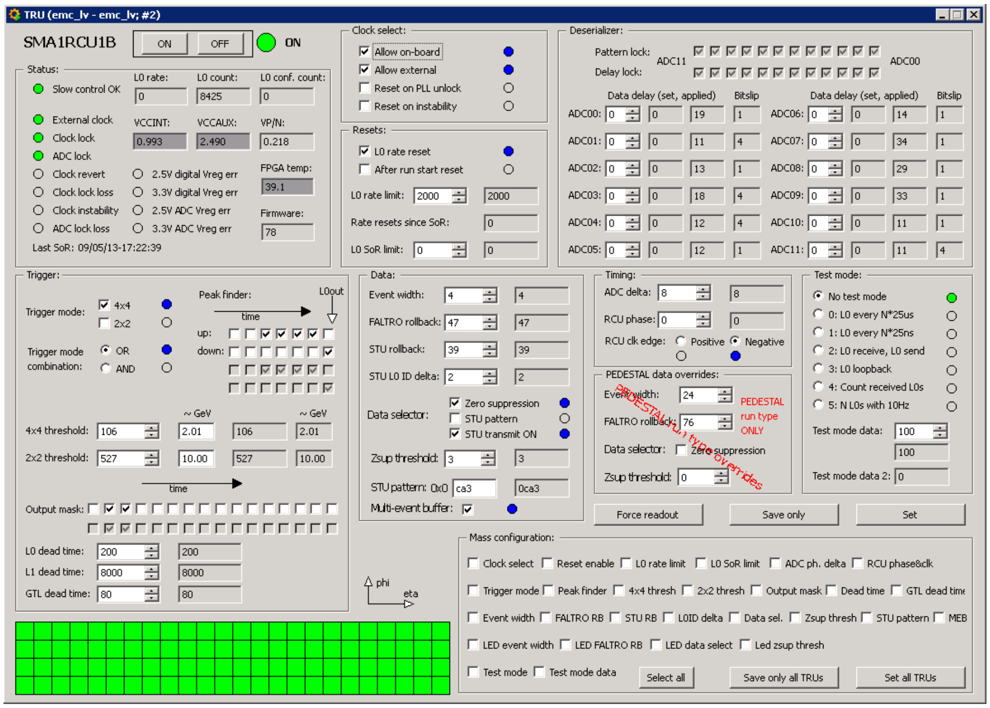

SMA1RCU1B ● ON

Status:
● Slow control OK
● External clock
● Clock lock
● ADC lock
○ Clock revert
○ Clock lock loss
○ Clock instability
○ ADC lock loss
○ 2.5V digital Vreg err
○ 3.3V digital Vreg err
○ 2.5V ADC Vreg err
○ 3.3V ADC Vreg err
L0 rate: 0
L0 count: 8425
L0 conf. count: 0
VCCINT: 0.993
VCCAUX: 2.490
VP/N: 0.218
FPGA temp: 39.1
Firmware: 78
Last SoR: 09/05/13-17:22:39

Clock select:
☑ Allow on-board ●
☑ Allow external ●
☐ Reset on PLL unlock ○
☐ Reset on instability ○

Resets:
☑ L0 rate reset ●
☐ After run start reset ○
L0 rate limit: 2000 2000
Rate resets since SoR: 0
L0 SoR limit: 0 0

Deserializer:
Pattern lock: ADC11 ☑ ☑ ☑ ☑ ☑ ☑ ☑ ☑ ☑ ☑ ☑ ☑ ADC00
Delay lock: ☑ ☑ ☑ ☑ ☑ ☑ ☑ ☑ ☑ ☑ ☑ ☑

	Data delay (set, applied)			Bitslip		Data delay (set, applied)			Bitslip
ADC00:	0	0	19	1	ADC06:	0	0	14	1
ADC01:	0	0	11	4	ADC07:	0	0	34	1
ADC02:	0	0	13	1	ADC08:	0	0	29	1
ADC03:	0	0	18	4	ADC09:	0	0	33	1
ADC04:	0	0	12	4	ADC10:	0	0	11	1
ADC05:	0	0	12	1	ADC11:	0	0	11	4

Trigger:
Trigger mode: ☑ 4x4 ● ☐ 2x2 ○
Trigger mode combination: ● OR ● ○ AND ○
Peak finder:
up: ☐ ☐ ☑ ☑ ☑ ☑ ☐
down: ☐ ☐ ☐ ☐ ☐ ☐ ☑
☐ ☐ ☑ ☑ ☑ ☑ ☐
☐ ☐ ☐ ☐ ☐ ☐ ☑

		~ GeV		~ GeV
4x4 threshold:	106	2.01	106	2.01
2x2 threshold:	527	10.00	527	10.00

Output mask: ☐ ☑ ☑ ☐ ☐ ☐ ☐ ☐ ☐ ☐ ☐ ☐ ☐ ☐ ☐ ☐
☐ ☑ ☑ ☐ ☐ ☐ ☐ ☐ ☐ ☐ ☐ ☐ ☐ ☐ ☐ ☐
L0 dead time: 200 200
L1 dead time: 8000 8000
GTL dead time: 80 80

Data:
Event width: 4 4
FALTRO rollback: 47 47
STU rollback: 39 39
STU L0 ID delta: 2 2
Data selector: ☑ Zero suppression ● ☐ STU pattern ○ ☑ STU transmit ON ●
Zsup threshold: 3 3
STU pattern: 0x0 ca3 0ca3
Multi-event buffer: ☑ ●

Timing:
ADC delta: 8 8
RCU phase: 0 0
RCU clk edge: ○ Positive ○ ● Negative ●

PEDESTAL data overrides:
Event width: 24
FALTRO rollback: 76
Data selector: ☐ Zero suppression
Zsup threshold: 0
PEDESTAL run type ONLY
PEDESTAL run type overrides

Test mode:
● No test mode ●
○ 0: L0 every N*25us ○
○ 1: L0 every N*25ns ○
○ 2: L0 receive, L0 send ○
○ 3: L0 loopback ○
○ 4: Count received L0s ○
○ 5: N L0s with 10Hz ○
Test mode data: 100 100
Test mode data 2: 0

Mass configuration:
☐ Clock select ☐ Reset enable ☐ L0 rate limit ☐ L0 SoR limit ☐ ADC ph. delta ☐ RCU phase&clk
☐ Trigger mode ☐ Peak finder ☐ 4x4 thresh ☐ 2x2 thresh ☐ Output mask ☐ Dead time ☐ GTL dead tim
☐ Event width ☐ FALTRO RB ☐ STU RB ☐ L0ID delta ☐ Data sel. ☐ Zsup thresh ☐ STU pattern ☐ MEB
☐ LED event width ☐ LED FALTRO RB ☐ LED data select ☐ Led zsup thresh
☐ Test mode ☐ Test mode data

Figure 4.26: Control panel for the TRU.

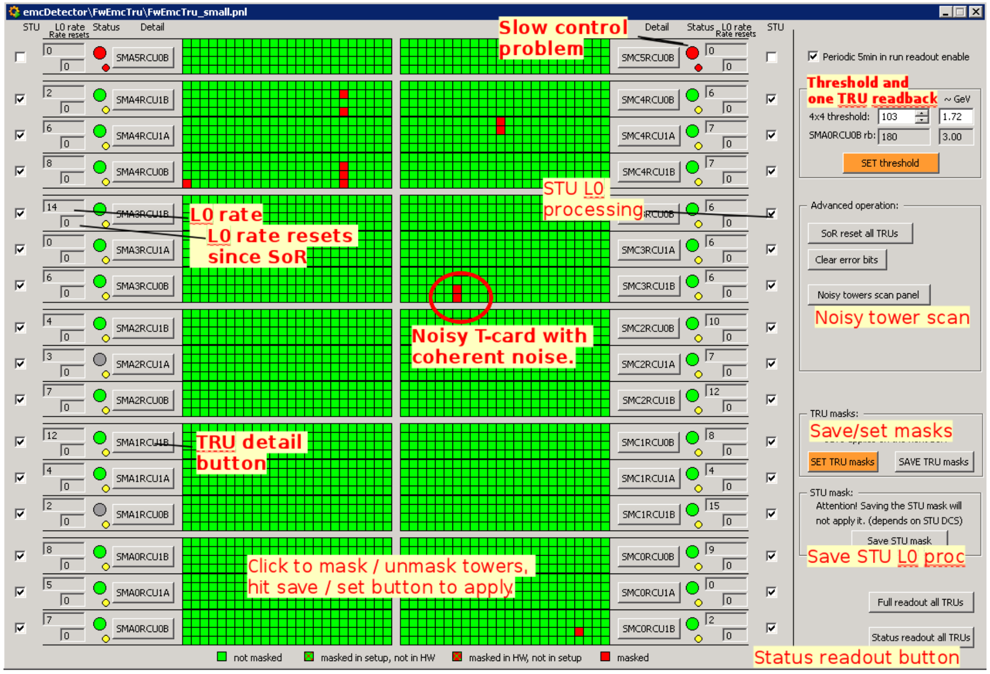

☑ Periodic 5min in run readout enable

4x4 threshold: 103 1.72

SMA0RCU0B rb: 180 3.00

Attention! Saving the STU mask will not apply it. (depends on STU DCS)

Figure 4.27: Overall control panel for the trigger.

4.7 Long term trigger operation

A commissioned trigger system requires an oversight during the operation periods. The main interest is quality of the trigger performance and functionality of the hardware.

4.7.1 Hardware operation

The hardware operation is monitored by the DCS, problems are reported to the operators who then contact EMCal experts. The general problems with trigger hardware are linked to overload of the voltage regulators on the TRUs. The DCS has alarms set to watch voltage values on the TRU board. In case of emerging problems, it is possible to replace the hardware ASAP before a total failure.

Another hardware operational problem can be a high level noise that is generated by a failing APD or a FEE card. TRU DCS monitors trigger rates and alerts operators in case of new noisy tower appearance (which happens relatively often).

Any change in a system interacting with the trigger must be monitored. Appropriate hardware commissioning must be re-run in case of need. For example, firmware upgrades of RCUs or STU can cause phase changes in propagating L0 messages. Replacements of FEE boards can lead to disconnected trigger signal cables, etc.

4.7.2 AMORE and DQM

ALICE framework offers possibility to connect online to the acquired data stream and process subset of events on the fly. The subset of events can then be displayed to detector experts via AMORE interface [148]. The interface is capable of producing plots from the supplied data and update them continuously. A larger set of trigger plots is defined, so that the trigger performance can be assessed fast during test running.

Another monitoring possibility is to define a subset of important plots that are to be reviewed periodically by ALICE shifters. The plots are displayed in the Data Quality Monitoring (DQM) interface (Fig. 4.28);

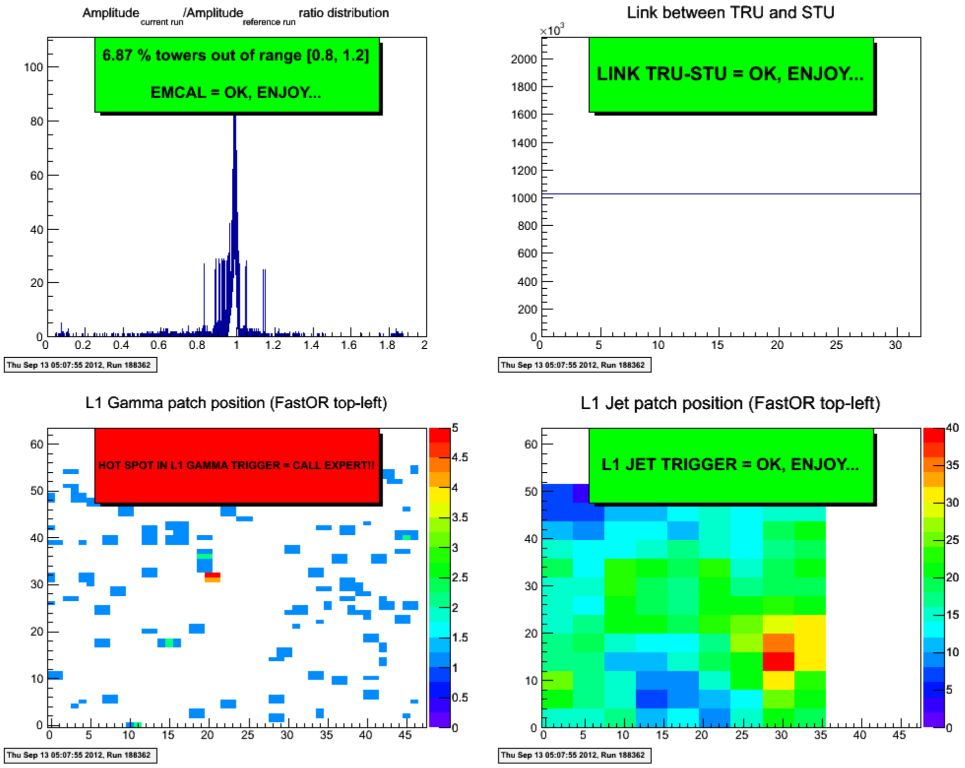

Figure 4.28: Part of the DQM display for EMCal. Monitoring TRU–STU link stability and L1 trigger production.

Chapter 5

Neutral pion analysis

The analysis aims to produce π^0 invariant yields in EMCal for PbPb collisions. The analysis was conducted together with and later completed by Dr. Astrid Morreale. The details on π^0 decay simulation and signal background subtraction are presented.

The analysis is presented for PbPb data set and was conceived to be complementary to already proceeding analysis in p–p data, which was carried out by different authors.

The EMCal detector had a functioning trigger during the PbPb run of 2011. For this reason it was expected that the p_{T} reach of obtained π^0 spectrum would be higher compared to momentum accessible in PHOS detector, which is better suited for the two photon invariant mass reconstruction thanks to its better granularity (roughly 3× smaller tower size) and better energy resolution.

5.1 π^0 reconstruction

The decayed π^0 were reconstructed using invariant mass method. The invariant mass of the pion is obtained from energies of two clusters hitting EMCal, E_1 and E_2, and their opening angle θ, Eq. (5.1).

$$M_{\gamma\gamma}^2 = 2E_1E_2(1-\cos\theta) \tag{5.1}$$

This method should guarantee a good identification of the π^0 up to transverse momentum (p_{T}) of ≈ 20 GeV/c, when the reconstruction efficiency drops rapidly due to finite resolution of the detector, depending on the decay asymmetry α

$$\alpha = \left|\frac{E_1-E_2}{E_1+E_2}\right| \tag{5.2}$$

where $E_{1,2}$ are the decay photon energies.

The analysis was conducted on minimum bias data samples, as well as on data triggered by the EMCal trigger.

5.1.1 EMCal resolution limit

Cluster merging becomes significant at some p_{T} level, which is dependent on the clustering algorithm used and detector granularity. The merging level starts around $p_{\mathrm{T}} \simeq 6$ GeV/c for the v1 clusterizer (3.3.1) and around $p_{\mathrm{T}} \simeq 20$ GeV/c for the v2. Reconstruction efficiency starts to drop rapidly and the invariant mass method becomes unsuitable. Shower shape analysis (3.3.3) is capable of identifying π^0 decay photons in the higher p_{T} regions.

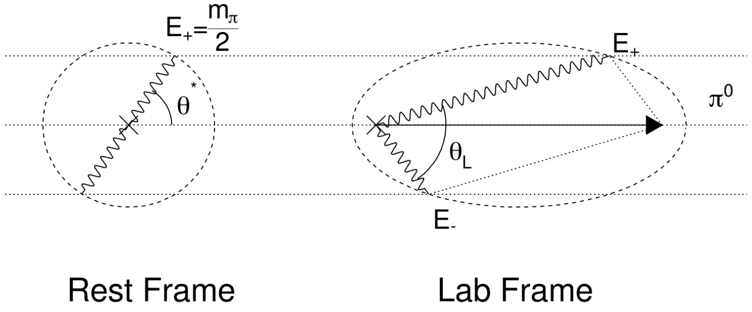

Figure 5.1: The $\pi^0 \to 2\gamma$ decay kinematics. The γ momenta were calculated for $E_{\pi^0} = 250$ MeV.

To get the basic idea about the region where the reconstruction efficiency starts to drop, one can derive analytically $\mathrm{d}N_{\pi^0}/\mathrm{d}\theta$ distribution using the fact that the decay photon pairs from the unbiased π^0 decay have uniform α distribution. Assuming the isotropic back-to-back γ decay in the rest frame of π^0 and boosting the decay photons into laboratory frame (Fig. 5.1) one can show that the 2γ opening angle in the laboratory frame, θ_L, can be expressed as

$$\cos\theta_L = \frac{\gamma^2(1-\alpha^2)-2}{\gamma^2(1-\alpha^2)} = \frac{\gamma^2(\beta^2-\alpha^2)-1}{\gamma^2(1-\alpha^2)} = \frac{E_{\pi^0}^2(1-\alpha^2)-2m_{\pi^0}^2}{E_{\pi^0}^2(1-\alpha^2)} \tag{5.3}$$

where E_{π^0} and m_{π^0} are π^0 energy and mass. Then

$$\begin{aligned} \frac{\mathrm{d}N_{\gamma\gamma}}{\mathrm{d}\alpha} &= \frac{\mathrm{d}N_{\gamma\gamma}}{\mathrm{d}\theta_{\mathrm{L}}}\frac{\mathrm{d}\theta_{\mathrm{L}}}{\mathrm{d}\alpha} = \text{const} \Rightarrow \\ \Rightarrow \frac{\mathrm{d}N_{\gamma\gamma}}{\mathrm{d}\theta_{\mathrm{L}}} &\propto \frac{\mathrm{d}\alpha}{\mathrm{d}\theta_{\mathrm{L}}} \end{aligned}$$

and thus

$$\frac{\mathrm{d}N_{\gamma\gamma}}{\mathrm{d}\theta_{\mathrm{L}}} \propto \frac{m_{\pi^0}^2(1+\cos\theta_{\mathrm{L}})}{E_{\pi^0}^2 \sin\theta_{\mathrm{L}}\sqrt{1-\cos\theta_{\mathrm{L}}}\sqrt{1-\cos\theta_{\mathrm{L}}-\frac{2m_{\pi^0}^2}{E_{\pi^0}^2}}} \approx \frac{m_{\pi^0}^2}{E_{\pi^0}^2\sin\theta_{\mathrm{L}}}\frac{1+\cos\theta_{\mathrm{L}}}{1-\cos\theta_{\mathrm{L}}} \tag{5.4}$$

Another way how to obtain a $\mathrm{d}N/\mathrm{d}\theta_{\mathrm{L}}$ distribution is to extract an angle θ_{L} from Eq. (5.3) and perform a random sampling using a flat α distribution. The comparison of Eq. (5.4) with the monte carlo simulation where the decay photons from π^0 of different p_{T} are boosted and the opening angle distribution is calculated is shown on Fig. 5.2. Fig. 5.3 shows the analytic formula and MC simulation compared with data.

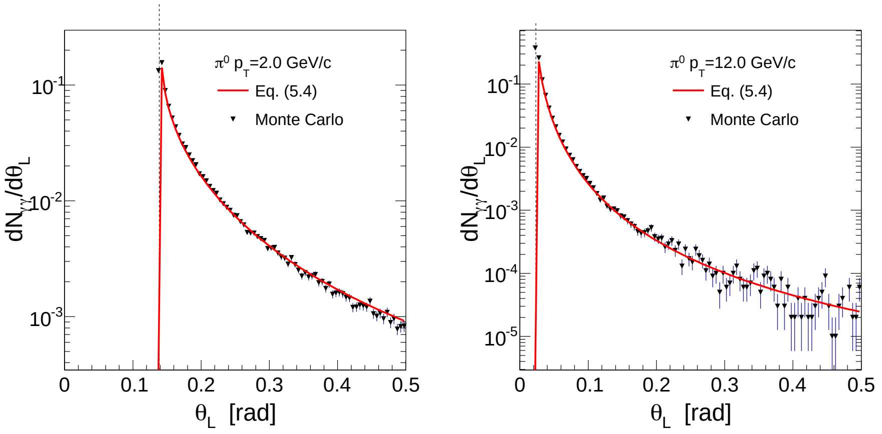

Figure 5.2: An opening angle distributions from the π^0 decay in mid-rapidity of $p_{\mathrm{T}\pi^0}$ = 2 GeV/c (left) and $p_{\mathrm{T}\pi}$ = 12 GeV/c (right). The solid red lines represent Eq. (5.4) and the data points represent the results of the simple Monte Carlo simulations. The vertical dashed line represents the minimum opening angle Eq. (5.5)

There is a minimum of the $\theta_{\mathrm{L,min}}$ for a given $p_{\mathrm{T}\pi^0}$. The minimum angle is reached when the decay photons are emitted perpendicularly with respect to the π^0 momentum. In this case the asymmetry $\alpha = 0$. From Eq. (5.3) with $\alpha = 0$ one sees

$$\theta_{\mathrm{L,min}} = \arccos\left(\frac{E_{\pi^0}^2 - 2m_{\pi}^2}{E_{\pi^0}^2}\right) = \arccos\left(\frac{p_{\mathrm{T}\pi^0}^2 - m_{\pi^0}^2}{p_{\mathrm{T}\pi^0}^2 + m_{\pi^0}^2}\right) \tag{5.5}$$

The EMCal geometry (tower size, one cell is 0.83 degrees) and the clusterizer algorithm determine the minimal angular distance, $\Delta\theta_{\mathrm{min}}$, when the two photon hits can be resolved. This also determines the π^0 transverse momentum region where the two photon invariant mass method can be used. The π^0 reconstruction efficiency, $\varepsilon_{\gamma\gamma}(p_{\mathrm{T}\pi^0})$, can be calculated as

$$\varepsilon_{\gamma\gamma}(p_{\mathrm{T}\pi}) = \int_{\Delta\theta_{\mathrm{min}}}^{\pi^0} \frac{\mathrm{d}N_{\gamma\gamma}}{\mathrm{d}\theta_L}\mathrm{d}\theta_L \cdot \left(\int_0^{\pi^0} \frac{\mathrm{d}N_{\gamma\gamma}}{\mathrm{d}\theta_L}\mathrm{d}\theta_L\right)^{-1} \tag{5.6}$$

where $\mathrm{d}N_{\gamma\gamma}/\mathrm{d}\theta_L$ is taken from Eq. (5.4). Results of numerical integration of Eq. (5.6) for v2 and v1 clusterizers with $\Delta\theta_{\mathrm{min}} = 0.04$ and $\Delta\theta_{\mathrm{min}} = 0.014$ radians are shown on Fig. 5.4.

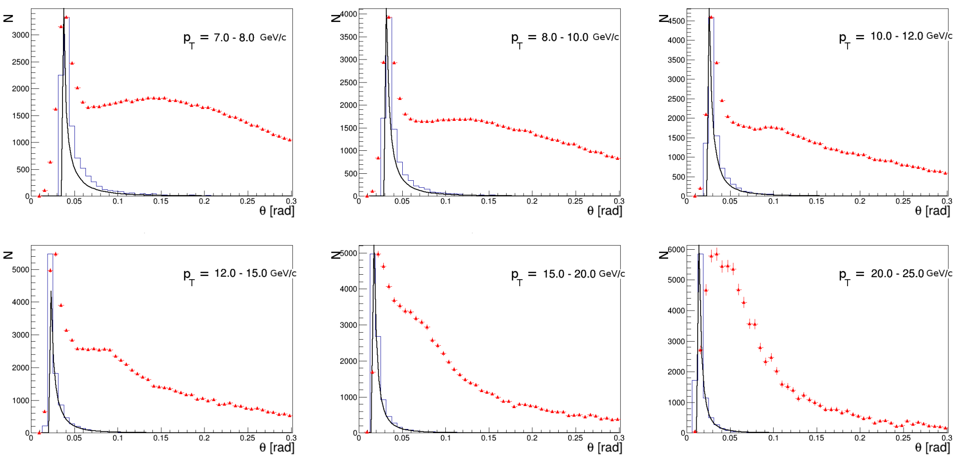

Figure 5.3: θ distribution comparison of data (red), MC sample from Eq. (5.3) (blue) and analytic form Eq. (5.4) (black), for various p_{T} bins and v2 clusterizer. The cluster merging starts to eliminate the π^0 signal at around 20 GeV/c. Arbitrary normalization. The yield in high-mass region comes from combinatorial background. It can be seen that for higher p_{T} bins the data suffers from the resolution limit and degraded reconstruction efficiency.

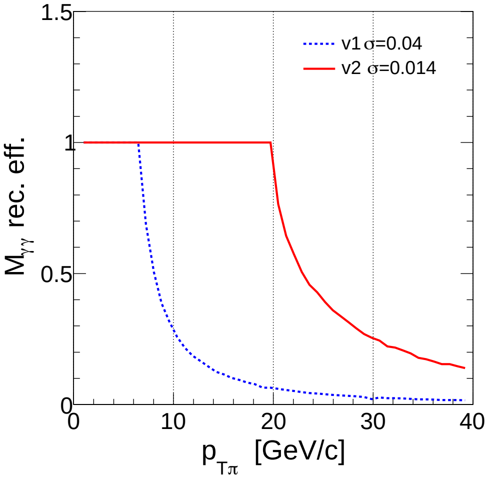

Figure 5.4: The π^0 reconstruction efficiency from $M_{\gamma\gamma}$ method for two different angular resolutions $\Delta\theta_{\mathrm{min}} = 0.04$ (v1 clusterizer) and $\Delta\theta_{\mathrm{min}}$=0.014 (v2 clusterizer). The efficiency $\varepsilon_{\gamma\gamma}(p_{\mathrm{T}\pi^0})$ starts to drop around $p_{\mathrm{T}\pi^0} \sim 6$ GeV/c for v1 and $p_{\mathrm{T}\pi^0} \sim 20$ GeV/c for v2 clusterization algorithm.

The efficiency $\varepsilon_{\gamma\gamma}(p_{\mathrm{T}\pi^0})$ starts to drop around $p_{\mathrm{T}\pi^0} \sim 6$ GeV/c for v1 and $p_{\mathrm{T}\pi^0} \sim 20$ GeV/c for v2 clusterization algorithm.

Another important observation is that the efficiency drops quite sharply near the edge ($p_{T,\max}$). It means that one can estimate the π^0 p_{T} reach for given angular resolution (given by hardware and clusterizer method) by inversion of Eq. (5.5)

$$p_{T,\max} = m_\pi \sqrt{\frac{1+\cos\theta_{L,\min}}{1-\cos\theta_{L,\min}}} \approx m_\pi \sqrt{\frac{4}{\theta^2_{L,\min}} - 1} \approx \frac{2\,m_\pi}{\theta_{L,\min}} \tag{5.7}$$

where we use a Taylor expansion of $\cos x = 1 - x^2/2 + \mathcal{O}(x^4)$ and assume $\theta_{L,\min} \ll 1$. However, the last approximation in Eq. (5.7) holds so well that e.g. for largest angle $\theta_{L,\min} = 0.04$ rad the approximation (last term of Eq. (5.7)) differs from the exact solution (first term of Eq. (5.7)) by less then 10^{-3} %.

Aside of the limits of the π^0 signal resolution, it is also useful to know, what minimal $M_{\gamma\gamma}$ coming from combinatorial background will be available in the invariant mass distribution for various γ pair p_{T}. For extracting the invariant mass yields, it is useful to be able to fix fits of remaining background in both lower and higher $m_{\gamma\gamma}$ areas around m_{π^0}. The Eq. (5.3) can be adapted to become function of $m_{\gamma\gamma}$, instead of a constant m_{π^0}, and α can be set to a constant. One can study then the minimal $m_{\gamma\gamma}$ available (Fig. 5.5). Knowing the detector granularity and a clustering algorithm used, one can deduce a minimum separation of two clusters. In case of EMCal and v2 clusterizer (requires once cell of local minimum to separate two clusters), it is safe to presume that the minimal separation is slightly above 1.5 of a cell width.

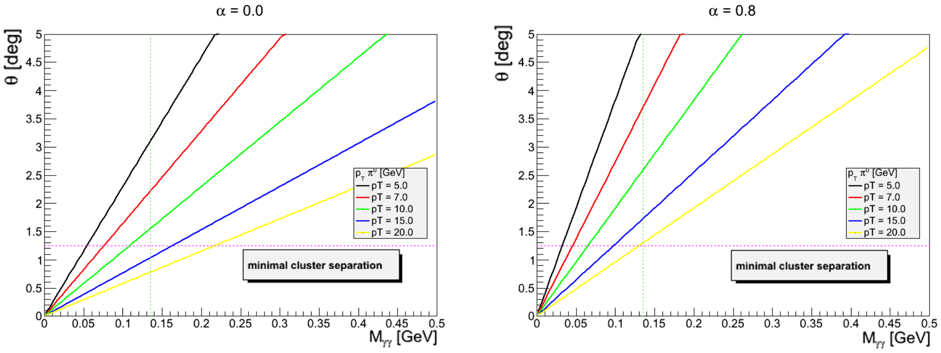

Figure 5.5: Mutual dependence of θ and $m_{\gamma\gamma}$ for two fixed α (0 left, 0.8 right) and multiple $p_{\mathrm{T},\gamma\gamma}$. The minimal cluster separation line (horizontal) is set to dimension of 1.5 cell. Vertical line highlights the π^0 mass. The $m_{\gamma\gamma}$ values below the separation line (where the diagonal lines cross below the horizontal threshold) will not be available in the $M_{\gamma\gamma}$ distribution for a given $p_{\mathrm{T},\gamma\gamma}$ and asymmetry.

5.2 π^0 invariant mass distribution

The target of the analysis was to use the invariant mass distribution to obtain fully corrected π^0 yields in the PbPb collisions.

The invariant mass signal of the decaying π^0 is superposed on uncorrelated and correlated background. The uncorrelated background arises from combining physically uncorrelated (random) pairs of EMCal hits. Physically correlated pairs comes from genuine π^0 decays, photon converting into electron–positron pair when passing through material (conversions) or localized production of particles in space (jets).

The π^0 pairs must be separated from all other sources. The main problem to be solved was the subtraction of the correlated background. After subtraction of the uncorrelated background with event mixing method (5.2.2), there was a residual correlated background left below the signal. Due to the minimum $m_{\gamma\gamma}$ limits discussed in the previous section (5.1.1) there is not enough of low mass signal to constrain the fit function needed to interpolate the residual background below the π^0 signal peak. Understanding the shape of the residual background below the signal peak would decrease significantly systematic error of the signal extraction.

5.2.1 EMCal clustering

The clusters used in analysis were obtained from EMCal by the v2 clusterizer. Clusters matched to charged tracks were removed from the analysis, as well as all clusters being identified as fake (exotic, see 3.3.2). Fiducial cut of 1 tower size was applied to the super module edges (except the mid–rapidity edge). Table 5.1 summarizes the v2-clusterizer parameteres and cuts used in this analysis.

Clusterizer seed	0.2 MeV
Clusterizer cutoff	0.05 MeV
Cells in cluster	> 1
Track matching radii	0.025
Fiducial cut	1 tower
Exotic cut	0.97
Minimal cluster E	0.3 GeV
Maximum pair asymmetry	0.8
Consider only pairs in similar SM	yes

Table 5.1: Clusterizer parameteres and cuts.

A check for correlated hot towers was performed by means of displaying a spatial distribution of the cluster pairs (Fig. 5.6). The SM borders, structure of ALICE space frame and TRD is very well visible (lower intensity regions).

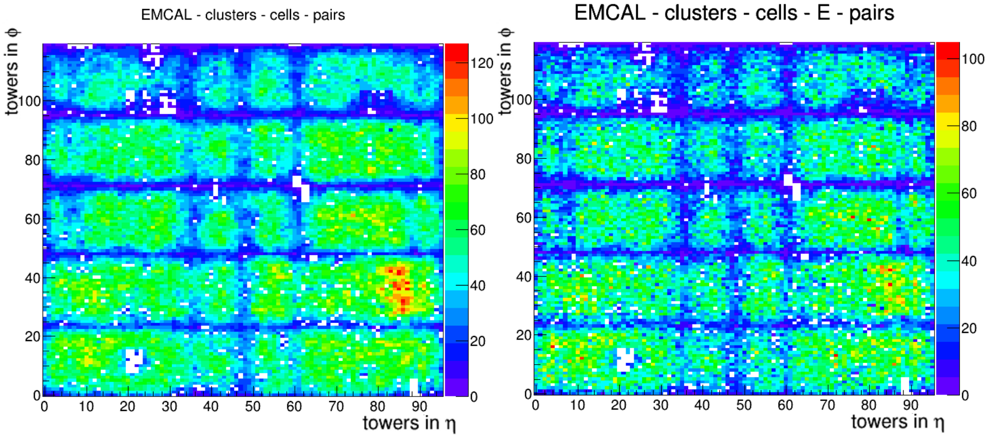

Figure 5.6: Left: Spatial distribution of towers in cluster pairs in EMCal. Right: Spatial distribution if integrated energy deposit of towers in cluster pairs.

5.2.2 Event mixing

The uncorrelated background can be subtracted with use of mixed-event invariant mass distribution. Combining the EMCal hits from different events removes any physical correlations between the photons and thus the invariant mass distributions should be able to describe the combinatorial background. There are some limitations coming e.g. from the residual correlation induced by elliptic flow or high-p_{T} jets.

In order to ensure that similar events are used for mixing, the maximum allowed difference in centrality is $\pm$ 10%, vertex position $\pm$ 5 cm and multiplicity $\pm$ 1000 charged tracks. An example of an event mixing distribution is shown on Fig. 5.7. The normalization of the event mixing distribution is obtained by adjusting the spectra at the high mass tail, well above the mass of the η meson (548 MeV/c^2). It can be seen from the figure that the uncorrelated background does not account for all the background below the signal.

The event mixing pool can be filled with triggered or minimum bias (MB) events and mixed with triggered or minimum bias events. It is always desired to mix only minimum bias events to avoid trigger to affect the resulting spectra. It may be interesting to examine an option to use triggered event for mixing due to the low statistics of minimum bias data set. Results of mixing of triggered events pool with triggered events, MB pool with triggered events and MB pool with MB events were compared. There is no significant difference in background shape in between the three methods for $p_{\mathrm{T}} > 7$ GeV/c. There is a lower background estimate in case of pure MB-MB mixing in respect to mixing triggered events with either triggered or MB pool in the lower p_{T} range (Fig. 5.8). The use of triggered data sample event mixing can be considered safe for $p_{\mathrm{T}} > 7$ GeV/c.

The remaining background below the π^0peak on Fig. 5.8 comes from correlated $\gamma\gamma$

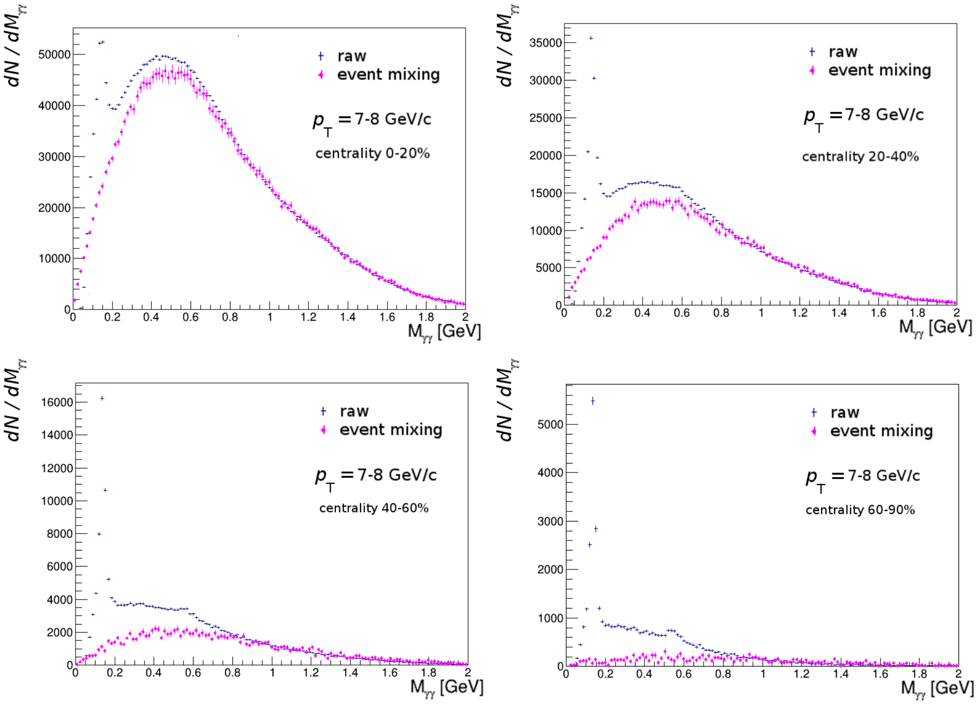

Figure 5.7: Example of raw (blue) and event mixing (magenta) invariant mass distribution for centrality bins 0-20-40-60-90%, for one selected p_T bin. The event mixing uncorrelated background does not account for the full background below the signal.

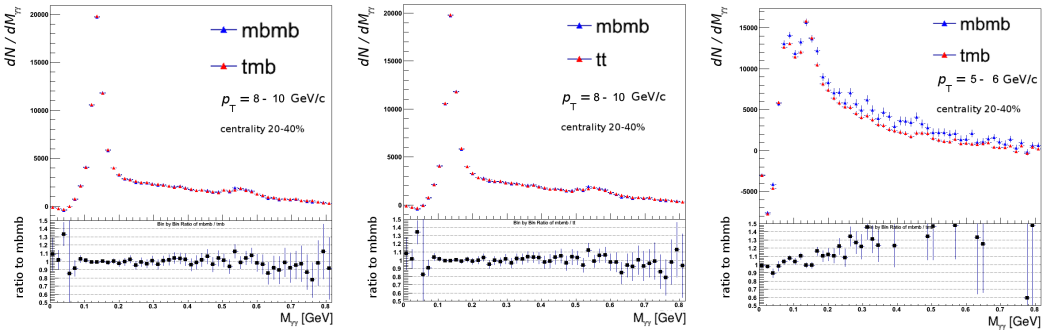

Figure 5.8: Invariant mass distribution with background subtracted by the event mixing method. The left plot shows comparison of pure MB event mixing with MB pool and triggered event mix. The middle plot shows MB-MB and triggered-triggered comparison. The right plot shows the same comparison for lower p_T bin (5-6 GeV), where a discrepancy in between pure MB and other methods shows up.

pairs. The undershoot of the distribution in low mass region on the same figure is caused by the fact, that in event mixing it is possible to combine two clusters topologically very close or even overlapping, which would normally merge in a single event due to limited calorimeter resolution (5.1.1). Combining very close hits then creates a lower mass enhancement of mixed signal.

5.2.3 Correlated background

There is a residual background in the invariant mass distribution after event mixing subtraction (see Fig. 5.8). Also, the calorimeter resolution does not allow to reconstruct photon pairs with invariant mass much below the peak, so it is uneasy to constraint a fit of the residual background. An attempt was made to understand the source of the remaining background in order to be able to constraint its shape below the signal peak.

It was examined first how big fraction of the residual background could be coming from photon conversions. A simple toy monte-carlo simulation was developed to study mass distribution from conversion. The material budget in front of EMCal is about 0.3 radiation lengtsh (X_0), where the major contribution comes from the TRD structure.

The toy MC simulated pion spectrum and decay. We used 50% conversion probability for the decay photons. The mass spectrum from the simulated conversions was found to reproduce the residual background very well. Due to the nature of the simple toy MC, it was not possible to simply simulate the finite detector resolution and cluster merging, so the background reaches to lower invariant masses and causes over subtraction (Fig. 5.9).

5.2.4 Signal fit

The remaining signal was fit with asymmetric gaussian + linear function Eq. (5.8).

$$f(x) = A \cdot \begin{cases} \exp\left(-\frac{(x-x_0)^2}{2\sigma^2}\right) & x > x_0 \\ \exp\left(-\frac{(x-x_0)^2}{2\sigma^2 r^2}\right) & x \leq x_0 \end{cases} \tag{5.8}$$

where x_0 is peak position of the Gaussian and r is asymmetry variable. The results of the fit are shown on Fig. 5.10 and on Fig. 5.11 for the case when undershoot correction is utilized, as discussed in 5.2.5. The extracted π^0 invariant mass and its width are shown on Fig. 5.12.

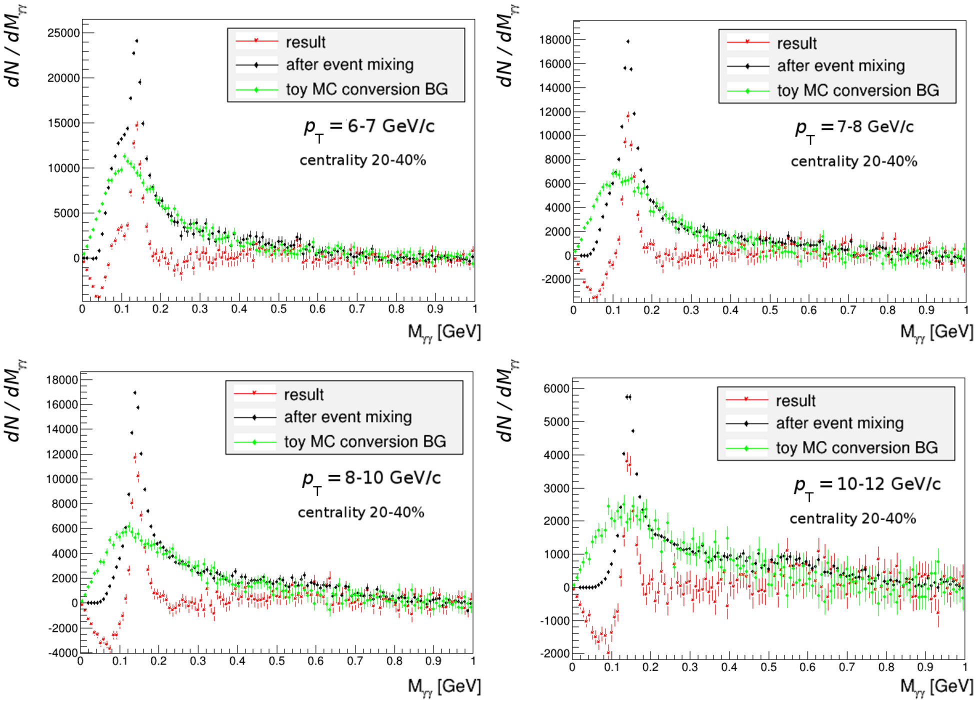

Figure 5.9: Event mixing subtracted invariant mass distribution with toy MC simulation of the residual correlated background. For selected centrality bin and several p_{T} bins. The black points represent the data invariant mass distribution for 20-40% centrality and various pair p_{T}. The green points represent the monte carlo simulated conversion spectrum. The red points (labeled as "result") shows the spectrum after the conversion contrib is subtracted. The conversion simulation doesn't take into account the double hit resolution which causes the overestimation of the conversion contrib in the low mass region. Consequently the resulting spectrum is over subtracted in this low mass region.

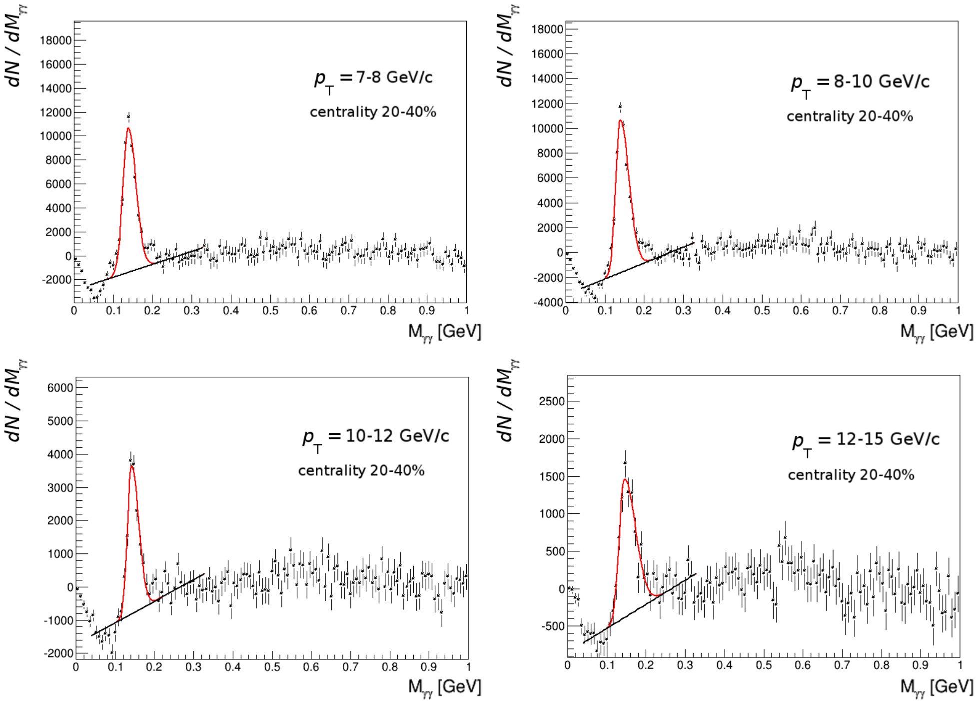

Figure 5.10: Signal fit examples with Eg. 5.8. for 20-40% centrality and p_{T} bins 7-8-10-12-15 GeV/c. The conversion contribution simulated by the toy MC is subtracted.

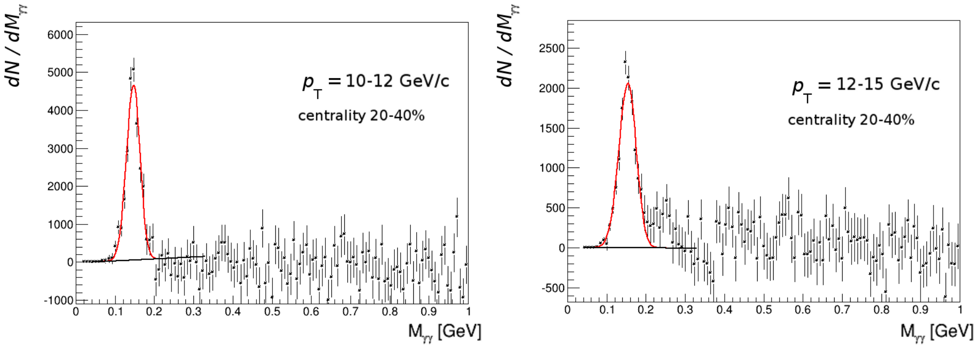

Figure 5.11: Signal fit examples with Eg. 5.8. for 20-40% centrality and p_{T} bins 10-12-15 GeV/c. The conversion contribution simulated by the toy MC is subtracted. Undershoot correction on event mixing and MC simulation is utilized, as discussed in 5.2.5

.

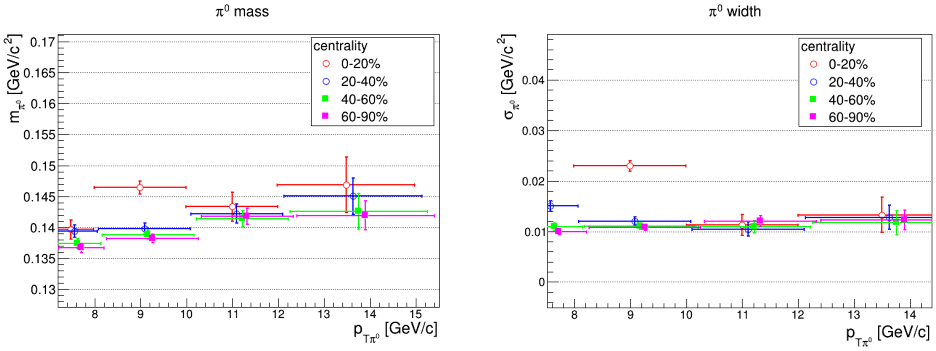

Figure 5.12: Extracted π^0 mass peak position and mass peak widths as a function of the π^0 transverse momentum. The outlier point for 0-20% centrality comes from a failing fit.

5.2.5 Undershoot correction

Subtraction of event mixing and correlated background suffers from missing finite detector granularity and cluster merging. The low invariant mass part of the background distribution is enhanced in respect to signal. The background subtraction results in an undershoot in the low mass region (ass seen on Fig. 5.9 or 5.10) and possibly also an underestimate of the π^0 yield.

An attempt was made to correct the undershoot from the background subtraction. A full ALICE monte-carlo was used to obtain an efficiency of pair reconstruction as a function of the pair mass. In the low mass regions, the efficiency should be decreased by cluster merging. In the higher mass region the efficiency is expected to be decreased by geometry (a photon escaping acceptance).

Photon pairs originating close to interaction point were selected and checked for efficiency of each of them producing a separate cluster. The result from the MC is shown on Fig. 5.13. The intention was to understand only the low mass inefficiency, hence a maximum for each curve was normalized to 1 and only the low mass part of the curve was considered. The magenta Fig. 5.14 show how an event mixed background shape is altered when the two cluster resolution efficiency is applied during the mixing. The resolution efficiency was used to correct the undershoot that arises from mixed event and toy MC background subtraction.

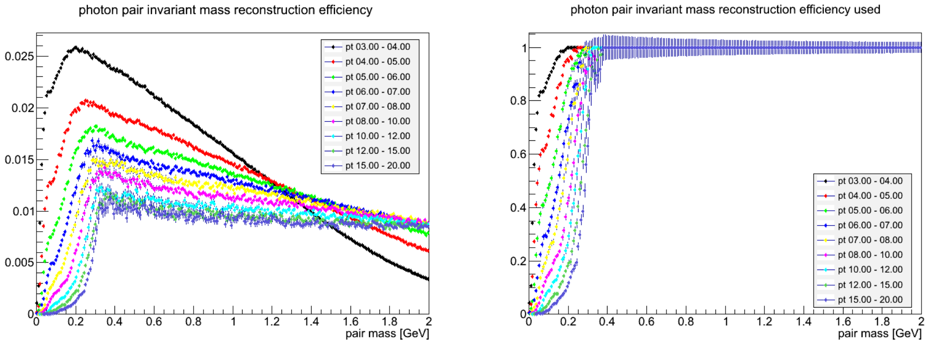

Figure 5.13: Efficiency of photon pair invariant mass reconstruction for different p_{T} bins. The right plot shows all curves normalized to maximum at 1 and geometry effect in the high mass region removed.

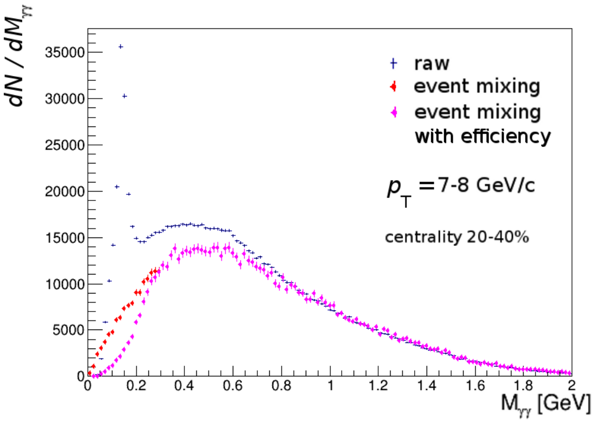

Figure 5.14: Example of raw (blue) and event mixing (red) and event mixing with two cluster resolution efficiency applied (magenta) invariant mass distribution for centrality bins 20-40% and p_{T} bin 7-8 GeV/c. The difference in between magenta and red points is the effect of the two cluster resolution efficiency application.

5.2.6 Invariant yields

The resulting π^0 invariant yields in ALICE Pb–Pb collisions are shown on Fig. 5.15 for minimum bias and for the EMCal triggered data set. Further steps of the analysis are described in ALICE note [149].

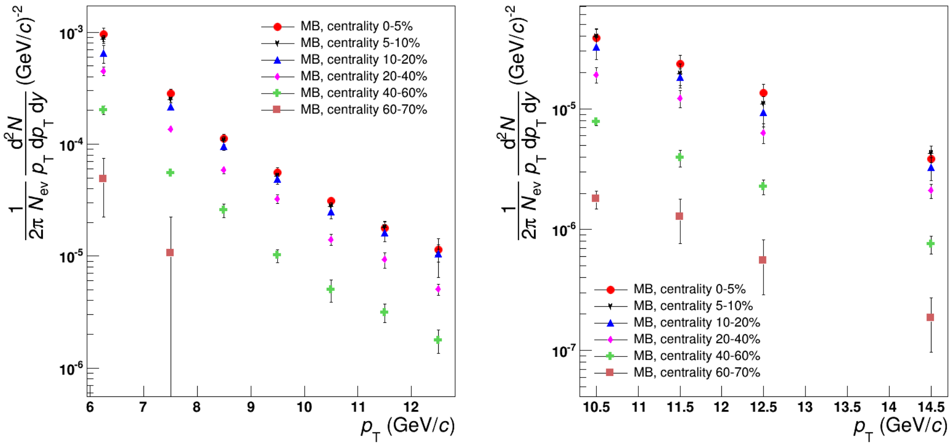

Figure 5.15: Invariant π^0 yields for minimum bias (left) and EMCal triggered (right) data sets. The yields are presented in centrality bins 0-5-10-20-40-60-80%.

5.3 Results

There are various methods with which the invariant π^0 yields can be reconstructed in ALICE [150, 151]. Invariant mass of a photon pair can be reconstructed directly in both calorimeters PHOS and EMCal. It is also possible to reconstruct the invariant mass indirectly, via Photon Conversion Method (PCM). The PCM uses charged tracks of electrons that come from photons converted in the inner volume of ALICE.

Comparison of results from EMCal and a combined results from PHOS and PCM methods is shown on Fig. 5.16. The results from EMCal do fit well the already published points [150] from the so far finished analysis.

5.4 Results from π^0 analysis from the LHC

The π^0 yields resulting from the EMCal analysis was compared to results from an analysis of PHOS data [131] and Photon Conversion Method (PCM) [150, 151]. All three different analyses were found in a good agreement but because of better understanding of PHOS and PCM systematics the EMCal results are not presented in [150] but it is being prepare for publication in the near future.

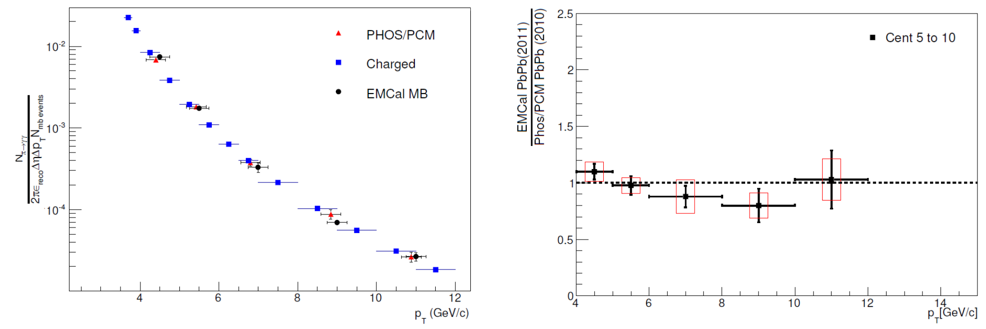

Figure 5.16: Invariant π^0 yields from EMCal compared to yields from combined PHOS and PCM analysis [150] and to $\pi^{\pm}$ yields. Displayed points are for PbPb collisions $\sqrt{s_{\mathrm{NN}}} = 2.76$ TeV and centrality bin 5-10%.

There are two major results of the π^0 yield analysis: (i) π^0 spectrum measured in pp collisions [151] and (ii) π^0 nuclear modification factor R_{AA} measured in $\sqrt{s_{\mathrm{NN}}} = 2.76$ TeV Pb–Pb data [150].

5.4.1 The π^0 yield in $\sqrt{s} = 0.9$ and 7 TeV pp data.

The π^0 transverse momentum distribution measured by PHENIX [152] was a landmark in the success of NLO description of the data from RHIC. Better than ~30% agreement between the NLO and the data (Fig. 5.17(a)) was observed. Therefore, it comes as s surprise that the comparison of charged hadron and π^0 yields to NLO at $\sqrt{s} = 0.9$ and 7 TeV pp data reveals a discrepancies by factor of 2 to 3 (Fig. 5.17(b)). Furthermore, the discrepancy seems to be worse at $\sqrt{s} = 7$ than at $\sqrt{s} = 0.9$ TeV.

It was pointed out by Eskola and his collaborators [153] that due to the fact that the charged hadron and π^0 production from the hard scattering at LHC is dominated by the gluon fragmentation the measured spectrum can be used to constraint the gluon-to-pion fragmentation function. The main result of this analysis is shown on Fig. 5.18 where the better agreement between the data and NLO is reached by use of improved fragmentation function set.

5.4.2 The nuclear modification factor R_{AA} at $\sqrt{s_{\mathrm{NN}}} = 2.76$ TeV

The nuclear modification factor is defined as Eq. (1.13). The centrality and p_{T} dependencies are sensitive to jet-quenching phenomenon discuss in section 1.2.2. and the first measurement of R_{AA} at $\sqrt{s_{\mathrm{NN}}} = 130$ GeV at RHIC was considered as a unambiguous manifestation of the deconfined nuclear medium in URHI collisions [52, 154]. Nowadays, the large suppression of high-p_{T} particles and jets is relatively well understood in terms of weak coupling (pQCD approach assuming $\alpha_S \ll 1$) [54–59] and

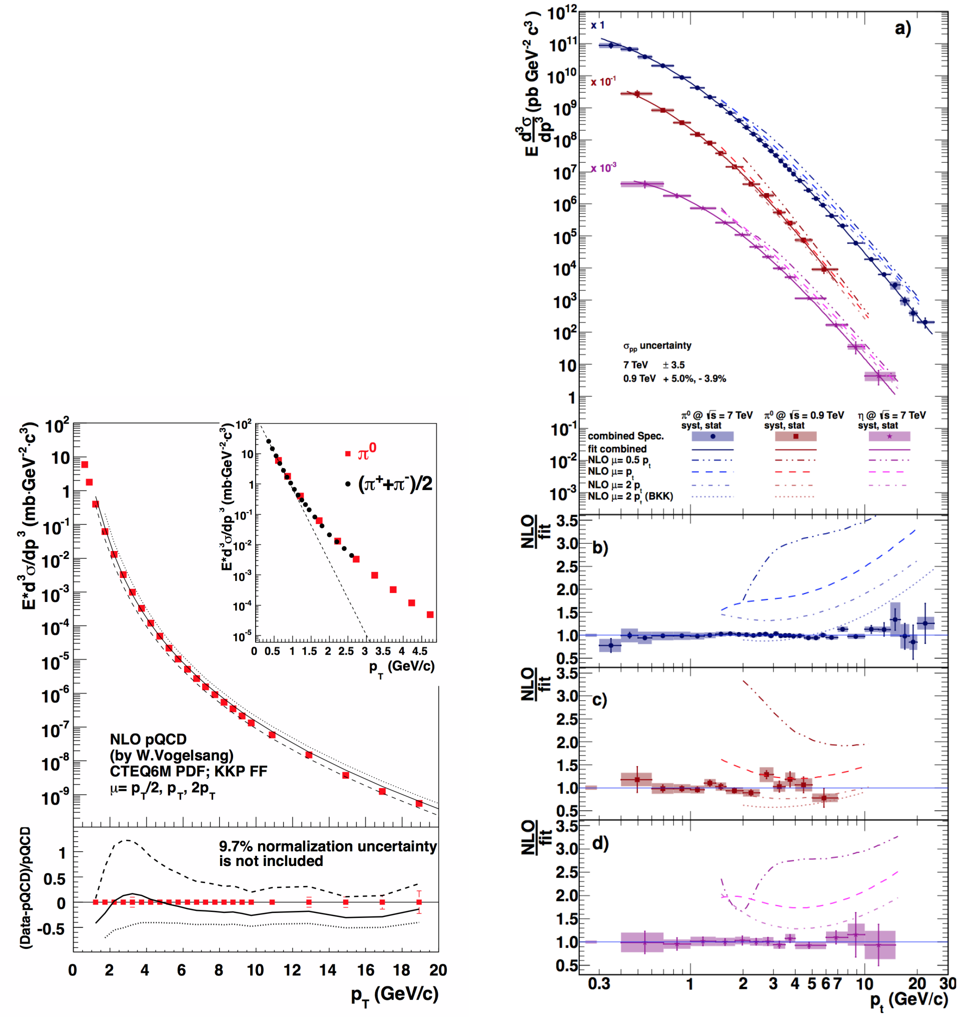

(a) PHENIX

(b) ALICE

Figure 5.17: (a) The neutral pion production cross section at $\sqrt{s_{\rm NN}} = 200$ GeV from PHENIX [152] compared to NLO pQCD calculations. (b) Differential invariant cross section of π^0 and η production in pp collisions at $\sqrt{s} = 7$ TeV (circles) and 0.9 TeV (squares) by ALICE [151].

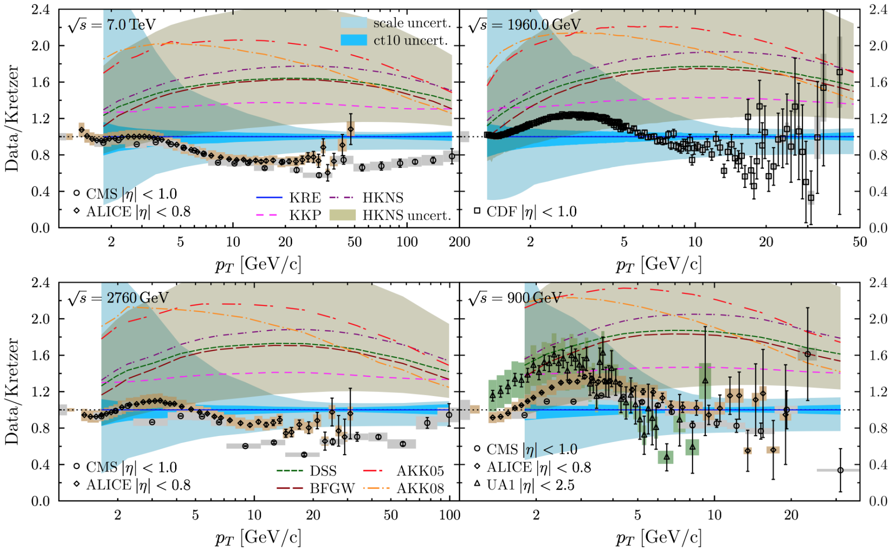

Figure 5.18: Ratio of the inclusive charged-hadron spectra measured by CMS (circles), ALICE, (diamonds), CDF (squares), and UA1 (triangles), see [153] and refences herein, over the corresponding NLO calculations using various fragmentation function sets.

strong coupling (exploiting the AdS/CFT duality) models [155–161].

The R_{AA} measurements for neutral (Fig. 5.19) and charged pions [167] agree with each other over the entire p_{T} range for all centrality classes. However, the neutral pion agrees with the charged particle R_{AA} [168] only in $p_{\mathrm{T}} \gtrsim 6$ GeV/c region indicating the anomalous proton production in central Pb-Pb collisions.

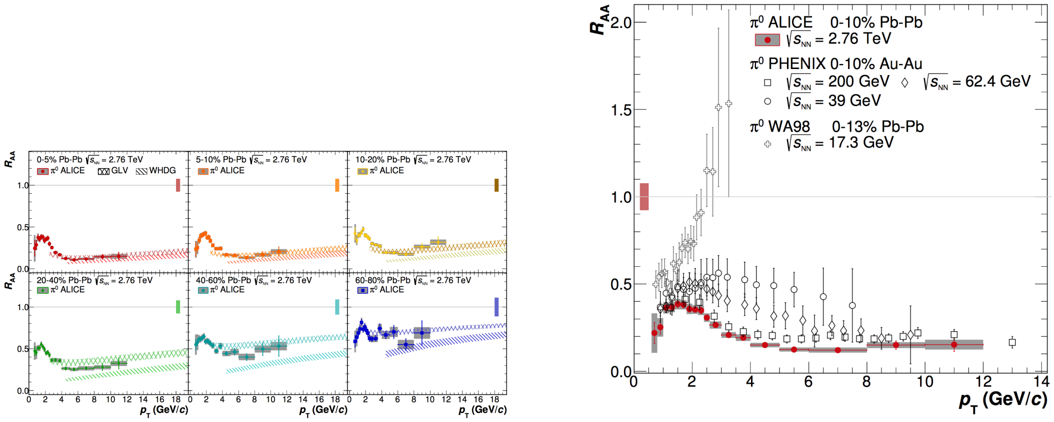
(a)

(b)

Figure 5.19: (a) Comparison of the measured nuclear modification factor R_{AA} with a GLV calculation [162, 163] and with a WHDG [59] parton energy loss calculations. (b) Neutral pion nuclear modification factor in Pb–Pb collisions at $\sqrt{s_{\mathrm{NN}}} = 2.76$ TeV for the 0-10% class in comparison with results from Au–Au collisions at $\sqrt{s_{\mathrm{NN}}} = 39$, 62.4 [164], and 200 GeV [165] as well as the result from the CERN SPS [166].

Chapter 6

Jet fragmentation transverse momentum distribution in p–Pb $\sqrt{s_{\mathrm{NN}}} = 5.02$ TeV data

Jets are the clusters of collimated particles originating from the fragmentation of hard scattered partons (see 1.3.4 for more details). The final state particles are collimated to cones around axis that is given by the scattered parton momentum. Jet properties are influenced by both perturbative and non-perturbative processes that take place during the jet fragmentation. In this way the reconstructed particles can still be mapped to some extent to the colored objects that originate from parton showering (1.3.5).

In this chapter the jet-fragmentation transverse momentum j_{T} is analyzed. The $\mathrm{d}N/\mathrm{d}j_{\mathrm{T}}$ distributions in jets provide insight into the gluon radiation patterns in jet fragmentation. The j_{T} distribution was studied at ISR [169] and RHIC [170] using the dihadron correlation technique. Here I exploited the fully reconstructed jets in p–Pb $\sqrt{s_{\mathrm{NN}}} = 5.02$ TeV data and analyzed the j_{T} momentum measure with respect to jet axis. The $\mathrm{d}N/\mathrm{d}j_{\mathrm{T}}$ distributions with respect to jet axis were first measured at TEVATRON [100] and found to be in a good agreement with Next-to-Modified Leading Log Approximation (NMLLA) [102].

This chapter discusses basics of the analysis method. The detail overview of the analysis is available in ALICE analysis note [171].

6.1 Data, trigger and event selection

The ALICE experiment collected a substantial data set of p–A collisions both with minimum bias and dedicated electromagnetic calorimeter jet trigger. The data periods are labeled LHC13 b,c,d,e and contain ≈ 116 Mevents of minimum bias and 3 Mevents of jet triggered interactions in good quality runs.

The EMCal trigger was operational for the p–A data taking period. Aside of single photon triggers, two jet trigger thresholds were utilized; 10 GeV and 20 GeV. The trigger algorithm was using 32×32 cells patch size, sliding by 8 cells (see 4.3.3). The trigger operates on level-1 and requires preceding level-0 which must be in coincidence with the interaction trigger. The level-0 trigger is a standard 4×4 sliding window in exclusive 8×24 towers areas (see 4.3.2). Threshold of the L0 trigger was set to 3 GeV.

Events are selected primarily according to the active triggers (interaction or jet trigger). Additionally number of tracks participating to vertex, vertex z coordinate and SPD and TPC vertex deviation are used to select events with proper vertex. Pile-up events with multiple vertexes are rejected.

6.2 Jet reconstruction

6.2.1 Charged tracks and EM clusters

The tracks are selected based on combined TPC and ITS information. Due to missing regions in ITS (dead modules in one layer of the SPD), the track cuts are released for the ITS to allow accepting tracks from regions with the missing ITS information (Fig. 6.1). The tracks with released cuts complement the higher quality ones.

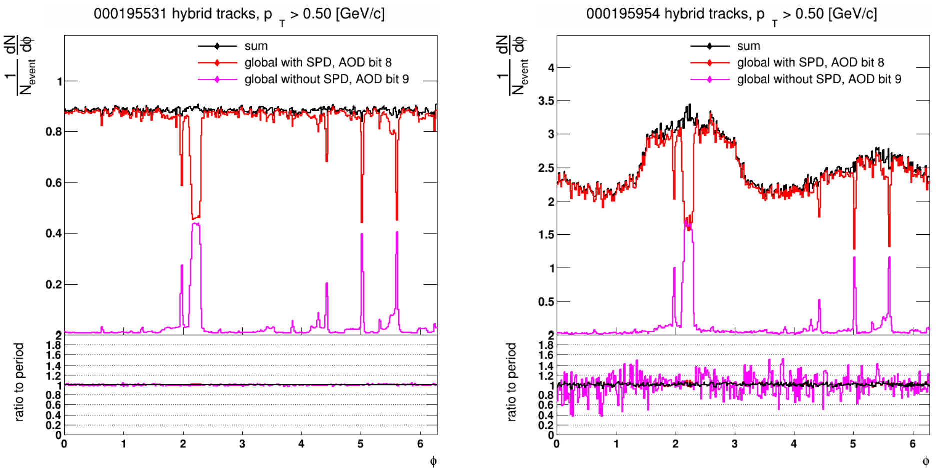

Figure 6.1: Track distribution in azimuth for minimum bias (left) and EMCal triggered (right) run. Black full distribution is decomposed into tracks with tight cuts (red) and released complement (magenta). A hole in ITS is clearly visible as decreased efficiency of the tight cuts.

Tracks used in analysis are with $p_{\mathrm{T}} > 150$ MeV and $|\eta| < 0.9$. The EMCal clusters are cleaned of the fake (exotic) clusters. Cluster $E > 300$ MeV is required.

Track to cluster matching was used to avoid double counting energy of a track that also creates a deposits in EMCal. The charged tracks were extrapolated to EMCal, to a point 440 cm in radius. The p_{T} of all tracks matched to the given cluster during the data production was subtracted in case that the track passed cuts: $\Delta\varphi < 0.03$ and $\Delta\eta < 0.015$.

The track residuals in η and φ, separate for positive and negative track charge and positive and negative η are shown on Fig. 6.2. The fact that the distributions for positively and negatively charged tracks differ in φ is given by non p_{T} dependent distance of the track extrapolation.

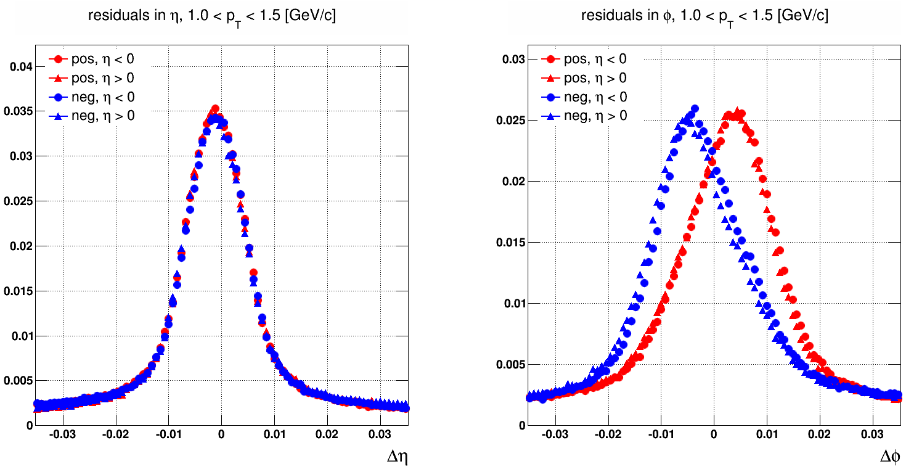

Figure 6.2: Residuals in η (left) and φ (right) from track matching in an example p_{T} bin. Each plot shows separate distributions for positive and negative track charge and positive and negative η.

Charged/full energy ratio in underlying event

The main target is to estimate the contribution of Underlying Event (UE) to a full jet (pointing to EMCal), using information from perpendicular event section (charged tracking available only). The perpendicular event section, due to the limited EMCal acceptance, can be reconstructed only by use of charge tracks. In order to estimate the full UE background (EM+charged) in fully reconstructed EMCal jet one needs to understand the average ratio of charge/full energy depositions in UE. The UE is estimated inside a circular acceptance rotated 90 degrees in φ, with area identical to the one of signal jet.

The underlying event will be estimated for a highly biased selection of events (including high p_{T} jets). To understand the ratio between charged and full energy deposition event rotation technique was used. We explored events with charged jets pointing in a perpendicular direction to EMCal and studied the background “UE” jet in the EMCal. The main advantage of this method is that triggering on charged jets gives a very similar event bias and that the 90 degree area where UE is estimated points to EMCal coverage, so that the UE full/charged energy ratio can be studied.

The p_{T} and E_T was then reconstructed from TPC and EMCal in the EMCal acceptance (after hadronic correction). The minimum bias triggered data sample LHC13b was used to conduct this study.

The full/charged energy ratio was obtained by integrating all track p_{T} and cluster E and making single division of the integrated energy as a function of V0A centrality (Fig. 6.3).

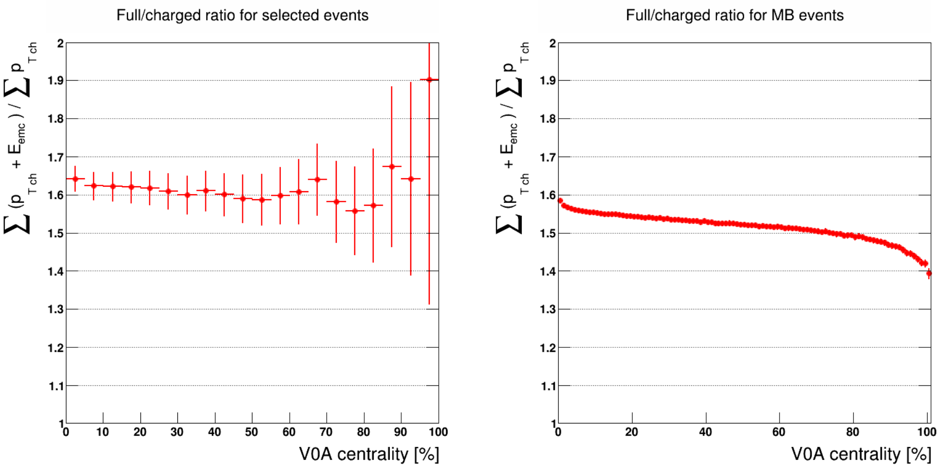

Figure 6.3: The full/charged scale obtained from studying an area rotated 90 degrees in φ from signal charged jet. All events energy deposits are integrated before making the ration. Left: events with jets; Right: minimum bias events

A second approach to recover the full/charged deposition scaling factor was used as a cross check. A sparse underlying event extraction method (see 6.2.2 for details) is executed on charged tracks only and then on the charged tracks + EMCal clusters. The sparse method is based on clustering all (but leading jets) energy into k_{T} jets and estimating this way the underlying event. The difference between the estimated UE with the two data sets (charged only/full) should give the full/charged energy scale, after correction to limited EMCal acceptance. The result is shown on Fig. 6.4.

It is also interesting to have a look how stable the full/charged scale is event by event. Fig. 6.5 shows the first method ratio event by event. It is evident that the there is an important fraction of events which do miss either tracks or clusters in the EMCal acceptance. Also it can be seen that the ratio is not stable but rather fills all possible values.

One can omit the events which do not contain either tracks or clusters and construct

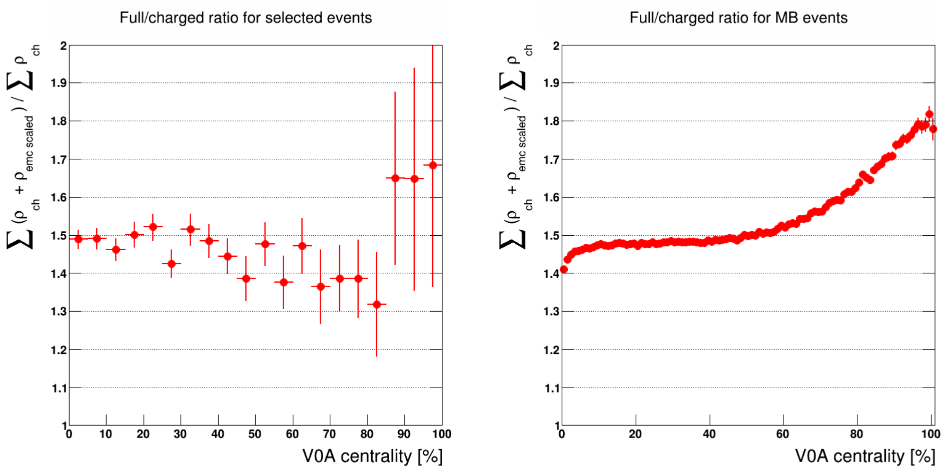

Figure 6.4: The full/charged scale obtained from ratios of UE estimated by the sparse method (6.2.2) Left: events with jets; Right: minimum bias events

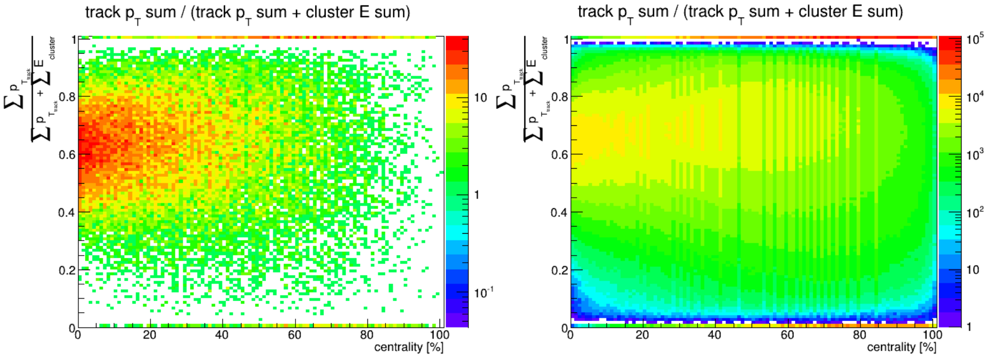

Figure 6.5: The full/charged scale event by event. Left: events with jets; Right: minimum bias events

an average from the event by event ratios from Fig. 6.5. Such ratios are shown on Fig. 6.6.

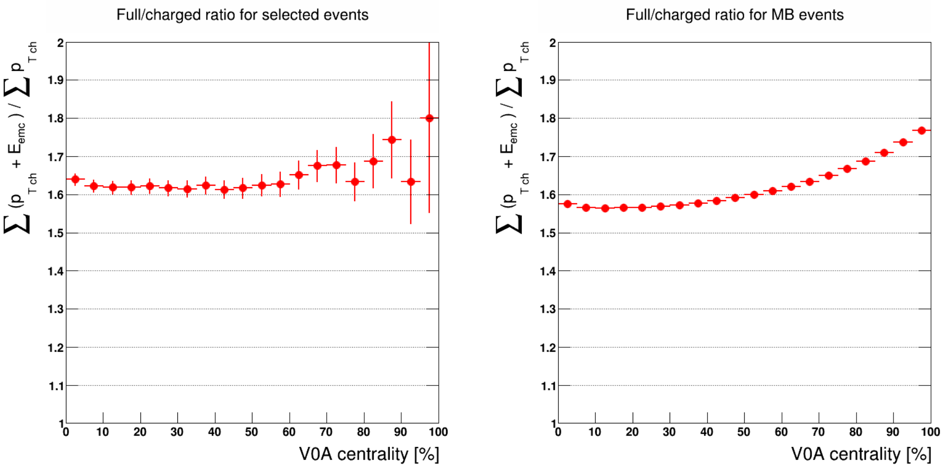

Figure 6.6: The EM scale obtained from event by event ratios Left: events with jets; Right: minimum bias events

The full/charged scale obtained using division of tracks and cluster spectra, either event-by-event or integrated over all events, is similar with value ≈ 1.62. It should be also noted, that for the value is constant in centrality for the event sample with jets (which is expected). The method that uses division of UE reconstructed in charged only or full data set yields a slightly lower value close to 1.5. The origin of the $\approx 7\%$ difference is not evident. The value of 1.62 was used for the later analysis. Variation of the scale is one of the systematics sources.

6.2.2 Jet reconstruction

Fastjet package [172] is used to reconstruct jets. The anti-k_{T} and k_{T} algorithms are used, each for different purpose. The jet finding is run on a combined sample of input vectors of charged tracks and clusters or only tracks.

To obtain the signal jets, the anti-k_{T} algorithm ($R = 0.4$) on the combined tracks and clusters sample is used. To obtain the jet background (UE), as discussed in the following section, the k_{T} algorithm with tracks only and anti-k_{T} with tracks only is used. The limited EMCal acceptance is the reason for use of charged only data sample for UE subtraction.

Underlying event subtraction

A contribution from the underlying event is estimated using a median ρ of the distribution of the jet transverse momentum per jet area for all jets in an event [173,174]

$$\rho = \underset{j\,\in\,\mathrm{jets}}{\mathrm{median}} \left\{ \frac{p_{\mathrm{T}j}}{A_j} \right\} . \tag{6.1}$$

where A_{j} is area of a jet given by the jet finder.

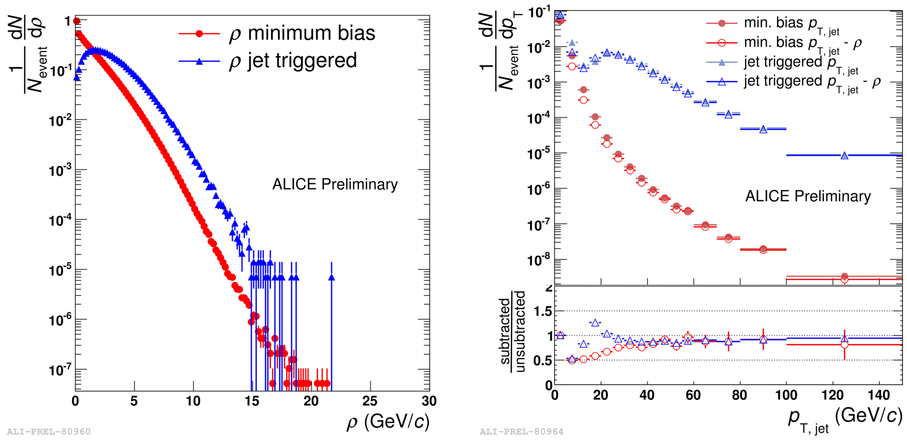

Figure 6.7: Left: the ρ parameter Eq. (6.1) for MB and jet high threshold triggers. Right: comparison of jet p_{T} spectra before and after the ρ subtraction, for the same triggers.

For this purpose a k_{T} algorithm is run on charged tracks only in the full acceptance. Taking advantage of the k_{T} algorithm behavior, that starts clustering from soft particles and creates not very circular jets.

The p_{T} cut on produced jets is lowered to zero, so that all fastjet jets are recovered. The decreased p_{T} cut also results into practically whole acceptance being covered with jets. For the p–Pb collisions multiplicities, those will be mostly jets composed of ghost particles[1].

The anti-k_{T} algorithm is run on the charged tracks as well, with 5 GeV/c cut on the jet p_{T}. To avoid counting signal jets into the underlying event, two most energetic k_{T} jets are removed first. Additionally, the produced k_{T} and anti-k_{T} jets are matched by constituents. Every k_{T} jet sharing a constituent with the $p_{\mathrm{T}} > 5$ GeV/c anti-k_{T} jet is removed. As the last removal step, all jets with $p_{\mathrm{T}} < 0.1$ GeV/c are removed (ghost particle jet removal).

---

[1] Ghost particles are virtual hits of infinitely small energy that are introduced by jet finding algorithms. The ghost particles fill the acceptance homogeneously.

Area and median of the p_{T} of the remaining k_{T} jets are computed. The median is then extrapolated to the full acceptance by using the ratio of areas of the remaining jets and all initial jets (which fill the whole acceptance). The obtained value is valid for charged jets background. It is not possible to run the same method for full jets due to limited calorimeter acceptance. A scale factor of 1.62 (see 6.2.1) is used to scale the underlying event contribution to full jets.

Fig. 6.7 shows results of the method. The UE subtraction changes the jet p_{T} distribution shape below $p_{\mathrm{T,jet}} \approx 40$ GeV/c. The UE of jet triggered events is higher.

6.3 The analysis of the dN/dj_{T} distribution

Transverse momenta of charged jet constituents in respect to the jet axis (j_{T}) are extracted. The jet finding algorithm provides an axis of the reconstructed jet and a list of its constituents (tracks and cluster). Charged constituent track objects only are used to fill the j_{T} spectra. Background of the j_{T} distribution coming from the the underlying event is subtracted (6.3.3).

6.3.1 Binning and trigger counts

The analyzed jets are sorted into bins according to their p_{T}, labeled as trigger bins. The analyzed constituents are also sorted into bins according to their p_{T}, labeled associated bins. Table 6.1 holds the bin borders.

trigger bin borders [GeV/c]	20,30,40,60,80,100,150
associated bin borders [GeV/c]	0.5,1,3,10,20,50,100

Table 6.1: Trigger and associated bin borders.

Triggered data

The amount of available triggers in the given bins is shown on Fig. 6.8. It can be seen, that the low threshold jet trigger (EJ2, blue triangles) did not provide too much of an enhancement in absolute number of jets.

Fig. 6.9 shows the turn on curves for the triggered data. It is safe to assume that the plateau starts at 50 GeV/c for the low threshold and at 60 GeV/c for the high threshold. This correlates well with the low and high online threshold difference of 10 GeV.

The j_{T} spectrum for jet bins above the 60 GeV/c is produced from the triggered data sample using the high threshold. The low threshold is not used (it doubles the data sample in between 50-60 GeV/c).

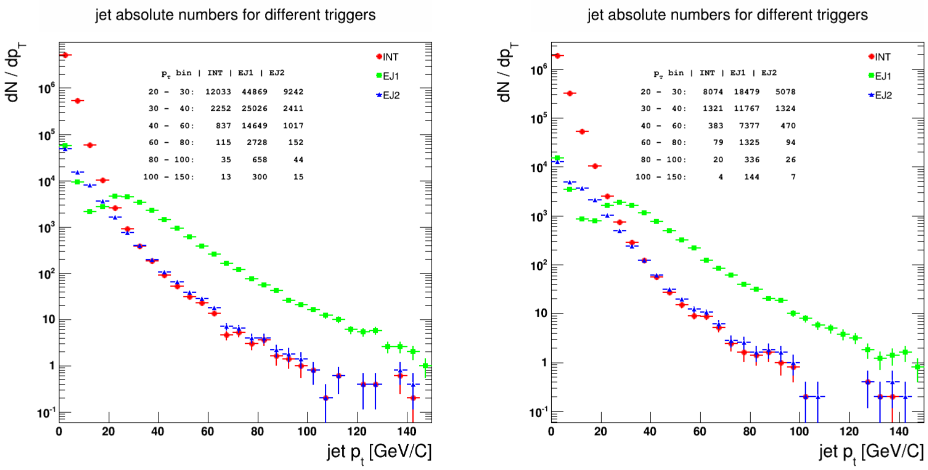

p_T bin	INT	EJ1	EJ2
20 - 30:	12033	44869	9242
30 - 40:	2252	25026	2411
40 - 60:	837	14649	1017
60 - 80:	115	2728	152
80 - 100:	35	658	44
100 - 150:	13	300	15

p_T bin	INT	EJ1	EJ2
20 - 30:	8074	18479	5078
30 - 40:	1321	11767	1324
40 - 60:	383	7377	470
60 - 80:	79	1325	94
80 - 100:	20	336	26
100 - 150:	4	144	7

Figure 6.8: Absolute numbers of triggers in the 2013 p–Pb data set, periods LHC13b,c,d,e. INT is minimum-bias trigger (red circles); EJ1 (green squares) high threshold jet trigger; EJ2 (blue triangles) low threshold jet trigger. The table inside the plot contains integrated numbers of triggers in bins given by table 6.1. Left: $R = 0.4$; Right $R = 0.5$. Larger R implies smaller EMCal acceptance due to fiducial cut, and consecutively lower reconstructed jet multiplicity.

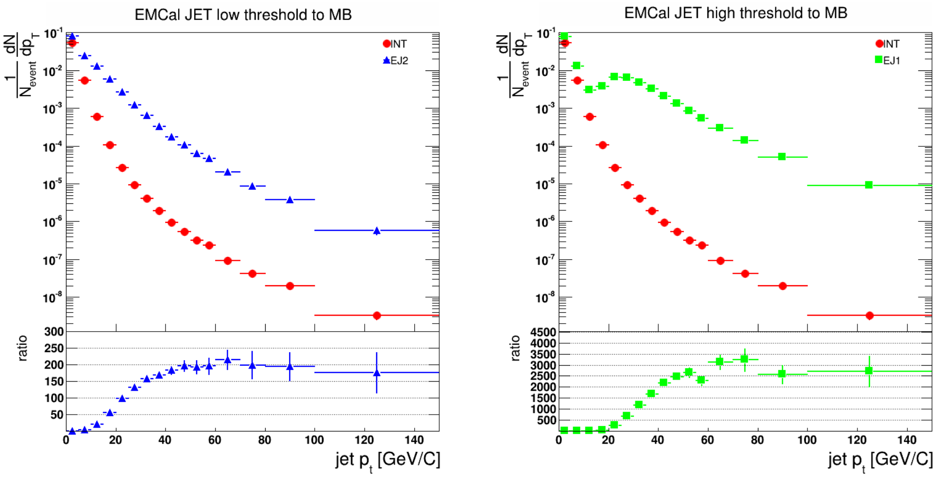

Figure 6.9: Triggered jets distribution compared to minimum bias, normalized per event. Trigger turn on curves (division of the two spectra) are plotted at the bottom parts of the plots. Left: low trigger threshold Right: high trigger thresholds.

Fig. 6.10 shows number of jets above 20 GeV/c in EMCal. There is one per mil events with 2 jets in EMCal acceptance, none with more, in both triggered and MB data sets. The analysis is conducted for leading jet in EMCal acceptance.

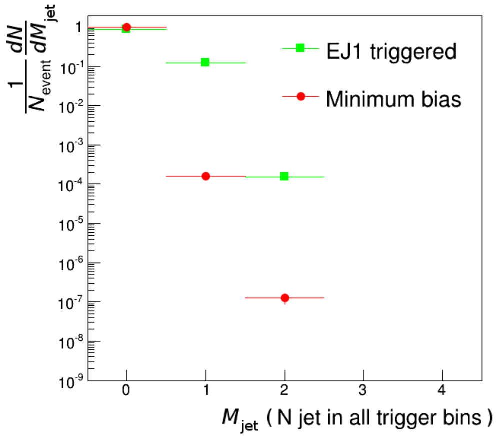

Figure 6.10: Number of jets with $p_{\mathrm{T}} > 20$ GeV/c in events for EJ1 trigger (high threshold, green squares) and minimum-bias data (red circles).

6.3.2 Jet fragmentation transverse momentum j_{T}

The extraction of the j_{T} is done simply by relating two vectors, one given by the jet finder algorithm, which represents the jet axis ($p_{\mathrm{T,jet}}$). The other vector is a charged track ($p_{\mathrm{T,track}}$) passing the hybrid cut. The jet fragmentation transverse momentum is then calculated as

$$j_{\mathrm{T}} = \frac{\vec{p}_{\mathrm{track}} \cdot \vec{p}_{\mathrm{jet}}}{p_{\mathrm{jet}}^2} \tag{6.2}$$

Calorimeter clusters are not used to build the j_{T} spectrum (but are used for obtaining the full jet axis). It was shown that there is no noticeable difference in between considering anti-k_{T} jet constituents and tracks within a fixed cone of R around the jet axis. Constituent method is used.

6.3.3 Background subtraction

The j_{T} distribution contains in its raw form background coming from the underlying event, as the jet finding algorithm clusters everything in the given jet area. The estimation of the underlying event background is done by rotating the jet axis 90 degrees in φ and building j_{T} distribution of particles close to the rotated axis.

Two methods were used to select particles close to the rotated axis. The first method gathers every track in $\Delta R < R$ of the jet finding algorithm. The second method takes

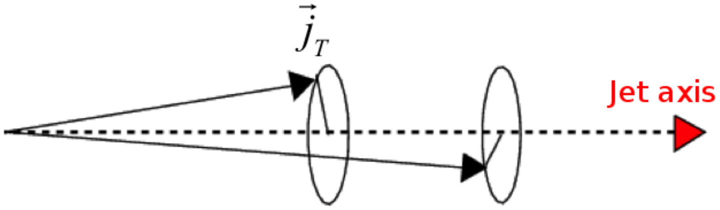

Figure 6.11: Vector $\vec{j}_T$ represents a transverse component of the charged particle fragment (black arrows) with respect to the jet axis (dashed arrow).

into account that the anti-k_T jet is never exactly circular and of a given R. Area of the jet A_j is obtained and particles with $\Delta R < \sqrt{A_j/\pi}$ are filled. Fig. 6.12 shows a comparison of background obtained by the two methods for pp Pythia 8 $\sqrt{s} = 7$ TeV simulation. The normalization of the background is obtained out of the box, as the method is executed once for every trigger jet.

It can be seen that background diminishes for the high p_T associated bins and that there is no difference in between the two background method estimations (fixed cone or comparable area).

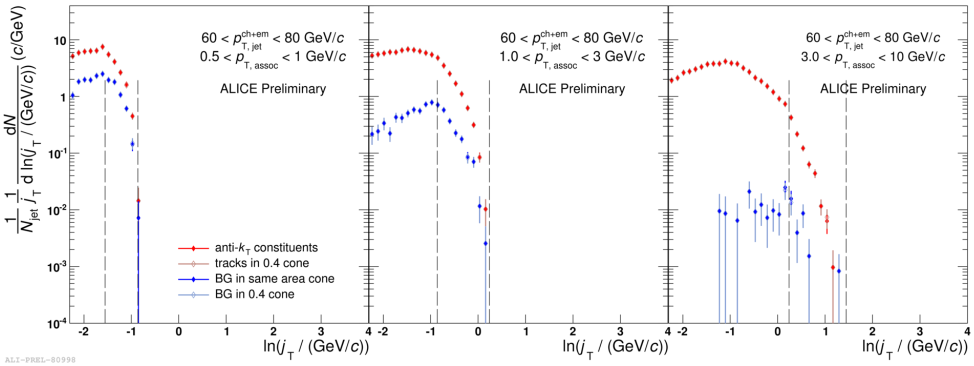

Figure 6.12: The plots show comparison of j_T spectra obtained from either constituents or all tracks in fixed size cone around axis. The background is constructed by either collecting all tracks in a cone with R similar to the jet finder or from a cone with variable R that resizes the cone to area of signal jet. The vertical lines show low and high maximum j_T edges of the associated bins. I.e.: maximum geometrical j_T limit for particle in cone of R (at the edge of it), with max and min p_T of the bin (particle with low p_T can not cross the lower line, particle with high p_T can not cross the higher line).

6.3.4 Raw j_{T} spectrum

Raw j_{T} spectrum was obained using EMCal jet (EJ1) and minimum bias (INT) triggers. The final raw spectrum plot sums all associated bins (single 0.3 - 100 GeV/c p_{T} bin for the charged particles). Ratio EJ1 to INT was made for all bins to check for validity of the statement, that the observable should not be modified by the trigger, once the trigger rejection reaches plateau. Fig. 6.13 shows the obtained plots. Indeed it is seen that the bin 60-80 GeV/c is identical in triggered and MB sample. The higher p_{T} bins suffer from very little statistics in the MB data sample.

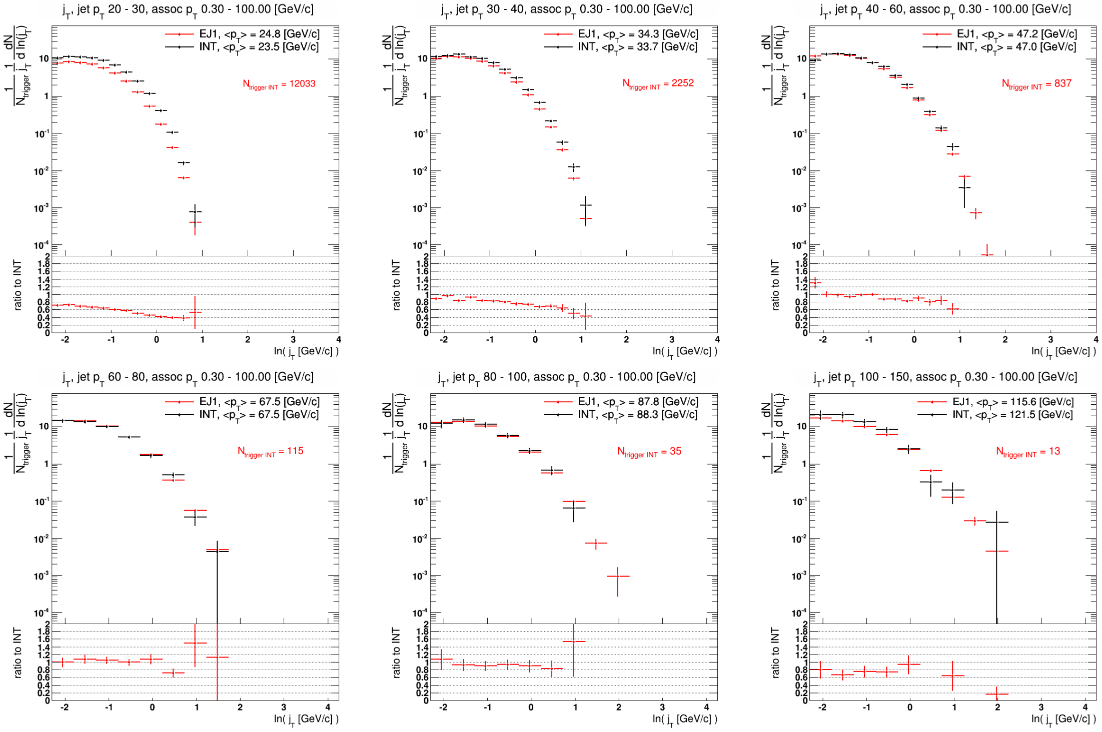

Figure 6.13: Raw j_{T} spectrum for EJ1 (red) and INT (black) triggered jets. All panels show ratio in between triggered and minimum bias spectra. The ration is flat for $p_{\mathrm{T,jet}}$ above 60 GeV/c. Number of high p_{T} jets reconstructed in the latest bins in minimum bias data set is very small, which gives large statistical fluctuation of the ratio.

6.4 Bin by bin correction

The bin by bin correction method is used to correct the j_{T} spectrum for various inefficiencies and effects (tracking efficiency, feed in/out, other detector effects).

The correction is obtained by producing jets and j_{T} spectrum on particle and detector level in full ALICE monte–carlo simulation and dividing the spectra afterwards. The particle level does include all final state particles. Same as in the analysis, all jets hitting the EMCal acceptance are used. Jet matching is not switched on as all possible corrections are of interest (not only detector influence on a specific jet).

The code that processes the MC sample is identical to the code that processes the real data. The only extension of the code is that there is a layer added, which allows to feed the particle level products to the common jet finder and analysis code.

6.4.1 MC normalization

The MC sample (combined LHC13b4_fix and LHC13b4_plus) is a Pythia production of the same $\sqrt{s}$ as the p–A collisions. The sample is produced in multiple p_{T} hard bins (Tab. 6.2). Standard Pythia cross section and N tries method was used to normalize the various bins. Normalized jet spectrum is shown on Fig. 6.14.

MC bin borders [GeV/c]	5,11,21,36,57,84,117,152,191,234,inf

Table 6.2: MC production p_{T} hard bin borders.

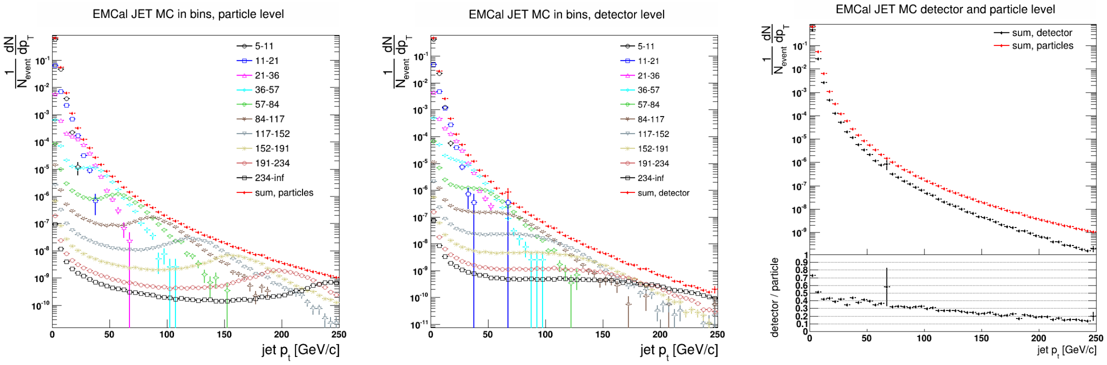

Figure 6.14: Jet spectrum as composed from various normalized MC production bins. Left: particle level. Middle: detector level. Right: ratio. The plots show that spectrum shape is smooth after being reconstructed from multiple MC production bins.

6.4.2 Feed-in, Feed-out

The amount of not reconstructed MC jets was checked. Also the amounts of MC jets which end up in different p_{T} bins on the detector level were studied. The feed out to higher p_{T} is very low, the feed out to lower p_{T} bins is significant (Fig. 6.15). Feed in to detector level jet bins was studied similarly. Jets outside of considered bins are marked not reconstructed.

Jet matching was used to link particle and detector level jets, so that feed in/out can be studied. Jets were considered matched, if Δr of their axes was lower than the R of the jet finder algorithm.

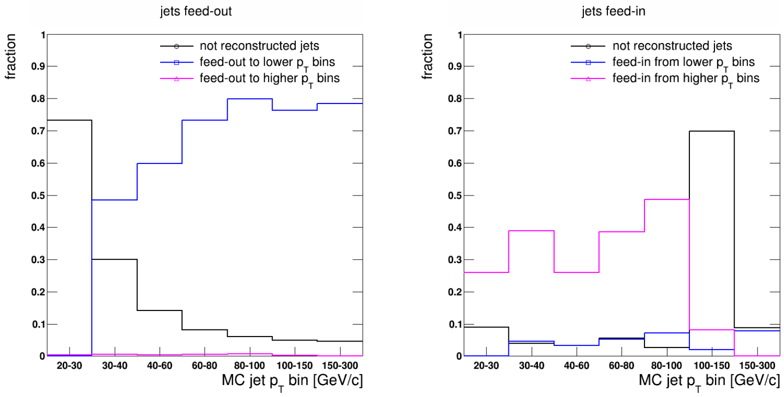

Figure 6.15: Left: fraction of MC jets that does not get reconstructed on the detector level or falls to higher or lower p_{T} bins. Right: fraction of detector level jets, that comes from particle level jets that are not reconstructed or in different p_{T} bins.

6.4.3 Jet background fluctuation Δp_{T}

Background fluctuation Δp_{T} was extracted from data as a difference of the jet background (ρ) subtraction method and random cone background.

The extracted background distribution was then sampled to randomly vary jet p_{T} in MC study. The additional feed-out due to Δp_{T} variation is shown on Fig. 6.16.

The additional feed out fractions were then used to create a final correction as a weighted sum of all bin corrections that contribute to the given target jet p_{T} bin.

6.4.4 Correction factors

Fig. 6.17 shows correction functions as obtained from the MC. Fig. 6.18 shows the same comparison of correction with and without the Δp_{T} fluctuation included. Vertical lines in the division parts of the plots show the reach of j_{T} from real data. The correction is fit with polynomial of 3rd order.

Fig. 6.19 shows correction decomposed according to origin of the jet into correction for jets reconstructed in the same p_{T} bin and correction for jets that are fed in from lower and higher p_{T} bins. The correction for jets from higher bins has a significant concave shape. This can be explained by presence of higher momentum particles (which give also higher j_{T}) in jets reconstructed by inefficiencies in lower p_{T}, where the high j_{T} is generally lower.

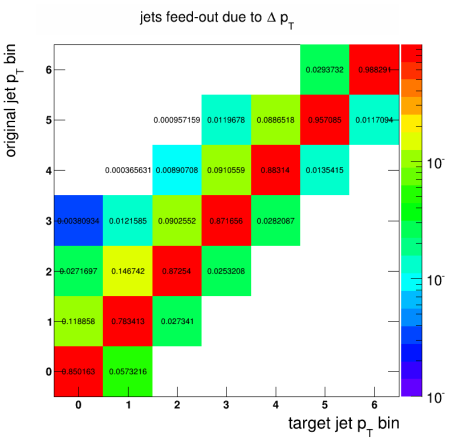

Figure 6.16: Additional feed out due to Δp_{T} variation. The plot shows how jet p_{T} bin changes after additional Δp_{T} smearing is applied (from original y-axis to after smearing x-axis). Numbers give fractions of jets and sum to 1 for each column. The amount of jets that end up in lower bins is larger.

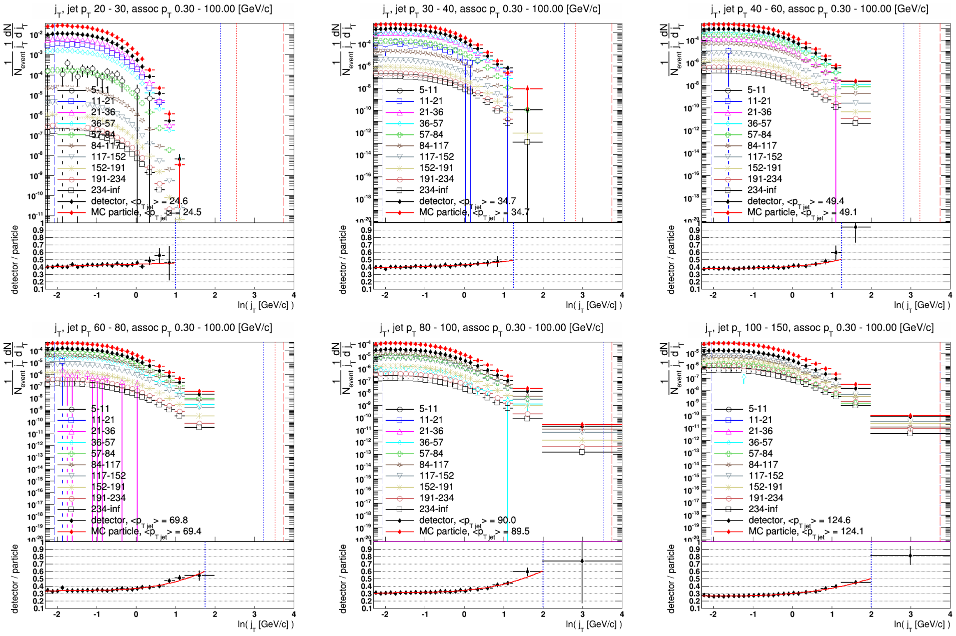

Figure 6.17: Correction factors obtained from Pythia full MC simulation. The vertical lines in the division area show reach of real data spectrum. The fit is polynomial of 3rd order.

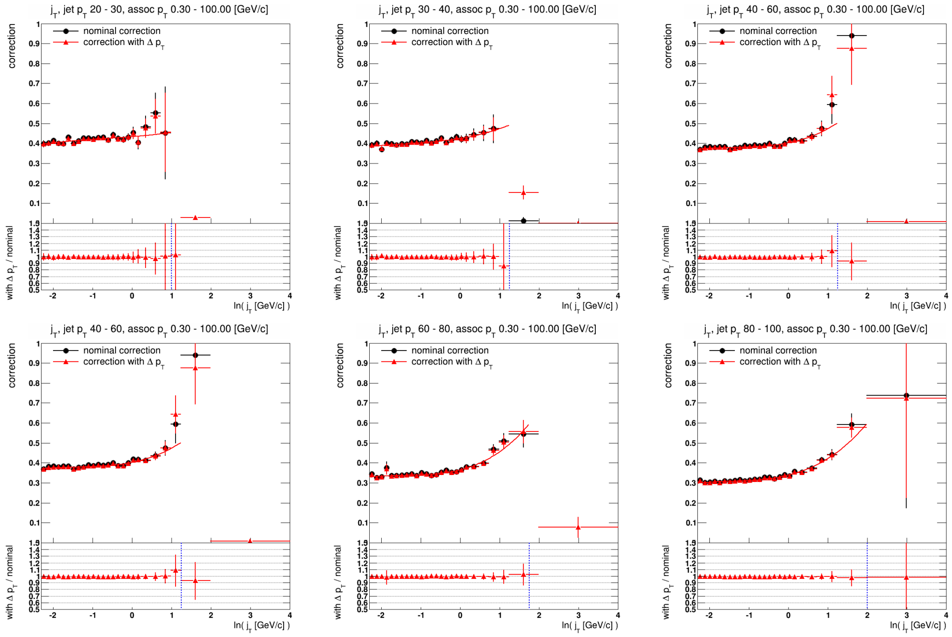

Figure 6.18: Correction factors compared with and without the re-weighting due to additional feed out due to Δp_{T} fluctuation.

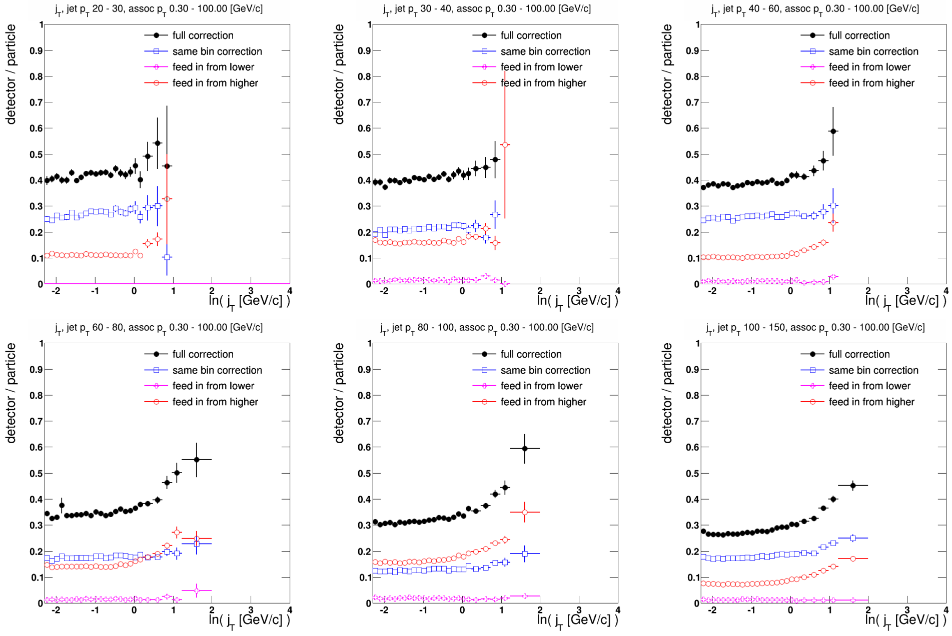

Figure 6.19: Decomposition of correction according to the jet origin; jets reconstruct in same p_{T} bin, jets fed in from higher and lower bins.

Fig. 6.20 shows correction in separated MC $p_{\mathrm{T},hard}$ production bins. There is no observed dependence of the correction function shape on the $p_{\mathrm{T},hard}$ of the MC event.

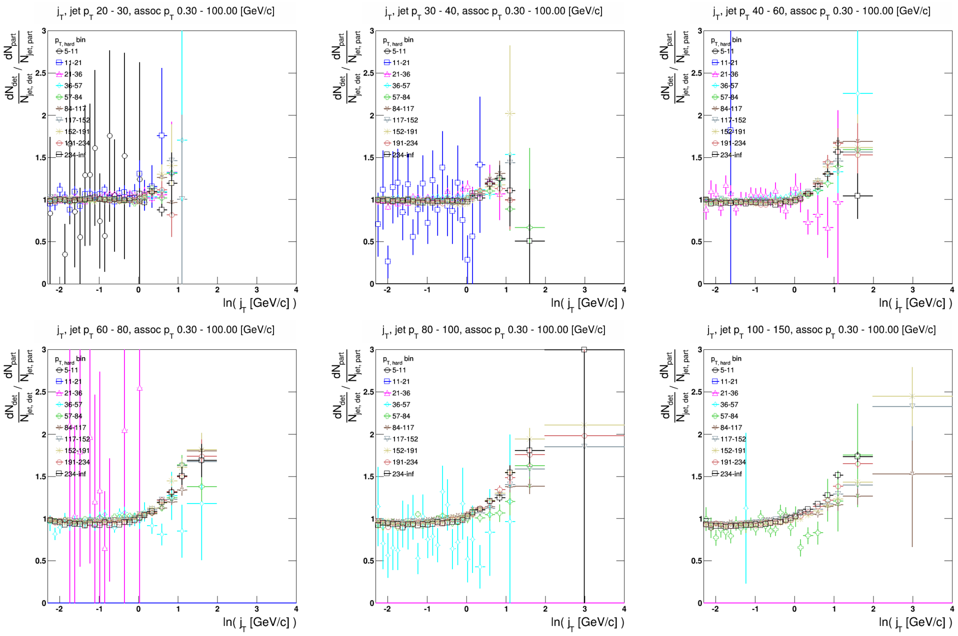

Figure 6.20: Correction separated by different MC LHC13b4 production $p_{\mathrm{T},hard}$ bins.

6.5 Analysis of systematical uncertainties in the $\mathrm{d}N/\mathrm{d}j_{\mathrm{T}}$ distributions

The uncertainties in this analysis arise from uncertainty of the bin-by-bin correction and cuts used in the analysis. Cuts were varied to study the uncertainty.

6.5.1 Correction uncertainty

The correction uncertainty was obtained by removing randomly 5% of the detector level (reconstructed) tracks. This simulates a 5% uncertainty in tracking efficiency. It is assumed that the effect is symmetric, as it is not simply possible to add reconstructed tracks. Uncertainty is obtained by division of two fits of the correction functions (one nominal, the other with the 5% altered detector level), ± uncertainty obtained is then applied.

Fig. 6.21 shows the fits through the two corrections. Fig. 6.22 shows the construction of the final correction uncertainty. The final uncertainty is a quadrature addition of the corrections fit ratio and the fit error (fitter error of the pol3 constant parameter).

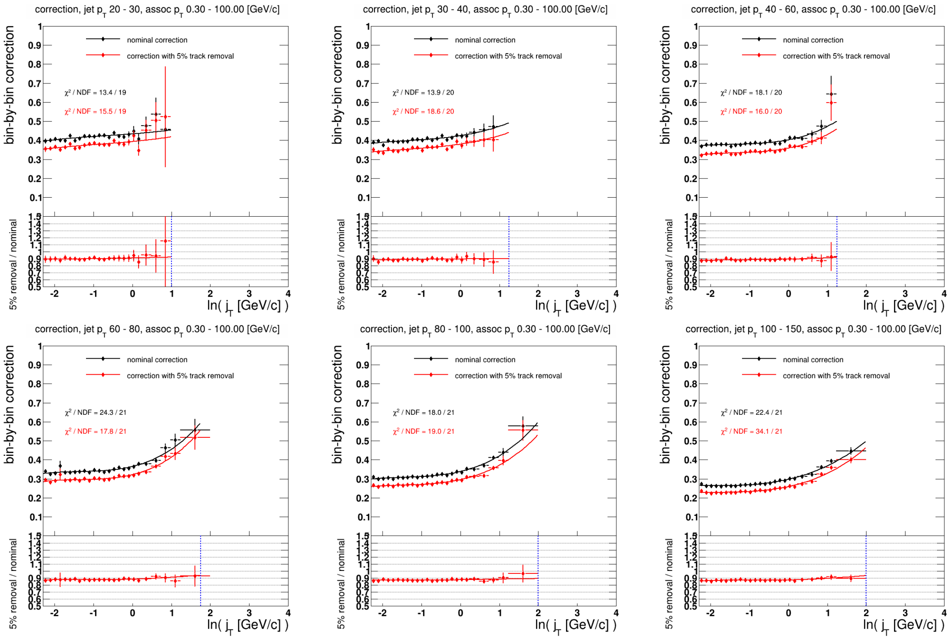

Figure 6.21: Correction factors obtained from Pythia full MC simulation, one more lover MC bin included.

6.5.2 Hadronic correction uncertainty

The charged track momentum is fully subtracted from the matched EMCal cluster. This is a safe approach in the sparse environments of the pp and p–A collisions, where it is unlikely that the charged track would overlap with neutral particle. Still, to assess possible systematic error, the hadronic correction was varied from 100% matched charged track momentum subtraction to down to 70%. The uncertainty was obtained by dividing a modified j_T spectrum by the nominal one and was found to be minimal.

6.5.3 EMCal scale uncertainty

The jet full background is subtracted, (as discussed at 6.2.2), by using charged background scaled to full level. The scale factor was varied to 50% to obtain uncertainty of the given approach. The uncertainty was obtained by dividing a modified j_T spectrum by the nominal one.

Fig. 6.23 shows combined uncertainties of the hadronic correction and scale factor. The uncertainty is found to be below 10%, except for very high j_T values, where the statistics is low.

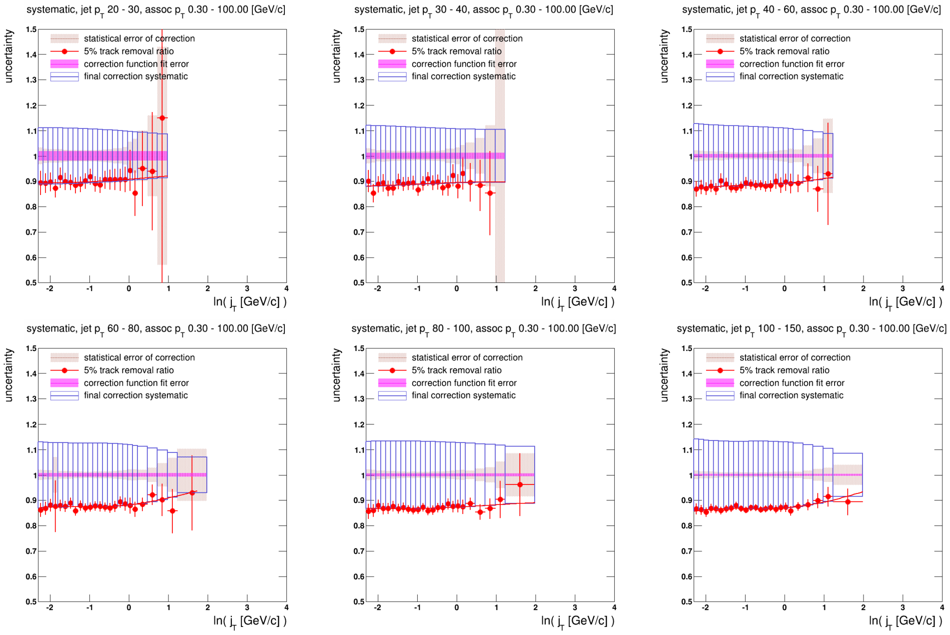

Figure 6.22: Correction uncertainty. Red points are ratio of two corrections (with and without 5% track removal), with red line fit. The black points show difference in between fit with and without the high j_{T} kink. Magenta area shows fit error. Shaded area represents statistical errors of the nominal correction. Blue squares stand for the final correction.

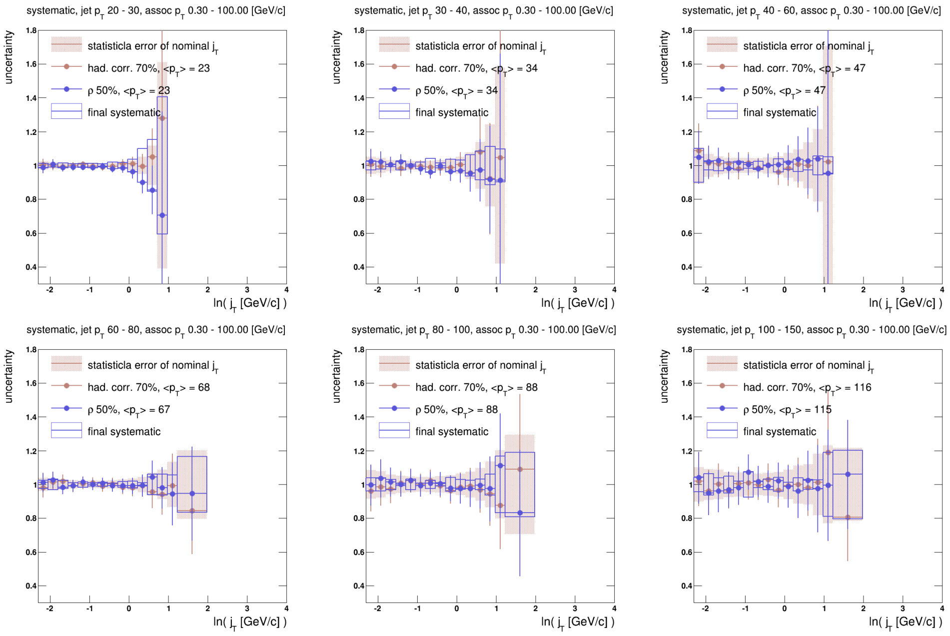

Figure 6.23: Ratio of nominal and modified j_{T} spectrum for hadronic correction (brown), EMCal scale (blue) uncertainties. The blue boxes show combined uncertainty. Shaded area shows statistical errors of the nominal j_{T} distribution.

6.6 Pythia study

An extensive Pythia 8 and Pythia 6 study was carried out to understand effects from jet reconstruction parameters and to gain insight on the sensitivity to different physics phenomena. A preceding analysis of j_{T} spectrum was done by the CDF collaboration [100]. It was also studied how the results from two experiments with significantly different setups can be compared.

The Pythia generated events were directly connected to the analysis code, so that the same code can run on both real data and Pythia produced events. The charged tracks were built from final charged Pythia particles. The clusters were built from photons. No event cuts, track selection and trigger selection were performed. The rest of the analysis code remained identical to the code used in the final analysis.

6.6.1 Comparison to CDF results

Aside a difference in the collisions (p$\bar{\mathrm{p}}$ $\sqrt{s} = 1960$ GeV), the CDF has full azimuthal coverage of calorimeters and much higher acceptance $|\eta| < 4$. The CDF analysis selected balanced full di–jet events with jets reconstructed with a cone $R = 1.0$ algorithm.

The target of this part of the Pythia study was to evaluate effects of selecting all jet events in ALICE EMCal acceptance (instead of balanced di–jets), choosing anti-k_T algorithm instead of cone and lowering the R to 0.4 or 0.5. The CDF analysis was carried out in bins of di–jet mass (M_jj), which is also impossible to do in ALICE (p_T binning chosen instead).

Initially, the CDF results were reproduced using similar Pythia 6 setup as used for CDF (their data were well described by Pythia). Consequently, the jet finder parameters were modified and di–jet event selection disabled, still using the CDF $\mathrm{p\bar{p}}$ collisions setup. Finally, the collisions were switched to LHC parameters. The j_T spectra were compared in between the steps.

6.6.2 Jet finder effects

Effects of different jet finder usage on the j_T spectrum are shown on Fig. 6.24 and 6.25. The j_T spectrum in the CDF analysis is constructed from charged particles within a rigid $R = 0.5$ cone around the found jet axis, no matter on what jet finder is used to locate the jet. The M_jj and p_T bins are defined by the jet finder from all the constituents. The M_jj and p_T binning according to constituents within the rigid 0.5 cone was also tested, to eliminate effect of different size jet finders placing the found jet in different bins.

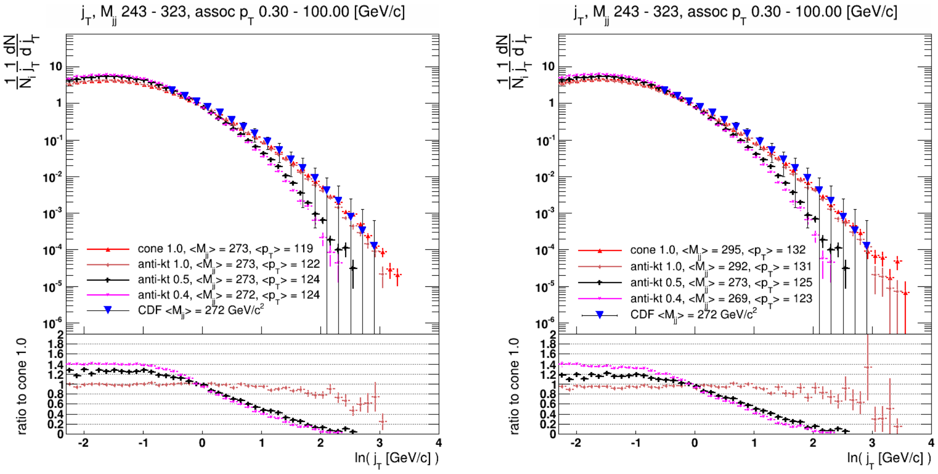

Figure 6.24: Comparisons of jet finder effects on j_T spectrum in 0.5 rigid cone around jet axis. Left: binning defined by all constituents. Right: binning defined by constituents in the 0.5 cone.

Only the shapes of the spectra were compared (not the total yields), because the CDF analysis used normalization such, that the value of $\ln(j_\mathrm{T})$ at 0 is normalized to 1. The conclusion from the test is that the jet finder setting has a significant effect on the shape of j_T distribution. This is an interesting effect, as the distribution is always

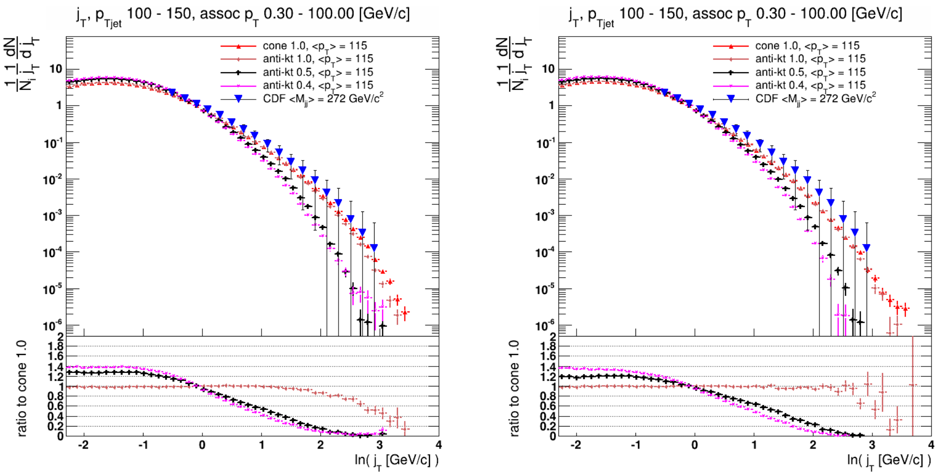

Figure 6.25: Comparisons of jet finder effects on j_{T} spectrum in 0.5 rigid cone around jet axis. With ALICE–like jet and event selection (all jets instead of balanced di–jet events). Left: binning defined by all constituents. Right: binning defined by constituents in the 0.5 cone.

composed from charged tracks in the same rigid cone around jet axis. It has been also found that differences mainly come from the jet finder scale parameter R, there is a very small difference in between cone and anti-k_{T} of the same size. Most likely explanation is that the axis of the located jet is dependent on the R parameter. This can be explained by possible jet splitting or the fact that a smaller jet cone can be more easily tilted towards a more energetic constituent, hence decreasing its transverse momentum.

6.6.3 Event selection effects

The events for the CDF analysis are selected to contain balanced di–jets. The balance is evaluated by combining the four vectors of the two leading jets. The balance is equal to magnitude of the resulting vector component, that is perpendicular to another vector, which is constructed to point in the middle of opening angle in between the two jets in the plain defined by the two jets.

The events for the ALICE analysis can not contain two full jets, because of the limited calorimeter acceptance. Hence no di–jet event selection is done. Leading jet reconstructed in EMCal is considered.

Effect of the event selection was studied by comparing spectra in bins with close $\langle p_{\mathrm{T}} \rangle$, because the M_{jj} binning can not be used in ALICE analysis. The alignment of the $\langle p_{\mathrm{T}} \rangle$ is not perfect and is believed to cause the spectra difference in higher j_{T} region. The ALICE analysis has slightly lower $\langle p_{\mathrm{T}} \rangle$, which results in lower j_{T} spectrum in higher j_{T} region. Even with the imperfect bin alignment, it was found that the di–jet event selection has no significant effect on the final spectrum (Fig. 6.26). For the purpose of the study, the virtual ALICE acceptance was enlarged in η so that $R = 1.0$ jets do fit in the acceptance.

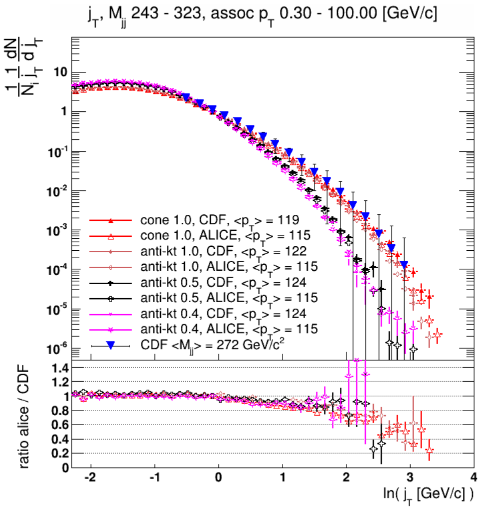

Figure 6.26: Study of the effect of event selection on the final spectra. CDF balanced di–jet event selection versus ALICE all jets in slightly enlarged EMCal acceptance selection.

6.6.4 Rigid cone effect

The effect of composing j_{T} spectrum from charged particles in a rigid cone around the jet axis, versus from the charged constituents of the jet was studied. The main target was to compare performance for the anti-k_{T} $R = 0.5$, when the cone and jet finder scale are the same. It was found that there is no effect when taking the charged constituents or charged particles in the rigid cone for the R similar to the R of the jet finder (Fig. 6.27).

6.6.5 Collision energy effect

It was studied what is the effect of the collisions setup on the final j_{T} spectrum. Comparison of p$\bar{\mathrm{p}}$ $\sqrt{s} = 1960$ GeV (CDF, Tevatron) and pp $\sqrt{s} = 5020$ GeV (ALICE, LHC) was studied. The ALICE–like event and jet selection was used for the comparison. The result shows not a significant effect (Fig. 6.28).

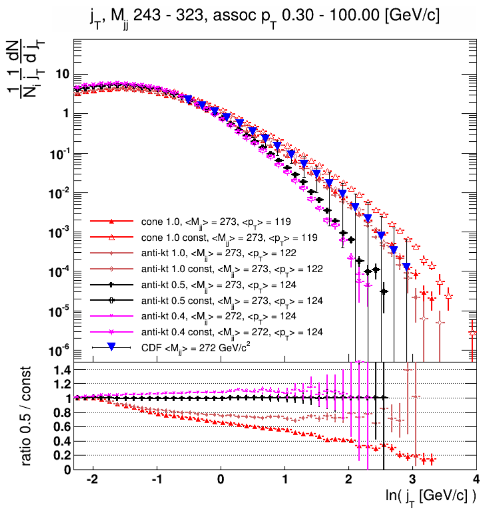

Figure 6.27: Comparison of spectra from charged particles 0.5 cone and all charged jet constituents.

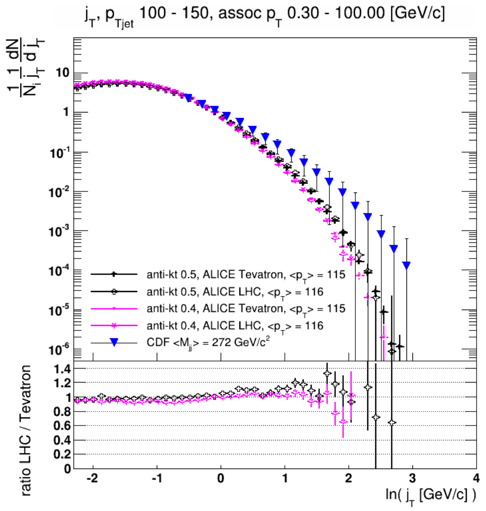

Figure 6.28: Comparison of spectra obtained from ALICE style analysis in different collisions p$\bar{\text{p}}$ $\sqrt{s}$ = 1960 GeV (Tevatron) and pp $\sqrt{s}$ = 5020 GeV (LHC)

6.6.6 Pythia 6 and 8 comparison

The ALICE–like event and jet selection analysis was also used to compare the Pythia 6 and Pythia 8 results. Both Pythias were tunned with the CDF A tune, using the LHC collisions. The difference is found to be minimal (Fig. 6.29). The test was conducted mainly to study the difference in between mass and p_{T} ordering of the shower evolution Pythia 6 and Pythia 8 respectively.

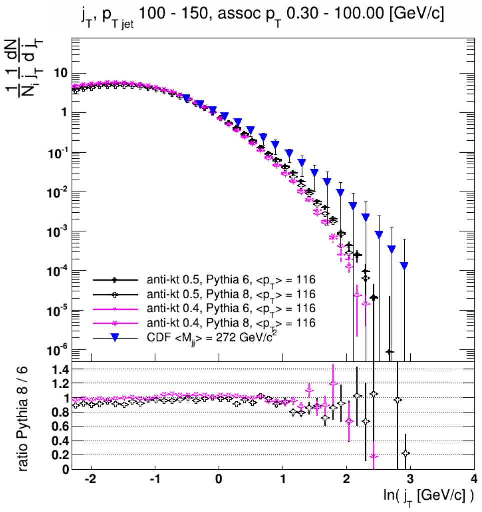

Figure 6.29: Comparison of spectra obtained from Pythia 6 and Pythia 8.

6.6.7 Conclusion of the Pythia study

It was shown that the method is well understood and CDF results can be reproduced. The final j_{T} spectrum is dependent on the jet finder scale parameter R that is used, hence comparison of the data obtained from ALICE with the CDF results will be difficult. The j_{T} spectra is not significantly altered by the event and jet selection or the $\sqrt{s}$ of the collisions.

6.7 Results

The results are presented in form of j_{T} spectrum of the charged constituents of full jets in the given jet p_{T} bins. The spectrum is normalized to unity at $\ln(j_{\mathrm{T}}) = 0$. The arbitrary normalization is required in order to be able to compare the data to the NMLLA theory computation [101, 102]. This theory implements local parton hadron duality instead of any more sophisticated hadronization model. Pythia 6 CDF A tune simulation was used to provide the comparison to the simulation. In order to study how significant the color coherance effects, namely angular ordering, are we switched off angular ordering in Pythia 6 (MSTJ(42) = 1).

Fig. 6.30 shows the final spectrum for the given jet p_{T} bins. Fig. 6.31 shows comparison to the MC.

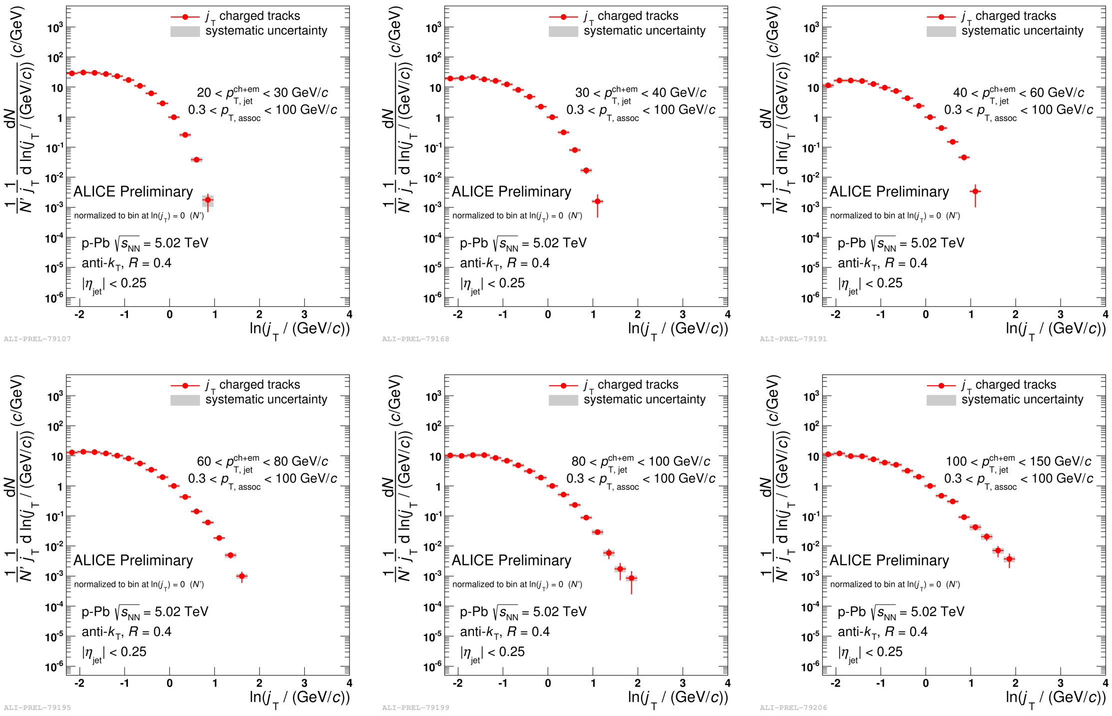

Figure 6.30: Final j_{T} spectrum of charged constituents of full anti-k_{T} $R = 0.4$ jets in p–Pb collisions. The spectra are plotted for jets in $p_{\mathrm{T,jet}}$ bins of 20-30-40-60-80-100-150 GeV/c.

6.7.1 Comparison to theory

The NMLLA prediction was obtained for the given jet p_{T} bins from R. Perez-Ramos and is an application of [101, 102] to the LHC energies. The theory works with jet virtuality instead of the jet p_{T}. The original calculation was done in bins of jet virtuality $Q = E \cdot R$ with R being the jet cone size. Due to the small EMCal η acceptance reconstructed jets rapidities are very small and thus the virtuality can be approximated as $Q = p_{\mathrm{T}} \cdot R$. The prediction was then generated for virtuality equivalent of the average jet p_{T} in the given analysis bin.

The theoretical $\mathrm{d}N/\mathrm{d}j_{\mathrm{T}}$ is generated separately for gluon and quark jets. Results for both quark and gluon jets are compared with the data in Fig. 6.32. Pythia 8 CDF A

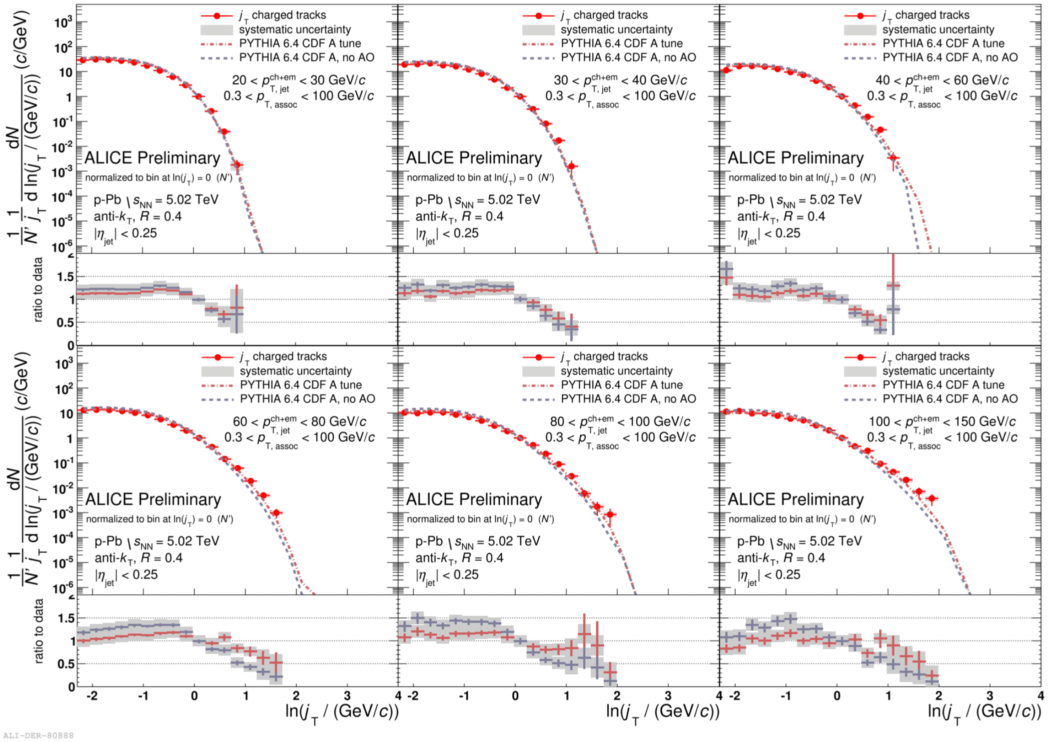

Figure 6.31: Final j_T spectrum compared to Pythia 6 CDF A tune with and without the angular ordering. The naive expectation is that the presence of angular ordering enhances production in the low-j_T region. The observed change in steepness of the j_T in between the two Pythia sets is small, with slightly larger effect for higher p_T jets. On contrary to the naive expectation, the Pythia low-j_T is enhanced in case of switched off angular ordering. The showering in Pythia 6 is mass ordered by default, forcing the angular ordering by parameter may interfere with other aspects showering showering, leading likely to not well simulated shower.

tune MC was run to obtain the quark and gluon jet fractions for the given jet p_{T} bins, by identifying the parton closest to the jet axis as the mother of the jet. The resulting gluon fractions are noted in Tab. 6.3.

Fig. 6.32 shows comparison to the theory and to the CDF data, where those are available. Fig. 6.33 details the comparison to both NMLLA and MLLA calculation for the two selected bins, where the CDF data is available.

jet p_{T} bin [GeV/c]	gluon fraction
20-30	0.7698
30-40	0.7411
40-60	0.7217
60-80	0.7141
80-100	0.7124
100-150	0.6928

Table 6.3: Gluon fractions from Pythia 8 simulation for jet p_{T} bins.

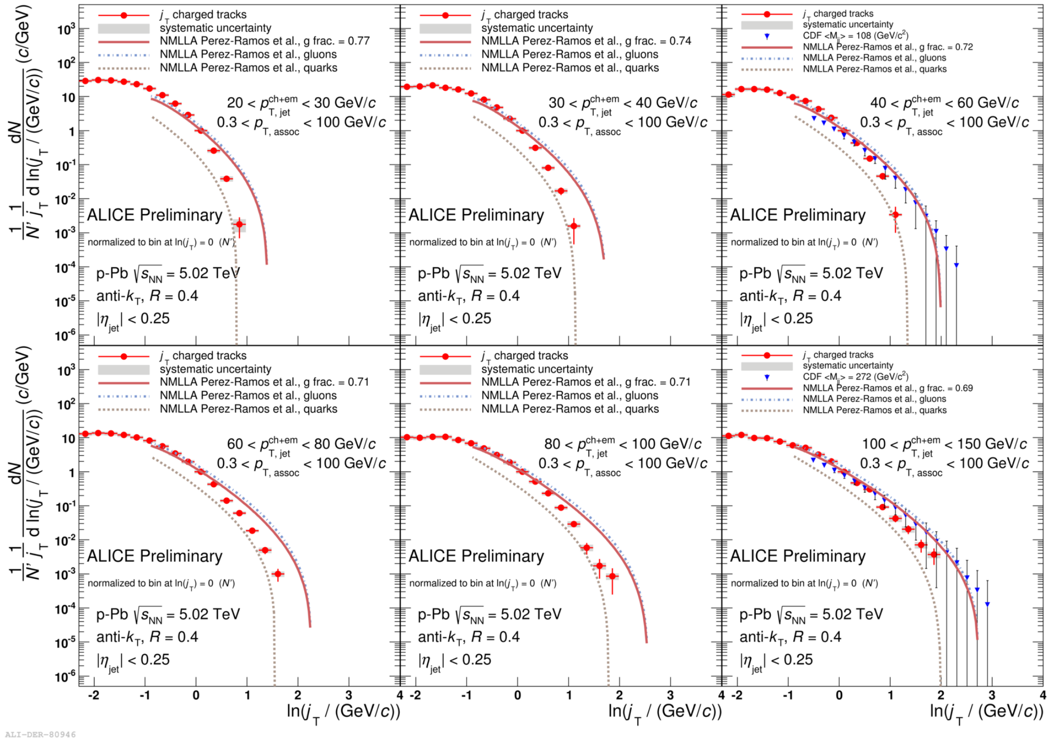

Figure 6.32: Final j_{T} spectrum compared to NMLLA model [101, 102] and CDF data points [100], for bins, where those are available.. Three curves for model comparison are shown, quark jets (lower) gluon jets (higher) and combination (middle).

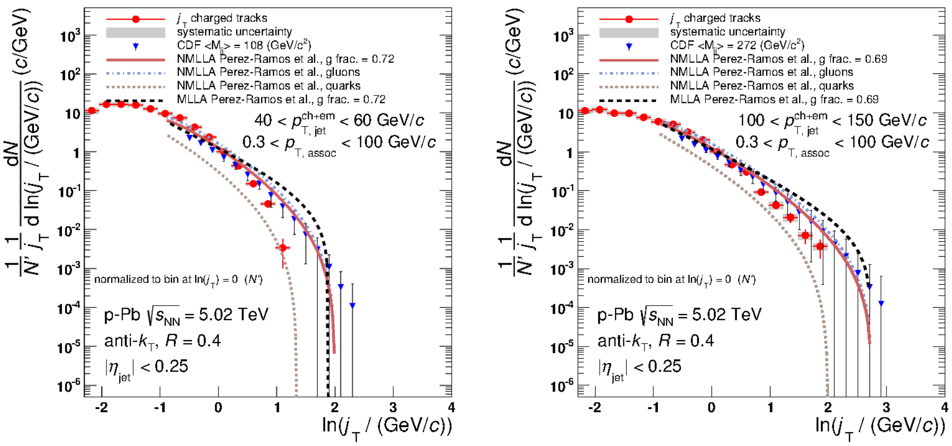

Figure 6.33: Final j_T spectrum compared to NMLLA and MLLA model [101, 102] and CDF data points [100].

6.7.2 Discussion

The NMLLA is found to have different (less steep) slope than the ALICE data. The difference is larger for lower jet p_T bins. Higher order corrections which are not included in the NMLLA improve the description of energy momentum conservation (by better description of parton recoils). Higher order corrections are important especially in the lower jet p_T bins. The parton showers more extensively in the higher j_T region, as it is left with more energy. The more extensive showering results then in overestimate of the hard hadron production.

With help of PYTHIA it was shown in section 6.6 that using an identically large acceptance cone around a jet axis from which the j_T distribution is constructed, the j_T spectrum shape changes significantly with the R of jet finder that is used to reconstruct the jet. A possible explanations for this effect are jet splitting or the fact that with lower R cone, it is easier to tilt the jet axis toward a more energetic constituent and hence decrease the overall large transverse momenta. Comparison of j_T distributions obtained using different jet finder algorithm configurations is not straightforward. This shows very well when doing the comparison in between CDF and ALICE results.

The ultimate goal of the analysis is to study and compare the jet fragmentation in p–p, p–Pb and PbPb data. The p–Pb data set was chosen to start with thanks to it's good quality and well working trigger. During the initial stage of the work the author tried to reproduce CDF results with PYTHIA, the j_T spectrum dependence on R was observed. This observation gives the prospect of comparing CDF and ALICE p–p data with use of MC based correction of the R dependence.

Chapter 7

Summary

This thesis presents results of the Ph.D. work of the author in physics data analysis and experimental hardware areas. Measurement of j_T spectrum of charged jet constituents of full jets with jet $p_{\mathrm{T}} = 20\text{-}150$ GeV/c at p–Pb collisions at $\sqrt{s} = 5.02$ TeV at ALICE experiment is presented. The results of the measurements were shown in form of a poster at the Quark Matter 2014 conference. On the hardware front, the thesis describes development of the Level–0 trigger for the ALICE EMCal detector. The core part of the trigger development was published in [142]. Aside of the two major topics, a partial description of analysis of neutral pion invariant yield in PbPb collisions at ALICE, tho which the author also contributed significantly, is included.

The main contribution of the author of the thesis lies in conducting the j_T analysis at the LHC energies. It was shown that the NMLLA is still closer match to data than the MLLA computation. Additionally it was shown that in order to compare the experimental j_T results to theory, the theory should take into account the form of experimentally reconstructed jets. Even if the j_T spectra would be constructed from particles inside a fixed size cone around the jet axis, the final spectra shape is still sensitive to the configuration of the jet finding algorithm that recovered the axis of the jet.

The j_T analysis in p–Pb data provides bases for the future extension of the analysis to the p–p and PbPb data, so the effects of the (cold) nuclear matter can be studied. Possibly an insight can be gained into medium induced soft gluon radiation. The studied jets can be biased by requirement of a constituent of a certain initial momentum fraction z, in this way a larger insight into fragmentation of the jets can be gained.

On the hardware front, the main contribution of the author is completion of the project of the Level–0 EMCal trigger for ALICE. Multiple out of the box solutions on trigger firmware level were developed in order to save the money invested into a hardware, which suffered from multiple design failures, and to bring the trigger in operation for the Run 1 of the LHC. New approach to capture timing of data incoming from ADC chips was developed to overcome issues with routing of returning clock lines, light weight deserialization was designed to speed up the process of data stream recovery and the Level–0 decision algorithm was heavily optimized to achieve its FPGA algorithm processing time of 1.5 LHC clocks. The author gradually took over responsibility for all aspects of the Level–0 trigger system in EMCal (hardware, firmware, control system, commissioning, run support, performance evaluation, endorsement by the collaboration). The trigger entered operation early in 2011 as the first calorimeter trigger in ALICE. The existence of the EMCal triggered data set enabled multiple analysis. Both analysis presented in this thesis do rely on data gathered by the EMCal trigger system, the reach of the j_T analysis is fully dependent on the triggered data set.

Significant contribution of the author can be also found in improving the understanding of the ALICE EMCal detector behavior and calibrations and continuous support of its operation.

Appendix A

Glossary of used symbols

AGS - Alternating Gradient Synchrotron
ALTRO - ALICE TPC Readout Chip
AOD - Slimmed data format in ALICE
APD - Avalanche Photo Diod
BNL - Brookhaven National Laboratory
CERN - European Organization for Nuclear Research
CTP - Central Trigger Processor
DAQ - Data Acquisition
DCal - Di-Jet Calorimeter
DCS - Detector Control System
DDL - Detector Data Link
DIS - Deep Inelastic Scattering
DQM - Data Quality Monitoring
EMCal - Electromagnetic Calorimeter
ESD - Data format in ALICE
FEE - Front-End Electronics
FF - Fragmentation Function
FMD - Forward Multiplicity Detector
FPGA - Field Programmable Gateway Array
FSR - Final State Radiation
GTL - Gunning Transceiver Logic
HMPID - High Momentum Particle Identification
HS - Hard Scattering
HV - High voltage
ITS - Inner Tracking System
ISR - Initial State Radiation
L0 - Level-0 trigger decision
L1 - Level 1 trigger decision

LCU	-	Led Control Unit
LHC	-	Large Hadron Collider
lQCD	-	Lattice QCD
LSB	-	Least Significant Bit
LV	-	Low voltage
MB	-	Minimum Bias
MEB	-	Multi-Event Buffer
MIP	-	Minimum Ionizing Particle
MSB	-	Most Significant Bit
NNLO	-	Next-to-Next-to-Leading Order
PCB	-	Printed Circuit Board
PDF	-	Parton Distribution Function
PDG	-	Particle Data Group
PHOS	-	Photon Spectrometer
PID	-	Particle Identification
pQCD	-	Perturbative QCD
PVSS	-	High level control system used in ALICE DCS (WinCC now)
QCD	-	Quantum ChromoDynamics
QED	-	Quantum ElectroDynamics
QGP	-	Quark Gluon Plasma
RCU	-	Readout Control Unit
RHIC	-	Relativistic Heavy Ion Collider
SDD	-	Silicon Drift Detector
SLAC	-	Stanford Linear Accelerator Center
SM	-	Super Module
SMAQ	-	CTP Trigger Decision Snapshot Monitor
SPD	-	Silicon Pixel Detector
SPS	-	Super Proton Synchrotron
SRU	-	Scalable Readout Unit
SSD	-	Silicon Strip Detector
T0	-	T Zero detector
TOF	-	Time of Flight
TPC	-	Time Projection Champer
TRD	-	Transition Radiation Detector
TRU	-	Trigger Region Unit
TTCrx	-	Trigger Timing and Clock receiver chip
URHIC	-	Ultra-Relativistic Heavy Ion Collision
V0	-	V Zero detector
ZDC	-	Zero Degree Calorimeter

Bibliography

[1] L. Evans and P. Bryant, “LHC Machine,” *JINST*, vol. 3, p. S08001, 2008.

[2] G. Aad *et al.*, “Observation of a new particle in the search for the Standard Model Higgs boson with the ATLAS detector at the LHC,” *Phys.Lett.*, vol. B716, pp. 1–29, 2012.

[3] S. Chatrchyan *et al.*, “Observation of a new boson at a mass of 125 GeV with the CMS experiment at the LHC,” *Phys.Lett.*, vol. B716, pp. 30–61, 2012.

[4] E. V. Shuryak, “Quantum Chromodynamics and the Theory of Superdense Matter,” *Phys.Rept.*, vol. 61, pp. 71–158, 1980.

[5] K. Aamodt *et al.*, “The ALICE experiment at the CERN LHC,” *JINST*, vol. 3, p. S08002, 2008.

[6] M. Gell-Mann, “Symmetries of baryons and mesons,” *Phys.Rev.*, vol. 125, pp. 1067–1084, 1962.

[7] Y. Neeman, “GAUGES, GROUPS AND AN INVARIANT THEORY OF THE STRONG INTERACTIONS,” 1961.

[8] G. ’t Hooft, “Renormalizable Lagrangians for Massive Yang-Mills Fields,” *Nucl.Phys.*, vol. B35, pp. 167–188, 1971.

[9] M. Gell-Mann, “A Schematic Model of Baryons and Mesons,” *Phys.Lett.*, vol. 8, pp. 214–215, 1964.

[10] G. Zweig, “An SU(3) model for strong interaction symmetry and its breaking. Version 2,” pp. 22–101, 1964.

[11] M. Han and Y. Nambu, “Three Triplet Model with Double SU(3) Symmetry,” *Phys.Rev.*, vol. 139, pp. B1006–B1010, 1965.

[12] V. Barnes, P. Connolly, D. Crennell, B. Culwick, W. Delaney, *et al.*, “Observation of a Hyperon with Strangeness -3,” *Phys.Rev.Lett.*, vol. 12, pp. 204–206, 1964.

[13] M. Breidenbach, J. I. Friedman, H. W. Kendall, E. D. Bloom, D. Coward, *et al.*, "Observed Behavior of Highly Inelastic electron-Proton Scattering," *Phys.Rev.Lett.*, vol. 23, pp. 935–939, 1969.

[14] R. Feynman, "The behavior of hadron collisions at extreme energies," *Conf.Proc.*, vol. C690905, pp. 237–258, 1969.

[15] J. Bjorken and E. A. Paschos, "Inelastic Electron Proton and gamma Proton Scattering, and the Structure of the Nucleon," *Phys.Rev.*, vol. 185, pp. 1975–1982, 1969.

[16] W. Panofsky, "ELECTROMAGNETIC INTERACTIONS: LOW q**2 ELECTRODYNAMICS: ELASTIC AND INELASTIC ELECTRON (AND MUON) SCATTERING," 1968.

[17] J. Bjorken, "Asymptotic Sum Rules at Infinite Momentum," *Phys.Rev.*, vol. 179, pp. 1547–1553, 1969.

[18] J. R. Ellis, M. K. Gaillard, and G. G. Ross, "Search for Gluons in e+ e- Annihilation," *Nucl.Phys.*, vol. B111, p. 253, 1976.

[19] F. Abe *et al.*, "Observation of top quark production in $\bar{p}p$ collisions," *Phys.Rev.Lett.*, vol. 74, pp. 2626–2631, 1995.

[20] S. Abachi *et al.*, "Search for high mass top quark production in $p\bar{p}$ collisions at $\sqrt{s} = 1.8$ TeV," *Phys.Rev.Lett.*, vol. 74, pp. 2422–2426, 1995.

[21] D. Abbaneo *et al.*, "A Combination of preliminary electroweak measurements and constraints on the standard model," 1999.

[22] D. Williams *et al.*, "Production of the pseudoscalars pi0, eta, and eta-prime in the reaction gamma gamma –> gamma gamma," 1988.

[23] N. Nielsen, "ASYMPTOTIC FREEDOM AS A SPIN EFFECT," *Am.J.Phys.*, vol. 49, p. 1171, 1981.

[24] D. Gross and F. Wilczek, "Asymptotically Free Gauge Theories. 1," *Phys.Rev.*, vol. D8, pp. 3633–3652, 1973.

[25] H. D. Politzer, "Reliable Perturbative Results for Strong Interactions?," *Phys.Rev.Lett.*, vol. 30, pp. 1346–1349, 1973.

[26] D. Duke and R. Roberts, "Analysis of Nucleon Structure Function Moments From Electron and Muon Data and Critical Tests of Asymptotic Freedom," *Phys.Lett.*, vol. B85, p. 289, 1979.

[27] S. Bethke, “Determination of the QCD coupling α_s,” *J.Phys.*, vol. G26, p. R27, 2000.

[28] J. Beringer *et al.*, “Review of Particle Physics (RPP),” *Phys.Rev.*, vol. D86, p. 010001, 2012.

[29] J. C. Collins and M. Perry, “Superdense Matter: Neutrons Or Asymptotically Free Quarks?,” *Phys.Rev.Lett.*, vol. 34, p. 1353, 1975.

[30] K. Kajantie, M. Laine, K. Rummukainen, and Y. Schroder, “The Pressure of hot QCD up to g6 ln(1/g),” *Phys.Rev.*, vol. D67, p. 105008, 2003.

[31] K. G. Wilson, “The Renormalization Group: Critical Phenomena and the Kondo Problem,” *Rev.Mod.Phys.*, vol. 47, p. 773, 1975.

[32] F. Karsch, E. Laermann, A. Peikert, C. Schmidt, and S. Stickan, “QCD thermodynamics with 2 and 3 quark flavors,” pp. 180–185, 2000.

[33] Z. Fodor and S. Katz, “Critical point of QCD at finite T and mu, lattice results for physical quark masses,” *JHEP*, vol. 0404, p. 050, 2004.

[34] F. Karsch, “Lattice QCD at high temperature and density,” *Lect.Notes Phys.*, vol. 583, pp. 209–249, 2002.

[35] F. Karsch, E. Laermann, and A. Peikert, “The Pressure in two flavor, (2+1)-flavor and three flavor QCD,” *Phys.Lett.*, vol. B478, pp. 447–455, 2000.

[36] D. Teaney, “The Effects of viscosity on spectra, elliptic flow, and HBT radii,” *Phys.Rev.*, vol. C68, p. 034913, 2003.

[37] E. Iancu, “Theory summary for ISMD2000,” pp. 411–437, 2011.

[38] M. L. Miller, K. Reygers, S. J. Sanders, and P. Steinberg, “Glauber modeling in high energy nuclear collisions,” *Ann.Rev.Nucl.Part.Sci.*, vol. 57, pp. 205–243, 2007.

[39] U. W. Heinz and M. Jacob, “Evidence for a new state of matter: An Assessment of the results from the CERN lead beam program,” 2000.

[40] G. Agakishiev *et al.*, “Low mass e+ e- pair production in 158/A-GeV Pb - Au collisions at the CERN SPS, its dependence on multiplicity and transverse momentum,” *Phys.Lett.*, vol. B422, pp. 405–412, 1998.

[41] M. Abreu *et al.*, “Evidence for deconfinement of quarks and gluons from the J / psi suppression pattern measured in Pb + Pb collisions at the CERN SPS,” *Phys.Lett.*, vol. B477, pp. 28–36, 2000.

[42] T. Matsui and H. Satz, "J/ψ Suppression by Quark-Gluon Plasma Formation," *Phys.Lett.*, vol. B178, p. 416, 1986.

[43] E. Andersen *et al.*, "Strangeness enhancement at mid-rapidity in Pb Pb collisions at 158-A-GeV/c," *Phys.Lett.*, vol. B449, pp. 401–406, 1999.

[44] J. Rafelski and B. Muller, "Strangeness Production in the Quark - Gluon Plasma," *Phys.Rev.Lett.*, vol. 48, p. 1066, 1982.

[45] R. Rapp, "Dilepton Spectroscopy of QCD Matter at Collider Energies," *Adv.High Energy Phys.*, vol. 2013, p. 148253, 2013.

[46] R. Albrecht *et al.*, "Transverse momentum distributions of neutral pions from nuclear collisions at 200-A/GeV," *Eur.Phys.J.*, vol. C5, pp. 255–267, 1998.

[47] M. Aggarwal *et al.*, "Centrality dependence of neutral pion production in 158-A-GeV Pb-208 + Pb-208 collisions," *Phys.Rev.Lett.*, vol. 81, pp. 4087–4091, 1998.

[48] X.-N. Wang, "Where is the jet quenching in Pb + Pb collisions at 158-A-GeV?," *Phys.Rev.Lett.*, vol. 81, pp. 2655–2658, 1998.

[49] B. Lenkeit *et al.*, "Recent results from Pb - Au collisions at 158-GeV/c per nucleon obtained with the CERES spectrometer," *Nucl.Phys.*, vol. A661, pp. 23–32, 1999.

[50] S. Adler *et al.*, "Suppressed pi0 production at large transverse momentum in central Au+ Au collisions at S(NN)**1/2 = 200 GeV," *Phys.Rev.Lett.*, vol. 91, p. 072301, 2003.

[51] J. Adams *et al.*, "Transverse momentum and collision energy dependence of high p(T) hadron suppression in Au+Au collisions at ultrarelativistic energies," *Phys.Rev.Lett.*, vol. 91, p. 172302, 2003.

[52] K. Adcox *et al.*, "Suppression of hadrons with large transverse momentum in central Au+Au collisions at $\sqrt{s_N N}$ = 130-GeV," *Phys.Rev.Lett.*, vol. 88, p. 022301, 2002.

[53] J. L. Albacete, A. Dumitru, and C. Marquet, "The initial state of heavy-ion collisions," *Int.J.Mod.Phys.*, vol. A28, p. 1340010, 2013.

[54] D. d'Enterria, "Jet quenching," 2009.

[55] U. A. Wiedemann, "Jet Quenching in Heavy Ion Collisions," pp. 521–562, 2010.

[56] N. Armesto, B. Cole, C. Gale, W. A. Horowitz, P. Jacobs, *et al.*, "Comparison of Jet Quenching Formalisms for a Quark-Gluon Plasma 'Brick'," *Phys.Rev.*, vol. C86, p. 064904, 2012.

[57] B. Kopeliovich, J. Nemchik, I. Potashnikova, and I. Schmidt, “Quenching of high-pT hadrons: Energy Loss vs Color Transparency,” *Phys.Rev.*, vol. C86, p. 054904, 2012.

[58] J. Nemchik, I. A. Karpenko, B. Kopeliovich, I. Potashnikova, and Y. M. Sinyukov, “High-pT hadrons from nuclear collisions: Unifying pQCD with hydrodynamics,” 2013.

[59] W. A. Horowitz, “LHC Predictions from an extended theory with Elastic, Inelastic, and Path Length Fluctuating Energy Loss,” *Int.J.Mod.Phys.*, vol. E16, pp. 2193–2199, 2007.

[60] K. Ackermann *et al.*, “Elliptic flow in Au + Au collisions at (S(NN))**(1/2) = 130 GeV,” *Phys.Rev.Lett.*, vol. 86, pp. 402–407, 2001.

[61] S. Voloshin and Y. Zhang, “Flow study in relativistic nuclear collisions by Fourier expansion of Azimuthal particle distributions,” *Z.Phys.*, vol. C70, pp. 665–672, 1996.

[62] P. Stankus, “Direct photon production in relativistic heavy-ion collisions,” *Ann.Rev.Nucl.Part.Sci.*, vol. 55, pp. 517–554, 2005.

[63] A. Adare *et al.*, “Enhanced production of direct photons in Au+Au collisions at $\sqrt{s_N N} = 200$ GeV and implications for the initial temperature,” *Phys.Rev.Lett.*, vol. 104, p. 132301, 2010.

[64] J. Rak and M. J. Tannenbaum, *"High-p_T physics in the Heavy Ion Era"*. Cambridge University Press, 2013.

[65] R. Feynman, “THE BEHAVIOR OF HADRON COLLISIONS AT EXTREME ENERGIES,” 1989.

[66] R. Cutler and D. W. Sivers, “QUANTUM CHROMODYNAMIC GLUON CONTRIBUTIONS TO LARGE P(T) REACTIONS,” *Phys. Rev.*, vol. D17, p. 196, 1978.

[67] J. F. Owens, “LARGE MOMENTUM TRANSFER PRODUCTION OF DIRECT PHOTONS, JETS, AND PARTICLES,” *Rev. Mod. Phys.*, vol. 59, p. 465, 1987.

[68] S. D. Drell and T.-M. Yan, “Massive Lepton Pair Production in Hadron-Hadron Collisions at High-Energies,” *Phys. Rev. Lett.*, vol. 25, pp. 316–320, 1970.

[69] J. C. Collins, D. E. Soper, and G. F. Sterman, “Factorization of Hard Processes in QCD,” *Adv.Ser.Direct.High Energy Phys.*, vol. 5, pp. 1–91, 1988.

[70] V. Gribov and L. Lipatov, “Deep inelastic e p scattering in perturbation theory,” *Sov.J.Nucl.Phys.*, vol. 15, pp. 438–450, 1972.

[71] G. Altarelli and G. Parisi, “Asymptotic Freedom in Parton Language,” *Nucl.Phys.*, vol. B126, p. 298, 1977.

[72] Y. L. Dokshitzer, “Calculation of the Structure Functions for Deep Inelastic Scattering and e+ e- Annihilation by Perturbation Theory in Quantum Chromodynamics.,” *Sov.Phys.JETP*, vol. 46, pp. 641–653, 1977.

[73] J. Pumplin, D. Stump, J. Huston, H. Lai, P. M. Nadolsky, *et al.*, “New generation of parton distributions with uncertainties from global QCD analysis,” *JHEP*, vol. 0207, p. 012, 2002.

[74] A. Cooper-Sarkar, “PDF Fits at HERA,” *PoS*, vol. EPS-HEP2011, p. 320, 2011.

[75] M. Botje, J. Butterworth, A. Cooper-Sarkar, A. de Roeck, J. Feltesse, *et al.*, “The PDF4LHC Working Group Interim Recommendations,” 2011.

[76] F. Aaron *et al.*, “Combined Measurement and QCD Analysis of the Inclusive e+- p Scattering Cross Sections at HERA,” *JHEP*, vol. 1001, p. 109, 2010.

[77] B. Andersson, G. Gustafson, G. Ingelman, and T. Sjostrand, “Parton Fragmentation and String Dynamics,” *Phys.Rept.*, vol. 97, pp. 31–145, 1983.

[78] M. Jacob and P. Landshoff, “Large Transverse Momentum and Jet Studies,” *Phys.Rept.*, vol. 48, p. 285, 1978.

[79] P. Abreu *et al.*, “Measurement of the gluon fragmentation function and a comparison of the scaling violation in gluon and quark jets,” *Eur.Phys.J.*, vol. C13, pp. 573–589, 2000.

[80] G. Hanson, G. Abrams, A. Boyarski, M. Breidenbach, F. Bulos, *et al.*, “Evidence for Jet Structure in Hadron Production by e+ e- Annihilation,” *Phys.Rev.Lett.*, vol. 35, pp. 1609–1612, 1975.

[81] G. Hanson, M. Alam, A. Boyarski, M. Breidenbach, F. Bulos, *et al.*, “Hadron Production by e^+e^- Annihilation at Center-of-mass Energies Between 2.6-GeV and 7.8-GeV. Part 2. Jet Structure and Related Inclusive Distributions,” *Phys.Rev.*, vol. D26, p. 991, 1982.

[82] R. Brandelik *et al.*, “Evidence for Planar Events in e+ e- Annihilation at High-Energies,” *Phys.Lett.*, vol. B86, p. 243, 1979.

[83] C. Berger *et al.*, “Evidence for Gluon Bremsstrahlung in e+ e- Annihilations at High-Energies,” *Phys.Lett.*, vol. B86, p. 418, 1979.

[84] W. Bartel *et al.*, "Observation of Planar Three Jet Events in e+ e- Annihilation and Evidence for Gluon Bremsstrahlung," *Phys.Lett.*, vol. B91, p. 142, 1980.

[85] D. Barber, U. Becker, H. Benda, A. Boehm, J. Branson, *et al.*, "Discovery of Three Jet Events and a Test of Quantum Chromodynamics at PETRA Energies," *Phys.Rev.Lett.*, vol. 43, p. 830, 1979.

[86] G. F. Sterman and S. Weinberg, "Jets from Quantum Chromodynamics," *Phys.Rev.Lett.*, vol. 39, p. 1436, 1977.

[87] A. Abulencia *et al.*, "Measurement of the Inclusive Jet Cross Section using the $\boldsymbol{k}_{\mathbf{T}}$ algorithmin$\boldsymbol{p\overline{p}}$ Collisions at$\sqrt{\boldsymbol{s}} = 1.96$ TeV with the CDF II Detector," *Phys.Rev.*, vol. D75, p. 092006, 2007.

[88] G. Aad *et al.*, "Measurement of the inclusive jet cross section in pp collisions at sqrt(s)=2.76 TeV and comparison to the inclusive jet cross section at sqrt(s)=7 TeV using the ATLAS detector," *Eur.Phys.J.*, vol. C73, p. 2509, 2013.

[89] G. P. Salam and G. Soyez, "A Practical Seedless Infrared-Safe Cone jet algorithm," *JHEP*, vol. 0705, p. 086, 2007.

[90] M. Cacciari, G. P. Salam, and G. Soyez, "The Anti-k(t) jet clustering algorithm," *JHEP*, vol. 0804, p. 063, 2008.

[91] S. Catani, Y. L. Dokshitzer, M. Olsson, G. Turnock, and B. Webber, "New clustering algorithm for multi - jet cross-sections in e+ e- annihilation," *Phys.Lett.*, vol. B269, pp. 432–438, 1991.

[92] Y. L. Dokshitzer, V. A. Khoze, A. H. Mueller, and S. Troian, "Basics of perturbative QCD," 1991.

[93] Y. L. Dokshitzer, V. S. Fadin, and V. A. Khoze, "Coherent Effects in the Perturbative QCD Parton Jets," *Phys.Lett.*, vol. B115, pp. 242–246, 1982.

[94] A. Bassetto, M. Ciafaloni, G. Marchesini, and A. H. Mueller, "Jet Multiplicity and Soft Gluon Factorization," *Nucl.Phys.*, vol. B207, p. 189, 1982.

[95] A. H. Mueller, "On the Multiplicity of Hadrons in QCD Jets," *Phys.Lett.*, vol. B104, pp. 161–164, 1981.

[96] G. Marchesini and B. Webber, "Simulation of QCD Jets Including Soft Gluon Interference," *Nucl.Phys.*, vol. B238, p. 1, 1984.

[97] B. Ermolaev and V. S. Fadin, "Log - Log Asymptotic Form of Exclusive Cross-Sections in Quantum Chromodynamics," *JETP Lett.*, vol. 33, pp. 269–272, 1981.

[98] Y. L. Dokshitzer, V. S. Fadin, and V. A. Khoze, “Double Logs of Perturbative QCD for Parton Jets and Soft Hadron Spectra,” *Z.Phys.*, vol. C15, p. 325, 1982.

[99] Y. I. Azimov, Y. L. Dokshitzer, V. A. Khoze, and S. Troyan, “Similarity of Parton and Hadron Spectra in QCD Jets,” *Z.Phys.*, vol. C27, pp. 65–72, 1985.

[100] T. Aaltonen *et al.*, “Measurement of the k_T Distribution of Particles in Jets Produced in $p\bar{p}$ Collisions at $\sqrt{s} = 1.96$-TeV,” *Phys.Rev.Lett.*, vol. 102, p. 232002, 2009.

[101] F. Arleo, R. P. Ramos, and B. Machet, “Hadronic single inclusive k-perpendicular distributions inside one jet beyond MLLA,” *Phys.Rev.Lett.*, vol. 100, p. 052002, 2008.

[102] R. Perez-Ramos, F. Arleo, and B. Machet, “Next-to-MLLA corrections to single inclusive k^- perp-distributions and 2-particle correlations in a jet,” *Phys.Rev.*, vol. D78, p. 014019, 2008.

[103] Y. I. Azimov, Y. L. Dokshitzer, V. A. Khoze, and S. Troyan, “Humpbacked QCD Plateau in Hadron Spectra,” *Z.Phys.*, vol. C31, p. 213, 1986.

[104] W. Braunschweig *et al.*, “Global Jet Properties at 14-GeV to 44-GeV Center-of-mass Energy in e^+e^- Annihilation,” *Z.Phys.*, vol. C47, pp. 187–198, 1990.

[105] M. Gyulassy and X.-n. Wang, “Multiple collisions and induced gluon Bremsstrahlung in QCD,” *Nucl.Phys.*, vol. B420, pp. 583–614, 1994.

[106] R. Baier, Y. L. Dokshitzer, A. H. Mueller, S. Peigne, and D. Schiff, “Radiative energy loss and p(T) broadening of high-energy partons in nuclei,” *Nucl.Phys.*, vol. B484, pp. 265–282, 1997.

[107] A. H. Mueller and J.-w. Qiu, “Gluon Recombination and Shadowing at Small Values of x,” *Nucl.Phys.*, vol. B268, p. 427, 1986.

[108] J. Cronin, H. J. Frisch, M. Shochet, J. Boymond, R. Mermod, *et al.*, “Production of Hadrons with Large Transverse Momentum at 200-GeV, 300-GeV, and 400-GeV,” *Phys.Rev.*, vol. D11, p. 3105, 1975.

[109] S. Adler *et al.*, “Common suppression pattern of eta and pi0 mesons at high transverse momentum in Au+Au collisions at S(NN)**(1/2) = 200-GeV,” *Phys.Rev.Lett.*, vol. 96, p. 202301, 2006.

[110] B. B. Abelev *et al.*, “Transverse momentum dependence of inclusive primary charged-particle production in p-Pb collisions at $\sqrt{s_N N} = 5.02$ TeV,” 2014.

[111] T. Renk and K. J. Eskola, “Hard dihadron correlations in heavy-ion collisions at RHIC and LHC,” *Phys.Rev.*, vol. C84, p. 054913, 2011.

[112] J. Adams *et al.*, “Evidence from d + Au measurements for final state suppression of high p(T) hadrons in Au+Au collisions at RHIC,” *Phys.Rev.Lett.*, vol. 91, p. 072304, 2003.

[113] K. Aamodt *et al.*, “Particle-yield modification in jet-like azimuthal di-hadron correlations in Pb-Pb collisions at $\sqrt{s_N N} = 2.76$ TeV,” *Phys.Rev.Lett.*, vol. 108, p. 092301, 2012.

[114] N. Armesto, “Nuclear shadowing,” *J.Phys.*, vol. G32, pp. R367–R394, 2006.

[115] E. Courant, M. Livingston, and H. Snyder, “The strong-focusing synchrotron: A new high-energy accelerator,” *Phys.Rev.*, vol. 88, pp. 1190–1196, 1952.

[116] S. van der Meer, “Calibration of the Effective Beam Height in the ISR,” 1968.

[117] G. Aad *et al.*, “The ATLAS Experiment at the CERN Large Hadron Collider,” *JINST*, vol. 3, p. S08003, 2008.

[118] S. Chatrchyan *et al.*, “The CMS experiment at the CERN LHC,” *JINST*, vol. 3, p. S08004, 2008.

[119] J. Alves, A. Augusto *et al.*, “The LHCb Detector at the LHC,” *JINST*, vol. 3, p. S08005, 2008.

[120] K. Aamodt *et al.*, “The ALICE experiment at the CERN LHC,” *JINST*, vol. 3, p. S08002, 2008.

[121] “ALICE technical design report of the dimuon forward spectrometer,” 1999.

[122] J. Alme, Y. Andres, H. Appelshauser, S. Bablok, N. Bialas, *et al.*, “The ALICE TPC, a large 3-dimensional tracking device with fast readout for ultra-high multiplicity events,” *Nucl.Instrum.Meth.*, vol. A622, pp. 316–367, 2010.

[123] G. Dellacasa *et al.*, “ALICE: Technical design report of the time projection chamber,” 2000.

[124] G. Dellacasa *et al.*, “ALICE technical design report of the inner tracking system (ITS),” 1999.

[125] G. Dellacasa *et al.*, “ALICE: Technical design report of the transition radiation detector.,” 2000.

[126] G. Dellacasa *et al.*, “ALICE technical design report of the time-of-flight system (TOF),” 2000.

[127] F. Piuz, W. Klempt, L. Leistam, J. De Groot, and J. SchÃijkraft, “ALICE high-momentum particle identification: Technical Design Report,” 1998.

[128] P. Cortese *et al.*, “ALICE technical design report on forward detectors: FMD, T0 and V0,” 2004.

[129] P. Cortese, G. Dellacasa, *et al.*, “ALICE Electromagnetic Calorimeter Technical Design Report,” Aug 2008.

[130] T. C. Awes, “The ALICE electromagnetic calorimeter,” *Nucl.Instrum.Meth.*, vol. A617, pp. 5–8, 2010.

[131] G. Dellacasa *et al.*, “ALICE technical design report of the photon spectrometer (PHOS),” 1999.

[132] J. Allen *et al.*, “ALICE DCal: An Addendum to the EMCal Technical Design Report Di-Jet and Hadron-Jet correlation measurements in ALICE,” Jun 2010.

[133] F. Carminati *et al.*, “ALICE: Physics performance report, volume I,” *J.Phys.*, vol. G30, pp. 1517–1763, 2004.

[134] B. Alessandro *et al.*, “ALICE: Physics performance report, volume II,” *J.Phys.*, vol. G32, pp. 1295–2040, 2006.

[135] B. B. Abelev *et al.*, “Performance of the ALICE Experiment at the CERN LHC,” 2014.

[136] F. Carena *et al.*, “Preparing the ALICE DAQ upgrade,” *J.Phys.Conf.Ser.*, vol. 396, p. 012050, 2012.

[137] R. Esteve Bosch, A. Jimenez de Parga, B. Mota, and L. Musa, “The ALTRO chip: A 16-channel A/D converter and digital processor for gas detectors,” *IEEE Trans.Nucl.Sci.*, vol. 50, pp. 2460–2469, 2003.

[138] “ALTRO manual,”

[139] A. ur Rehman, “Performance of the ALICE TPC Readout Electronics,” *IEEE Nucl.Sci.Symp.Conf.Rec.*, vol. 2011, pp. 1014–1018, 2011.

[140] D. Swoboda, P. Van de Vyvre, and O. Villalobos Baillie, “Data Acquisition, Control and Trigger : common Report for the preparation of the ALICE Technical Design Reports.,” 1998.

[141] F. Zhang, H. Muller, T. C. Awes, S. Martoiu, J. Kral, *et al.*, "Point-to-point readout for the ALICE EMCal detector," *Nucl.Instrum.Meth.*, vol. A735, pp. 157–162, 2014.

[142] J. Kral, T. Awes, H. Muller, J. Rak, and J. Schambach, "L0 trigger for the EMCal detector of the ALICE experiment," *Nucl.Instrum.Meth.*, vol. A693, pp. 261–267, 2012.

[143] O. Bourrion *et al.*, "The ALICE EMCal L1 trigger first year of operation experience," *JINST*, vol. 8, p. C01013, 2013.

[144] K. Deiters, Q. Ingram, and D. Renker, "Response of avalanche photo-diodes of the CMS Electromagnetic Calorimeter to neutrons from an Americium-Beryllium source.," 2010.

[145] H. Grassmann and H. G. Moser, "Shower shape analysis and longitudinal sampled electromagnetic calorimeters," Tech. Rep. PITHA-84-33, Aachen TU 3. Inst. Phys., Aachen, Nov 1984.

[146] P. Moreira and A. Marchioro, "QPLL a Quartz Crystal Based PLL for Jitter Filtering Applications in LHC,"

[147] J. Kral, "TRU configuration guide," *unpublished*.

[148] B. von Haller *et al.*, "The ALICE data quality monitoring system," *J.Phys.Conf.Ser.*, vol. 331, p. 022030, 2011.

[149] A. Morreale and J. Kral, "A Pi0 invariant yields from Pb+Pb collisions (LHC11h) measured with the EMCal," *unpublished*.

[150] B. B. Abelev *et al.*, "Neutral pion production at midrapidity in pp and Pb-Pb collisions at $\sqrt{s_N N} = 2.76$ TeV," 2014.

[151] B. Abelev *et al.*, "Neutral pion and η meson production in proton-proton collisions at $\sqrt{s} = 0.9$ TeV and $\sqrt{s} = 7$ TeV," *Phys.Lett.*, vol. B717, pp. 162–172, 2012.

[152] A. Adare *et al.*, "Inclusive cross-section and double helicity asymmetry for pi0 production in p + p collisions at s**(1/2) = 200-GeV: Implications for the polarized gluon distribution in the proton," *Phys.Rev.*, vol. D76, p. 051106, 2007.

[153] D. d'Enterria, K. J. Eskola, I. Helenius, and H. Paukkunen, "Confronting current NLO parton fragmentation functions with inclusive charged-particle spectra at hadron colliders," *Nucl.Phys.*, vol. B883, pp. 615–628, 2014.

[154] C. Adler *et al.*, “Centrality dependence of high p_T hadron suppression in Au+Au collisions at $\sqrt{s}_N N = 130$-GeV,” *Phys.Rev.Lett.*, vol. 89, p. 202301, 2002.

[155] J. M. Maldacena, “The Large N limit of superconformal field theories and supergravity,” *Adv.Theor.Math.Phys.*, vol. 2, pp. 231–252, 1998.

[156] J. L. Petersen, “Introduction to the Maldacena conjecture on AdS / CFT,” *Int.J.Mod.Phys.*, vol. A14, pp. 3597–3672, 1999.

[157] O. Aharony, S. S. Gubser, J. M. Maldacena, H. Ooguri, and Y. Oz, “Large N field theories, string theory and gravity,” *Phys.Rept.*, vol. 323, pp. 183–386, 2000.

[158] H. Liu, K. Rajagopal, and U. A. Wiedemann, “Wilson loops in heavy ion collisions and their calculation in AdS/CFT,” *JHEP*, vol. 0703, p. 066, 2007.

[159] C. Herzog, A. Karch, P. Kovtun, C. Kozcaz, and L. Yaffe, “Energy loss of a heavy quark moving through N=4 supersymmetric Yang-Mills plasma,” *JHEP*, vol. 0607, p. 013, 2006.

[160] S. S. Gubser, S. S. Pufu, and A. Yarom, “Sonic booms and diffusion wakes generated by a heavy quark in thermal AdS/CFT,” *Phys.Rev.Lett.*, vol. 100, p. 012301, 2008.

[161] D. E. Kharzeev, “Parton energy loss at strong coupling and the universal bound,” *Eur.Phys.J.*, vol. C61, pp. 675–682, 2009.

[162] R. Sharma, I. Vitev, and B.-W. Zhang, “Light-cone wave function approach to open heavy flavor dynamics in QCD matter,” *Phys.Rev.*, vol. C80, p. 054902, 2009.

[163] R. Neufeld, I. Vitev, and B.-W. Zhang, “A possible determination of the quark radiation length in cold nuclear matter,” *Phys.Lett.*, vol. B704, pp. 590–595, 2011.

[164] A. Adare *et al.*, “Evolution of π^0 suppression in Au+Au collisions from $\sqrt{s_N N} =$ 39 to 200 GeV,” *Phys.Rev.Lett.*, vol. 109, p. 152301, 2012.

[165] A. Adare *et al.*, “Suppression pattern of neutral pions at high transverse momentum in Au + Au collisions at s(NN)**(1/2) = 200-GeV and constraints on medium transport coefficients,” *Phys.Rev.Lett.*, vol. 101, p. 232301, 2008.

[166] M. Aggarwal *et al.*, “Suppression of High-p(T) Neutral Pions in Central Pb+Pb Collisions at s(NN)**(1/2) = 17.3-GeV,” *Phys.Rev.Lett.*, vol. 100, p. 242301, 2008.

[167] B. B. Abelev *et al.*, “Production of charged pions, kaons and protons at large transverse momenta in pp and Pb-Pb collisions at $\sqrt{s_N N} = 2.76$ TeV,” 2014.

[168] B. Abelev *et al.*, “Centrality Dependence of Charged Particle Production at Large Transverse Momentum in Pb–Pb Collisions at $\sqrt{s_{\rm NN}}$ = 2.76 TeV,” *Phys.Lett.*, vol. B720, pp. 52–62, 2013.

[169] A. Angelis *et al.*, “A Measurement of the Transverse Momenta of Partons, and of Jet Fragmentation as a Function of $\sqrt{s}$ in pp Collisions,” *Phys.Lett.*, vol. B97, p. 163, 1980.

[170] S. Adler *et al.*, “Jet properties from dihadron correlations in p^+p collisions at $\sqrt{s}$ = 200-GeV,” *Phys.Rev.*, vol. D74, p. 072002, 2006.

[171] J. Kral, “Study of the transverse momentum distribution of jet constituents in p-Pb collisions at ALICE,” *unpublished.*

[172] M. Cacciari, G. P. Salam, and G. Soyez, “FastJet User Manual,” *Eur.Phys.J.*, vol. C72, p. 1896, 2012.

[173] M. Cacciari, G. P. Salam, and S. Sapeta, “On the characterisation of the underlying event,” *JHEP*, vol. 1004, p. 065, 2010.

[174] S. Chatrchyan *et al.*, “Measurement of the underlying event activity in pp collisions at $\sqrt{s} = 0.9$ and 7 TeV with the novel jet-area/median approach,” *JHEP*, vol. 1208, p. 130, 2012.